Inaugural Dissertation
zur Erlangung des Doktorgrades der Naturwissenschaften
im Fachbereich Mathematik und Informatik, Physik, Geographie der
Justus-Liebig-Universität Gießen

Fractional Resonance Excitation in Dynamic Friction Force Microscopy

vorgelegt von

Felix Mertens

Betreuer

Prof. Dr. André Schirmeisen

Institut für Angewandte Physik

Justus-Liebig-Universität Gießen

April 2015

Abstract

In order to acquire a deeper understanding of interactions between objects on the nanometer scale, the development of new scientific techniques and methods is of central significance. A comprehensive understanding of frictional aspects on this scale helps to pave the way towards innovative material developments.
Friction on the nanometer scale is experimentally accessible since the advent of friction force microscopy (FFM) by *Mate et al.* in 1986. A fine tip at one end of a microscopically small cantilever touches a sample surface and lateral forces lead to deflections of the lever beam which are directly linked with static friction interactions between atoms.
This thesis focuses on a further experimental approach which is referred to as dynamic friction force microscopy (dynamic FFM). A lateral sample modulation combined with dynamic frictional interactions between tip and surface leads to bending or torsional oscillations of the lever, depending on the configuration.
A fractional resonance excitation with a frequency below the natural eigenfrequency of the cantilever beam can lead to a non-linear oscillation state, consisting of stick and slip interactions between tip and surface.
If the excitation amplitude remains small, this causes a linear response where the tip sticks to the surface and directly follows the modulation movement. The cantilever oscillates at the excitation frequency. As soon as the excitation amplitude exceeds a certain threshold, a non-linear tip sliding mechanism sets in, which causes oscillations of the cantilever beam at its resonance frequency.
For friction imaging, a lock-in amplifier scheme detects the arising resonant frequency component, which is directly connected with the transition from static-to-sliding of the tip. A feedback approach monitors the transition amplitude and images local friction of sample surfaces. This approach provides information about frictional properties of surfaces, which can be mapped with very high sensitivity.
Furthermore, this off-resonant excitation technique is extremely sensitive to subtle surface defects. Atomic discoordinations at defects lead to variations in the atomic interaction potential with surface atoms, which is also referred to as Schwoebel-Ehrlich barrier. Increased non-linear frictional tip-sample interactions at defects lead to an increased excitation of resonance oscillations. Surface steps and grain boundaries can clearly be identified and model simulations confirm a contrast mechanism.
Further, the complete resonance behavior of the cantilever is analyzed by using a fast band excitation scheme. Surface elasticity and topographical cross-talk with nanoparticles can furthermore play an important role for the image contrast formation.

Contents

1 Introduction

Tribology is the basic science which addresses the root causes and effects of friction [1]. The movement of a body on a surface is usually connected with losses of kinetic energy. Interactions at the interface between body and surface lead to a force which opposes the movement direction and mechanic energy of the directed macroscopic movement is transferred into undirected microscopic thermal vibrations of molecules and atoms.
Wear and abrasion of surfaces are closely linked with the dissipative mechanism of friction. A seemingly smooth surface on macroscopic scales offers a large number of microscopically small asperities [2]. This surface roughness leads to abrasion at the interface of two bodies. A relative movement causes plastic deformations of micro-contacts and a damaging of the surface structure [3]. In the field of mechanical engineering for example, the quality and durability of surfaces are of central significance. Lubricants reduce friction and abrasive wear at the interface and extends the lifetime of structural components.
An increased wear due to an unfavorable increased surface-to-volume ratio on a microscopic scale is particularly important in the field of small devices and components like microelectromechanical systems (MEMS) [4]. Comparatively higher friction and adhesion results and correspondingly microscopic devices quickly become useless.
A first description of friction on macroscopic scales was given by Leonardo da Vinci (1495) and was later rediscovered by Guillaume Amontons (1699) [1]. These phenomenological principles can be summarized as follows:

1. Friction F_{friction} is proportional to the applied load F_{load}.

2. Friction F_{friction} does not depend on the apparent contact area A_{contact}.

3. Kinetic friction is independent of the sliding velocity v_{slide}.

The first and second principles are also known as Amoton's law. The third law is named after Charles-Augustin de Coulomb and refers to dry friction. In an alternative representation, friction can be expressed by introducing the dimensionless friction coefficient μ [1]

$$F_{\text{friction}} = \mu \cdot F_{\text{load}}. \tag{1.1}$$

Generally, μ is divided into a static friction coefficient μ_{static} and a sliding friction coefficient μ_{sliding} [5]. The static friction force is usually increased compared to the friction force during sliding. Moreover, plastic deformations at the interface result in a growth of micro-contacts (creep) and the static friction coefficient $\mu_{\text{static}}(t)$ increases with the resting time [5].
Different approaches exist for a scientific investigation of frictional interactions at interfaces on different length scales. A common instrument for measuring the sliding friction coefficient between two materials on macroscopic scales is the tribometer [6]. A defined load force presses both materials against each other. An oscillating linear or a rotating relative movement can be applied for an estimation of the coefficient.
The surface force apparatus (SFA) is a first approach to measure forces between atomically smooth surfaces [7]. A piezoelectrical transducer approaches a surface to another surface which is held by a spring. Interaction forces on the very small nanometer scale (Van-der-Waals forces) can be measured by multiple beam interferometry.
Friction force microscopy (FFM) describes a special measuring setup where lateral friction forces on the atomic scale can be detected [8]. The basic idea is the approach of a wire with an infinitely fine tip to a surface. Deflections of the wire reflect forces at the tip-sample contact and can be detected for example by optical interferometry. In a first measurement, the relative movement between a tip and a graphite surface shows discontinuous jumps of the tip which is also denoted as atomic stick-slip [8].
The Prandtl-Tomlinson model is a first approach which describes the friction mechanism for a point-like tip inside the periodic potential of a surface [1]. A quasi-static movement of a single-atom tip dissipates energy during jumps from one stable position into the next stable position on the surface. In contrast, the point-like tip can also slide continuously in the conservative surface potential without stick-slip [9]. Superlubricity arises and energy dissipation does not take place.
The assumption of a single-atom tip is just a simplification and various conditions and parameters in the interpretation of FFM experiments have to be considered. For example, thermal vibrations of atoms due to a finite temperature can induce stick to slip jumps even in a resting period [10]. The material of tip and substrate, the load force, the temperature, the relative velocity and the real contact area of the tip are parameters which influence the interaction at the tip-surface contact [11].
A further development for friction measurements on the nanometer scale is dynamic friction force microscopy (dynamic FFM) [12]. In principle, the friction contact between a cantilever tip and an oscillating surface induces cantilever beam vibrations. This oscillation can be detected and provides insights into the dynamic interaction at the tip-sample contact.
Within this thesis a fractional resonance excitation technique in dynamic FFM is developed. Theoretical considerations and basic models to describe frictional interaction on the nanometer scale are presented first. In a second step, the experimental setup is introduced in detail. Furthermore, an innovative dynamic technique is presented which can measure the local friction force at the stick-to-slip transition of a tip on a surface. This technical approach can also be applied on graphite to investigate the constitution of surfaces. A topographical influence on the signal is investigated on metallic nanoparticles. Finally, surface defects like surface steps, grain boundaries and single-defects are revealed on the carbon model system HOPG.

2 Friction Force Microscopy

Nanotribology comprises fundamental concepts and experiments which describe frictional interactions between solids on the nanometer scale [1]. The invention of scanning probe techniques paved the way towards instruments which can measure interactions well below the physical limit of diffraction. Since the introduction of the atomic force microscope (AFM) by *Binnig et al.* [13], similar instrumental concepts and setups were designed to detect additional physical properties like friction. In this chapter, the experimental setup and applications of friction force microscopy (FFM) by *Mate et al.* [8] are presented which is one of the basic instruments to measure tribological interactions on the nanometer scale. Approaches and concepts describe basic properties of frictional interactions between a sharp tip and a sample surface.

2.1 The Friction Force Microscope

The contact area of two plane surfaces on the macroscopic scale depends on the apparent contact area. Taking a closer look, surface roughness on the micrometer scale reduces the area at the interface significantly (Fig. 2.1 (a)) and a multi-asperity contact impedes an interpretation of frictional interactions.
The contact between a sample surface and a single asperity is one of the basic ideas for friction measurements on the nanometer scale. A deeper understanding of friction interactions is principally based on the invention of friction force microscopy by *Mate et al.* [8]. They brought an etched tip of a tungsten wire into contact with a graphite sample and forced it across its surface. Deflections of the wire were detected by optical interferometry and gave a direct access to frictional interactions at the atomic scale.

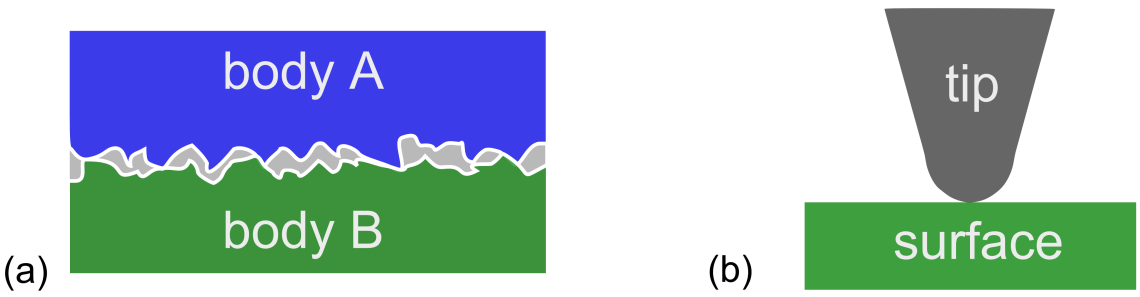

Figure 2.1: (a) The surface roughness on the micrometer scale decreases the contact area of two flat surfaces. (b) A well-defined contact between a tip and surface on the nanometer scale allows precise interpretations of friction measurements.

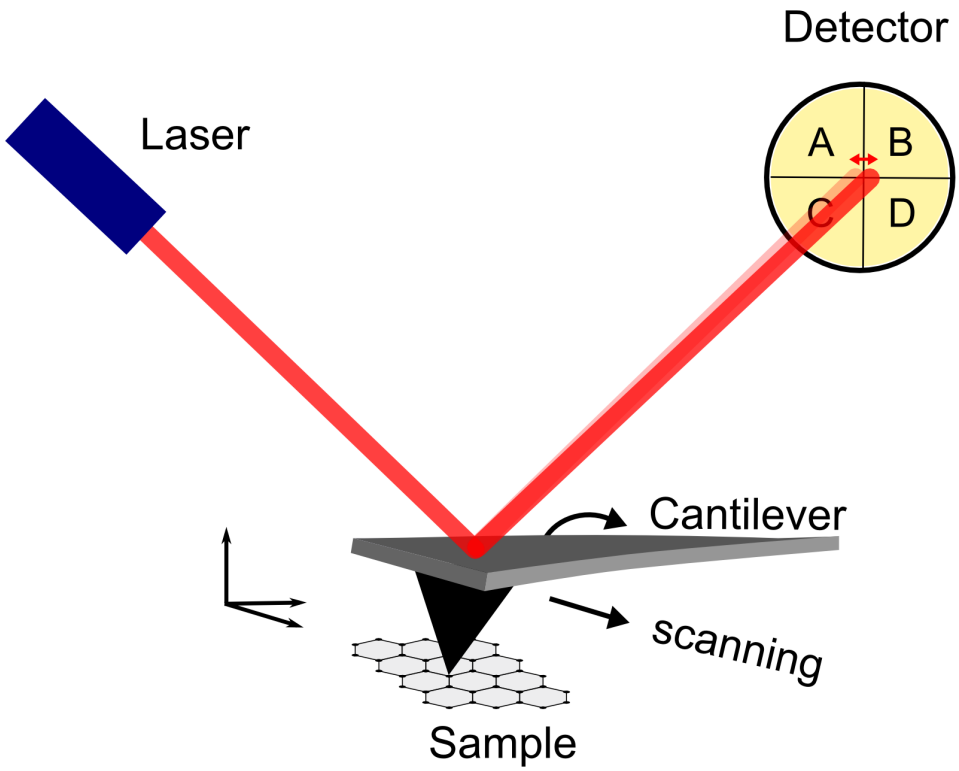

Figure 2.2: The basic setup of a friction force microscope. A cantilever reflects the interaction between a tip and a sample surface. A four-quadrant diode detects lateral deflections of a laser-pointer caused by friction forces at the contact. Furthermore, the vertical diode signal corresponds with the surface topography.

Nowadays, the tungsten wire is replaced by geometrically well-defined cantilevers. Depending on its application the lever can be shaped in various different ways. A typical friction force microscopy setup in Fig. 2.2 depicts a bar-shaped cantilever with a sharp tip at its end [14]. A laser pointer reflects lever deflections caused by lateral interactions between tip and surface and a four-quadrant diode separates topographical and frictional information depending on how laser intensity is distributed on the diode [15]. Friction corresponds with signal variations in lateral directions and is proportional to an intensity distribution on the individual diode quadrants according to

$$(A + C) - (B + D), \tag{2.1}$$

whereas the topography of a surface leads to vertical deflections and is proportional to a signal which corresponds with

$$(A + B) - (C + D). \tag{2.2}$$

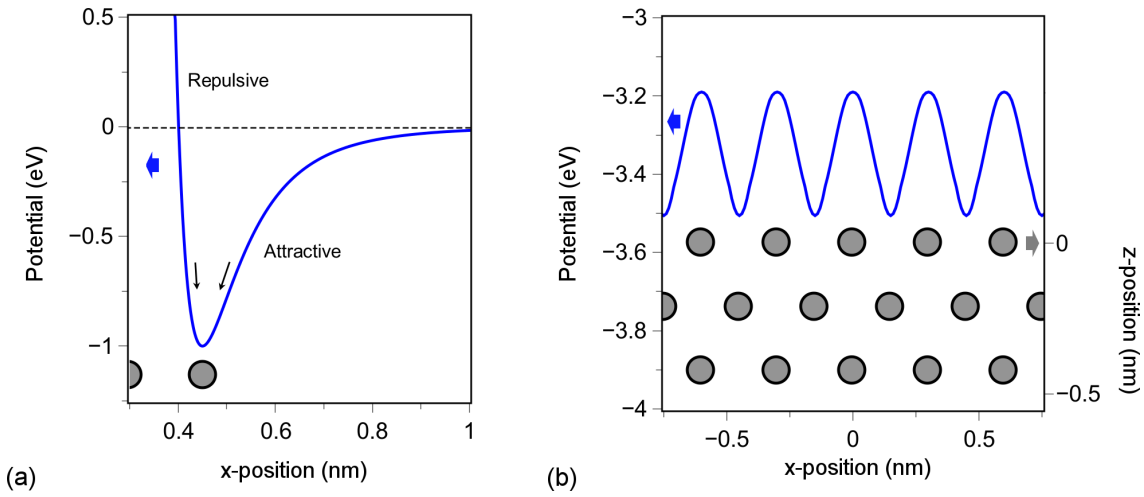

Figure 2.3: (a) The interaction force between two atoms depends on their distance r. Attractive and repulsive forces in the Lennard-Jones potential form an equilibrium position which is occupied by the atoms. (b) The atomic coordination of a crystalline solid (lattice constant $a = 0.3$ nm) leads to a lateral surface potential $V(x)$ with sinusoidal shape. Parameters for calculation are taken from [16] ($E_0 = 1$ eV, $r_0 = 0.45$ nm).

2.2 Point-Contact Friction

In friction force microscopy (FFM) the torsion of a cantilever usually reflects frictional interactions between tip and sample surface. An atomic corrugation of the surface and dissipative forces at the contact determine the friction signal. A simple approach describes atomic stick-slip movements of a point-like tip located inside a harmonic surface potential. The interactions can be used in Newton's equation of motion to describe the movement of the tip.

2.2.1 Lateral Surface Potential

When two atoms approach one another Fig. 2.3 (a), attractive and repulsive forces leave them in an equilibrium distance r_0. At higher distances electrostatic forces are present which attract the atoms. Contrarily, at smaller distances an overlap of their orbitals leads to a repulsive force. Depending on the distance $r = \sqrt{x^2 + y^2 + z^2}$, the phenomenological Lennard-Jones potential $V(r)$ describes the interaction energy

$$V(r) = E_0 \left(\left(\frac{r_0}{r} \right)^{12} - 2 \cdot \left(\frac{r_0}{r} \right)^{6} \right). \tag{2.3}$$

Several solids are built up of crystalline structures, where atoms are arranged periodically. A two-dimensional example presented by *Hölscher et al.* [16] determines the lateral potential $V(r)$ of an atom which approaches towards a surface. The interaction energy between all atoms i of the solid with a distance r_i has to be summed up

$$V(r) = \sum_{i}^{N} E_0 \left(\left(\frac{r_0}{r_i} \right)^{12} - 2 \cdot \left(\frac{r_0}{r_i} \right)^{6} \right). \tag{2.4}$$

The atom remains in its equilibrium z-position at the surface. Without any load force $F(z) = 0$ the first partial derivation of the potential $V(r)$ in z-direction equals zero at these locations

$$F(z) = -\frac{\partial V(r)}{\partial z} = 0. \tag{2.5}$$

In Fig. 2.3 (b) the resulting lateral sinusoidal potential $V(x)$ for each x-position of the surface is depicted. Conservative lateral forces affect the atom and are derived from the first partial derivation of the potential $V(r)$ in x-direction

$$F(x) = -\frac{\partial V(r)}{\partial x}. \tag{2.6}$$

For interpretations of experiments in friction force microscopy, it is often assumed that the last atom of a cantilever tip interacts with the lateral potential $V(x)$ of a surface [16]. A scanning movement of the cantilever tip leads to a periodically occurring interaction force which is caused by the atomic coordination of the sample material. A model describes the main properties of this interaction by taking relevant parameters into account.

2.2.2 Prandtl-Tomlinson Model

A basic model named after *L. Prandtl* and *G.A. Tomlinson* [17, 18] provides a simple approach to describe the movement of a cantilever tip in contact with the atomic potential of a surface (Fig. 2.4 (a)). A spring k_{eff} represents the stiffness of a point-like contact between cantilever tip and sample surface [19]. A support is connected with the spring and performs a scanning movement. Depending on the positions of support x_{support} and tip x in relation to the surface potential $V(x)$, the potential energy of the tip E_{tip} can be determined. If the support moves with constant velocity $x_{\text{support}} = v_{\text{x}} \cdot t$, the potential energy E_{tip} is given by

$$E_{\text{tip}}(x,t) = V(x) + 1/2 \cdot k_{\text{eff}}(x - v_{\text{x}} \cdot t)^2. \tag{2.7}$$

The conservative energy $E_{\text{tip}}(x)$ of the tip in a sinusoidal surface potential $V(x) = V_0/2 \cdot \cos(2\pi/a \cdot x)$ (Fig. 2.4 (b)) depends on the support x_{support} position, the lattice constant a and the atomic corrugation V_0. In a quasi-static case, the tip can rest motionless in positions, where conservative forces vanish

$$\frac{\partial E_{\text{tip}}}{\partial x} = 0, \tag{2.8}$$

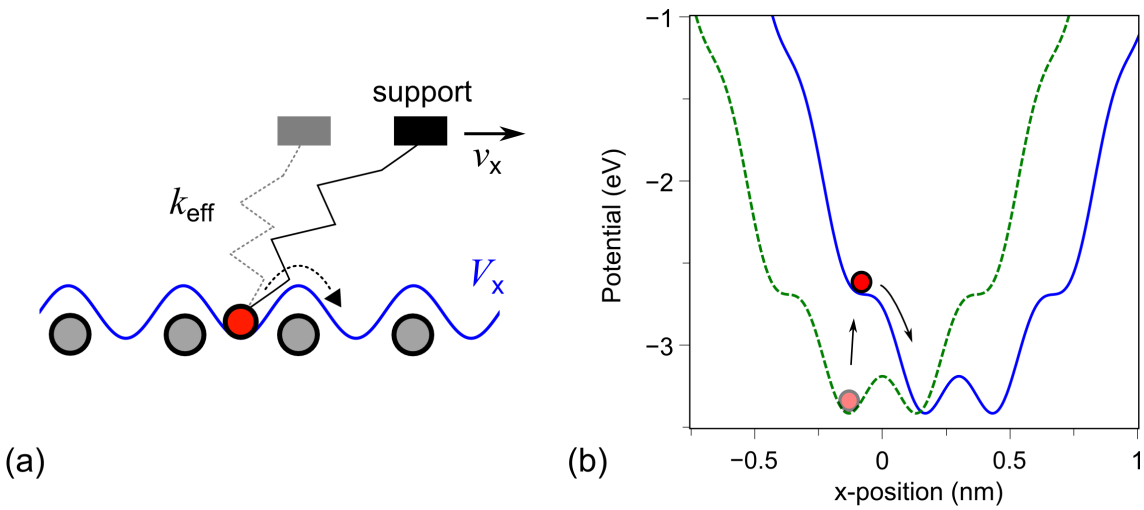

Figure 2.4: (a) Schematic illustration of the classical Prandtl-Tomlinson model. A point-like tip in contact with a surface is located inside a surface potential minimum ($\eta = 22.4 > 1$). A spring $k_{\text{eff}} = 0.5$ N/m pulls the tip across the surface and the tip fulfills atomic stick-slip movements. (b) The overall potential of surface and spring depicts local minima which get unstable due to a scanning movement of the support.

and the condition for a local minimum is fulfilled

$$\frac{\partial^2 E_{\text{tip}}}{\partial x^2} > 0. \tag{2.9}$$

A movement of the support leads to increased spring deflections and effects unstable rest positions. A jump of the tip into a next position is induced at potential saddle points, where the sign of the second derivative changes

$$\frac{\partial^2 E_{\text{tip}}}{\partial x^2} = 0. \tag{2.10}$$

The shape of the potential curve and number of potential minima in Fig. 2.4 (b) are influenced by different model parameters. Surface corrugation V_0, lattice constant a and especially the effective spring constant k_{eff} determine the factor

$$\eta = \frac{2\pi^2 V_0}{k_{\text{eff}}\, a^2}. \tag{2.11}$$

For $\eta > 1$, k_{eff} is in a moderate range compared to the surface potential and multiple local energy minima in the potential curve are present. The tip follows the support in a discontinuous way which is denoted as atomic stick-slip motion. In this case, critical positions x^*, where stick to slip can take place depend on the parameter η [20]

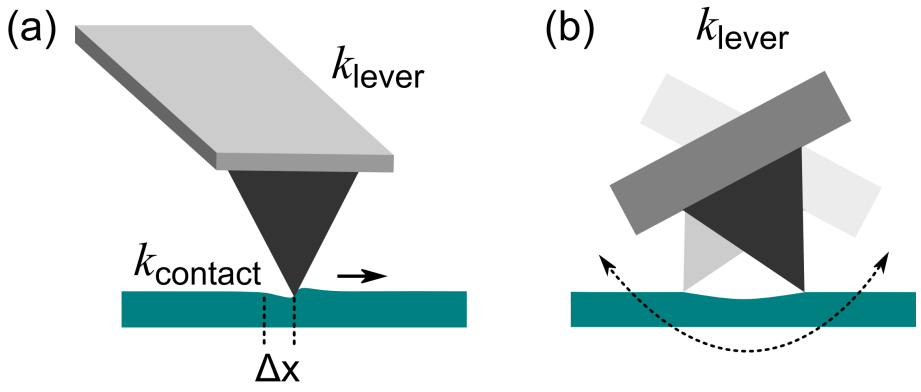

Figure 2.5: (a) A cantilever tip in contact with a sample surface during atomic stick-slip movement. The lever is almost relaxed due to its comparable high stiffness ($k_{\text{lever}} >> k_{\text{contact}}$) and the force to displace the contact is given by $k_{\text{contact}} \cdot \Delta x$. (b) Dynamic oscillations of the lever in contact with the surface. The resonance frequency f_{res} is mainly governed by the torsional spring constant k_{lever}.

$$x^* = \frac{a}{2\pi} \arccos\left(\frac{1}{\eta}\right). \tag{2.12}$$

In several publications the atomic stick-slip mechanism is successfully used to describe measured friction interactions for different experimental parameters and sample systems [8, 21, 22, 23, 24, 25].
In the case of a stiffer spring ($\eta < 1$), the spring force dominates the overall potential and atomic stick-slip is not possible. Multiple local minima are not present and Eq. 2.12 has no solution so that the tip slides continuously across the surfaces. It moves in a conservative potential without dissipation. Within this concept, *Socoliuc et al* [9] demonstrated vanishing dissipation experimentally for a silicon cantilever in contact with a NaCl(001) surface. Furthermore, an actuation of contacts can lead to vanishing friction interactions [26].

2.2.3 Effective Spring Constant

For a description of atomic stick-slip within the Prandtl-Tomlinson model, the effective spring constant k_{eff} of the contact between tip and sample is discussed by *Carpick et al.* [27]. In this approach the contact in experiments is built up of two virtual springs.
At first the sample surface is represented by a plane with a spring constant k_{contact} and secondly, the sphere of a tip is part of the cantilever with its own stiffness k_{lever}. Both springs are switched in series so that an effective spring constant k_{eff} results. The effective lateral stiffness of a contact between tip and surface is consequently given by

$$k_{\text{eff}} = \left(\frac{1}{k_{\text{lever}}} + \frac{1}{k_{\text{contact}}}\right)^{-1}. \tag{2.13}$$

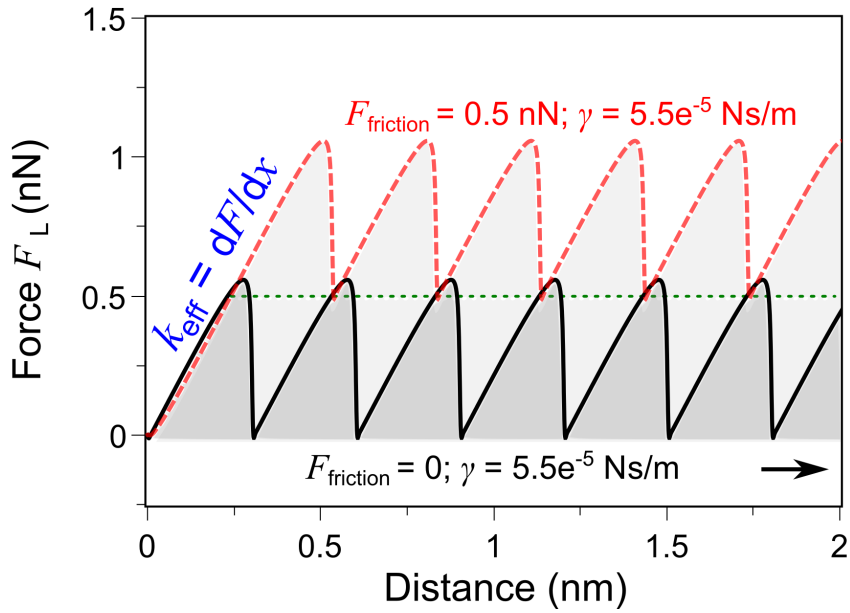

Figure 2.6: Simulated atomic stick-slip movement of a cantilever tip in the atomic potential of Fig. 2.3 (b). The point- like tip (m = $1 \cdot 10^{-10}$ kg) of an over-damped oscillator (black line) with k = 3 N/m is located at minima positions of the surface potential. Tip oscillations are suppressed by sufficient damping $\gamma = 5.5 \cdot 10^{-5}$ Ns/m. An increasing spring force during scanning ($v_x = 5 \cdot 10^{-7}$ m/s) leads to unstable potential minima positions and stick to slip movements occur. An additional constant friction force $F_{\text{friction}} = 0.5$ nN (red dashed line) leads to a force offset of atomic stick-slip and the amount of dissipated energy is increased.

A realistic contact stiffness is in the order of $k_{\text{contact}} = 1$ N/m [26]. In comparison, the lateral stiffness of a cantilever is in the order of 100 N/m. The effective spring constant consequently represents the contact stiffness [9]

$$k_{\text{eff}} \approx k_{\text{contact}}. \tag{2.14}$$

This description is extended in [28, 29], where the stiffness of the lever tip k_{tip} also contributes to the effective lateral stiffness.

2.2.4 Stick-Slip Simulation of a Point-like Tip

Atomic stick-slip represents a quasi-static motion of a cantilever tip on surfaces. During jumps from energetic higher to energetic lower levels in the conservative potential, the energy difference ΔE is instantaneously dissipated in the slip parts. Releasing phonons, as well as electronic excitations are responsible for dissipation [30]. Despite of an existing spring force k_{eff}, kinetic energy E_{kin} is not available during sticking and the tip remains motionless in its stable positions.
The time dependent movement of a point-like tip x_{tip} in Fig. 2.4 can be determined by Newton's equation of motion [31]. All acting forces are separated into conservative and dissipative forces for further discussions

$$m_{\mathrm{tip}} \cdot \ddot{x}_{\mathrm{tip}} = F_{\mathrm{conservative}} + F_{\mathrm{dissipative}}. \tag{2.15}$$

Spring force F_{spring} and lateral interaction force $F_x = -\partial V(x_{\mathrm{tip}})/\partial x_{\mathrm{tip}}$ form the conservative part of the equation

$$F_{\mathrm{conservative}} = k_{\mathrm{contact}} \left(x_{\mathrm{support}} - x_{\mathrm{tip}}\right) - \frac{\partial V(x_{\mathrm{tip}})}{\partial x_{\mathrm{tip}}}. \tag{2.16}$$

In this presentation the equation describes a simple harmonic oscillator which is located inside the atomic interaction potential. If kinetic energy is present, the tip vibrates inside the conservative potential without dissipation. The tip oscillation slows down when frictional energy losses come into effect. A velocity-dependent friction constant γ can be introduced which opposes the direction of motion and describes viscous damping [31]

$$F_{\mathrm{dissipative}} = -\gamma \cdot v_{\mathrm{tip}}. \tag{2.17}$$

Except from the surface potential interaction, a linear damped oscillator results. This approach has been successfully used to describe several results and aspects of friction measurements on the nanometer-scale [2, 32, 33]. In order to suppress oscillations of the tip during support movements v_{x}, critical damping of the spring-tip system can be considered [31]

$$\gamma = 2 \cdot \sqrt{m_{\mathrm{tip}}\, k_{\mathrm{eff}}}. \tag{2.18}$$

In Fig. 2.6 a numerical integration of the equation depicts an example for a calculated atomic stick-slip movement. A movement of the support v_{x} forces the point-like tip across the surface potential of Fig. 2.3. For an over-damped system (black line) the tip sticks to the surface until the spring force pulls it out of the surface potential minima. The gradient of the slopes during sticking represents the lateral stiffness $\mathrm{d}F/\mathrm{d}x = k_{\mathrm{eff}}$ of the contact [29, 27, 28]. The enclosed area corresponds with dissipated energy caused by viscous damping during the slip parts of the tip motion.
Zwörner et al [34] revealed that friction on different carbon compounds is independent of velocity v_{x} concerning a wide range of sliding speeds. Derived from the macroscopic description of Coulomb friction, as presented for example by *McMillan* [35], a constant friction value $F_{\mathrm{friction}} \geq 0$ can additionally affect the tip during sliding

$$F_{\mathrm{dissipative}} = -F_{\mathrm{friction}} \cdot \mathrm{sgn}\left(v_{\mathrm{tip}}\right) - \gamma \cdot v_{\mathrm{tip}}. \tag{2.19}$$

In Fig. 2.6 the dashed red line represents a quasi-static tip movement. The spring is initially preloaded caused by the constant friction force F_{friction} before the tip jumps out of stable positions. Atomic stick-slip sets in and the amount of dissipated energy is increased. This approach of tip and surface interactions captures the essential parameters to simulate atomic stick-slip movements.

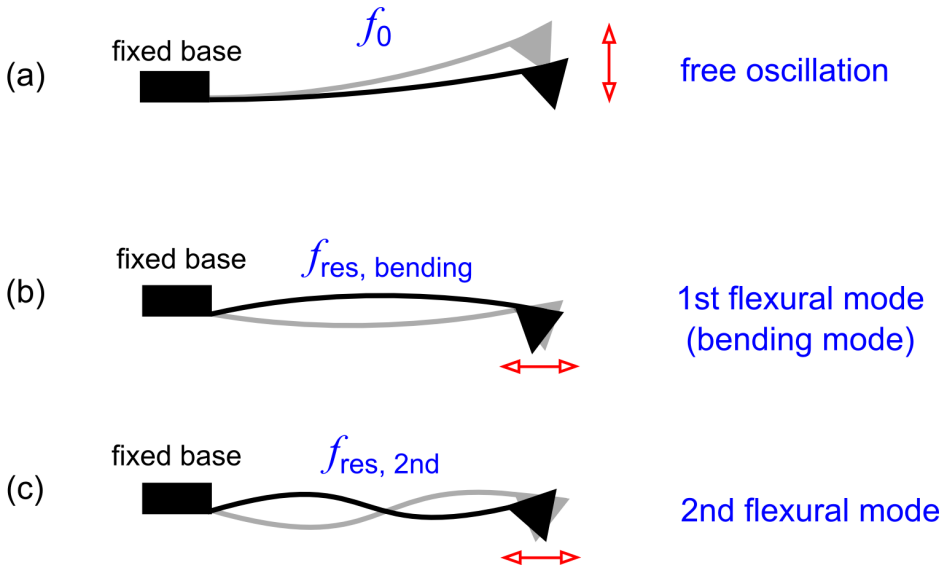

Figure 2.7: Free oscillation of a cantilever beam (a). Dynamic excitations lead to vibrations of torsional or flexural eigenmodes. Two flexural modes are depicted for a cantilever which is clamped at both ends (b, c). Depending on the excitation frequency in longitudinal direction the first, the second, as well as higher eigenmodes (not shown) can be brought into resonance.

2.3 Vibrations of Cantilever Eigenmodes

In principle, a cantilever is a vibratory bar with specified resonance frequencies f_{res} for each vibrational mode (Fig. 2.5 (b)) [36, 37, 38, 39]. In dynamic atomic force microscopy (dAFM) for example, a dither piezo at the base of a cantilever can excite resonance vibrations of a specific eigenmode while the tip interacts with the surface potential [37].
In contact resonance microscopy (CR-AFM) furthermore, surface vibrations excite lever oscillations to measure elastic properties of sample surfaces [40, 41]. The sensitivity of dynamic measurements can be increased if the cantilever oscillates around its torsional or flexural eigenmodes [40].
Depending on the excitation direction and frequency, different torsional or flexural modes can be brought into vibration. Mechanical properties, geometry of the lever, as well as experimental boundary conditions govern the exact resonance frequencies. In Fig. 2.7 (b, c) two flexural modes are depicted which can be used for excitations in dynamic friction force microscopy.
However, up to now, attention is focused on a tip of an almost relaxed cantilever in contact with the atomic potential of a sample surface. Vibrations during sliding over a surface are suppressed due to frictional damping. As a first step towards an appropriate description of dynamic excitations in friction force microscopy, one can consider a cantilever tip which is deflected several nanometers from its equilibrium position. The conservative spring force stores potential energy in the spring-tip system and dominates the interaction. In this case the tip oscillates around its equilibrium position and the dynamic movement of the tip is determined by mechanical properties of the corresponding lever mode.
In a realistic case, friction interactions at the tip-sample contact lead to losses of mechanic energy and cause a decay of the oscillation amplitude. Parameters like load force and

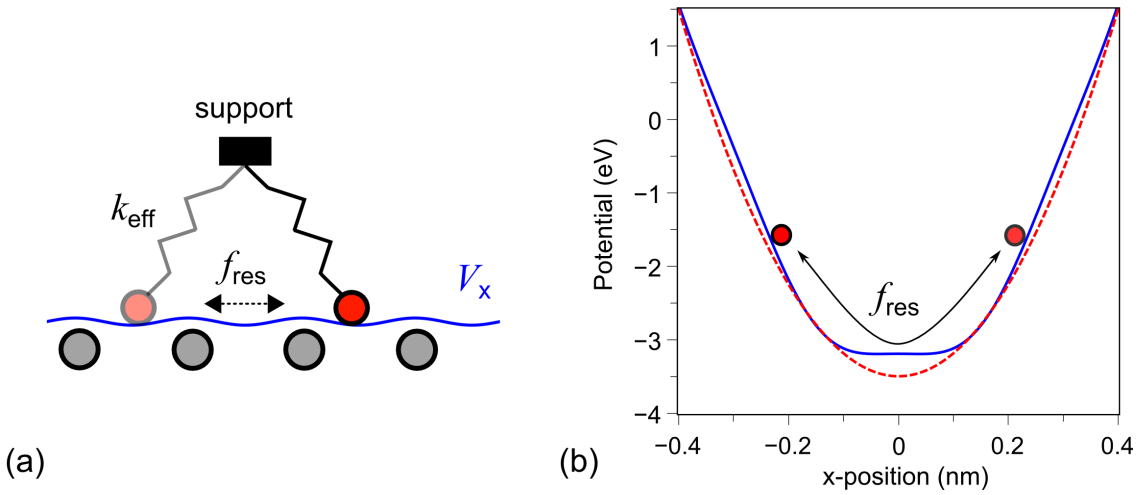

Figure 2.8: (a) An increased spring constant $k_{\text{eff}} = 10$ N/m reduces the influence of the atomic potential ($\eta = 1.12 \approx 1$). (b) A point-like tip oscillates over the surface, where the overall potential converges towards the potential of the spring force. A contribution of the surface potential can be neglected with increasing spring constant.

contact area influence friction interactions in experiments [11].

2.3.1 Simulation of Dynamic Cantilever Oscillations

For simulations of dynamic oscillations of cantilever eigenmodes, the equation of motion can be modified, where the effective spring constant k_{eff} describes the stiffness k_{lever} of the corresponding mode

$$k_{\text{eff}} = k_{\text{lever}}. \tag{2.20}$$

The tip oscillates around its equilibrium point and positions x_{tip} are consequently derived from

$$m \cdot \ddot{x}_{\text{tip}} = -k_{\text{lever}} \cdot x_{\text{tip}} - \frac{\partial V(x_{\text{tip}})}{\partial x_{\text{tip}}} - F_{\text{friction}} \cdot \text{sgn}\,(v_{\text{tip}}) - \gamma \cdot v_{\text{tip}}. \tag{2.21}$$

In this context, an important aspect has to be addressed which relates to the linearity of the system. Besides a possible contribution of the surface potential, the discontinuous sgn-function evokes a non-linear equation of motion and can describe non-linear oscillations [42].
The equation of motion Eq. 2.21 is used to simulate a tip oscillation (Fig. 2.9) in the atomic potential. A spring $k_{\text{lever}} = 175$ N/m is connected with a support (Fig. 2.8) and an initial deflection of $x_0 = 5$ nm leads to an oscillation of the point-like tip. Energy

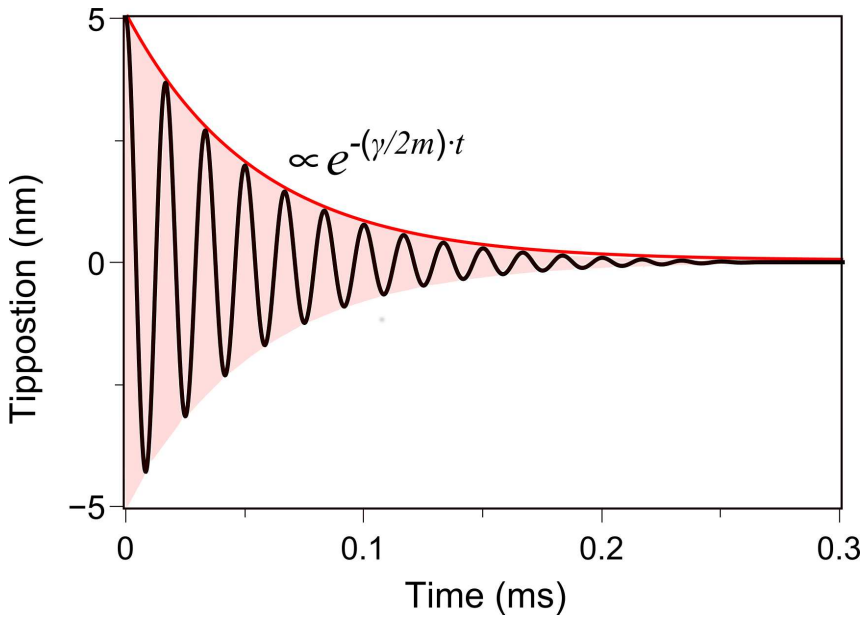

Figure 2.9: Amplitude envelope for an oscillation of a point-like tip $m = 1.23 \cdot 10^{-9}$ kg inside the atomic potential of Fig. 2.3. The spring force (k = 175 N/m) leads to an oscillation at its natural frequency and the amplitude decreases due to damping ($\gamma = 4.5 \cdot 10^{-5}$ Ns/m, $F_{\text{friction}} = 0.5$ nN).

dissipation causes a decay of the oscillation amplitude. Taking the exponential decay rate δ into account

$$\delta = \frac{\gamma}{2 \cdot m}, \tag{2.22}$$

the tip amplitude can be described as a function of time t

$$x_{\text{tip}} = x_0 \, e^{-\delta t} \cos(2\pi \, f_{\text{res}} \cdot t). \tag{2.23}$$

The tip reaches high velocities during oscillation and dissipation is obviously dominated by the viscous damping parameter γ. A comparably small constant friction force F_{friction} is negligible in this case and the atomic potential has no further influence on the oscillation. For this reason, energy losses during oscillations can be determined. Potential energy E which is stored in the spring behaves proportionally to the square of the oscillation amplitude. Taking account of the exponential decay rate δ, energy dissipation per time unit is consequently given by

$$\frac{\mathrm{d}E}{\mathrm{d}t} = \dot{E} = -2 \cdot \delta \cdot E. \tag{2.24}$$

The Q factor describes a ratio of stored energy in the system in relation to energy losses during one oscillation cycle [43]

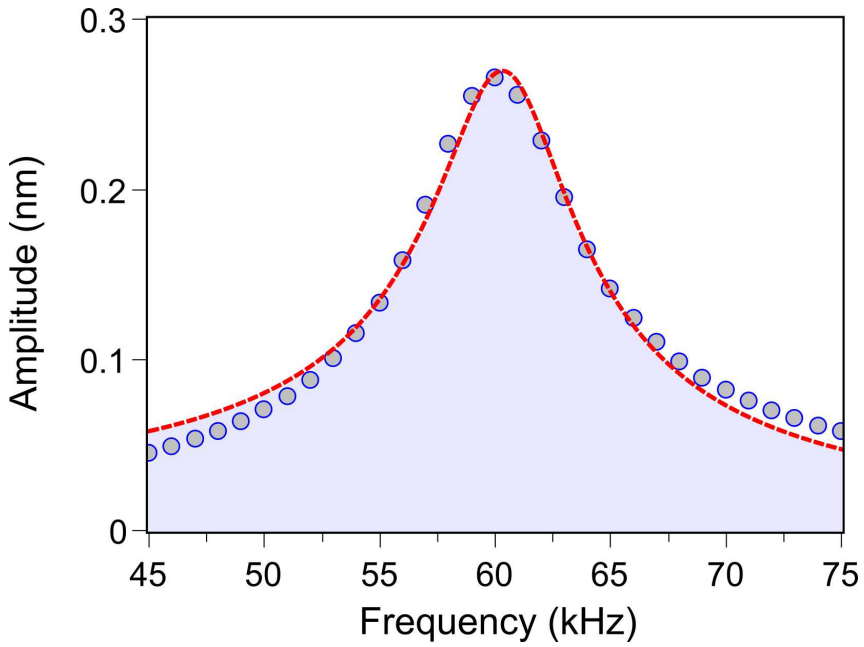

Figure 2.10: A fast Fourier transformation of the temporal oscillation in Fig. 2.9. The width of the distribution is directly related to energy losses at the tip-surface contact. A fitted Lorenz curve exhibits useful information like the quality of the system ($Q = 10.2$).

$$Q = \frac{E \cdot \omega}{-\dot{E}} = \frac{\omega}{2 \cdot \delta} = \frac{2\pi \cdot f \cdot m}{\gamma}. \tag{2.25}$$

The quality factor Q is often used to specify damping in mechanical systems. In Fig. 2.10 a fast Fourier transformation of the exponential decay exhibits a distribution of the Fourier components around the resonance frequency f_{res}. The width of the distribution is directly related to damping, respectively the quality factor Q of the oscillation [44].
For a detection of quality factors in FFM experiments, experimental methods can be applied which exhibit and analyze oscillation responses of cantilevers within an adequate frequency band.

2.3.2 Dynamic Excitations of Cantilever Oscillations

In Fig. 2.9 the oscillation is left to its own resources and decreases due to damping. The resonance curves of mechanical systems like cantilevers can be investigated in experiments for a detection of damping. For example, a series of single-frequency modulations covering a frequency range around the resonance is usable to measure the amplitude response [44]. The amplitude distribution $A(\omega)$ around the free resonance frequency $\omega_{\text{res}} = 2\pi f_{\text{res}}$ is described by a Lorenz curve [45]

$$A(\omega) = \frac{F_0/m}{\sqrt{(\omega_{\text{res}}^2 - \omega^2)^2 + (\omega \cdot \omega_{\text{res}}/Q)^2}}, \tag{2.26}$$

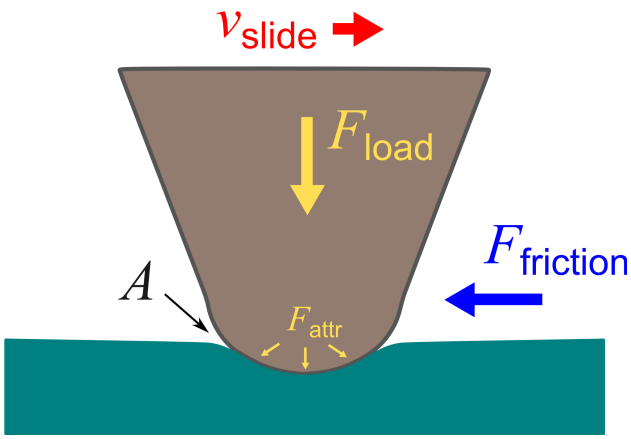

Figure 2.11: A single-asperity contact between a cantilever tip and surface leads to deformations and an increased contact area. Lateral friction depends on experimental parameters like load force, adhesion and mechanical properties of tip and surface.

where F_0 corresponds with an external driving force and m with the effective mass of the system. In Fig. 2.10 this function is fitted to the components of the Fourier transformation and Q factors in experiments can be extracted from derived data in this way.
The phase relation between excitation and oscillation is given by

$$\tan\phi = \frac{\omega \cdot \omega_{\text{res}}/Q}{\omega_{\text{res}}^2 - \omega^2}. \tag{2.27}$$

In conclusion, the dynamic treatment of Eq. 2.21 provides a basis for interpretations of experimental data in dynamic friction force microscopy. Here, dissipative friction forces between tip and surface govern the oscillation, whereas a contribution of the atomic potential can be neglected. However, one has to note that the picture of a point-like tip in contact with the atomic potential of a surface is rather simplified.
For a better understanding of results, a more comprehensive and improved description of the contact between tip and surface is required.

2.4 Friction depending on the Contact Properties

Realistic contact areas in friction force microscopy are in the range of several nanometers to tens of nanometers. These dimensions involve thousands of atoms which determine interactions between tip and sample. In order to overcome the simplified approach of a point-like contact, further frictional aspects have to be considered. Adhesive forces and structural lubricity for example influence lateral forces at the interface.

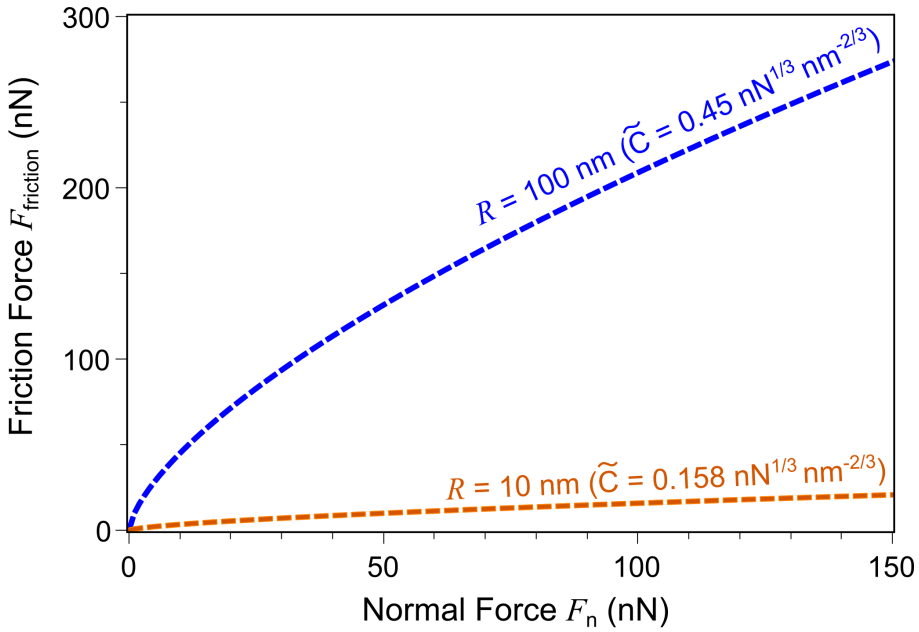

Figure 2.12: Friction forces, depending on normal forces, are illustrated for two different contact radii R and experimentally found coefficients $\tilde{C}$ in [46]. Small friction forces result for a small tip on a clean amorphous carbon surface under argon atmosphere. Higher friction results in the cases of an increased tip radius on amorphous carbon under ambient conditions.

2.4.1 Contact Area between Tip and Surface

A cantilever tip in contact with a sample surface performs pressure to the surface and consequently deforms the surface elastically. Mechanical stress depends on the load force F_{load} and deformations of the surface (Fig. 2.11) increase the contact area A_{cont}.
Taking account of adhesive forces between tip and surface, *Schwarz et al.* [46] investigated lateral friction forces F_{friction} on different carbon compounds within the Hertz-plus-offset model. Here, the contact area A_{cont} between a flat surface and the sphere of a tip apex is described by

$$A_{\text{cont}} = \pi \left(\frac{R F_{\text{n}}}{K} \right)^{2/3}, \tag{2.28}$$

where R is the tip radius. The elastic modulus K of the contact is determined by Young's moduli E and the Poisson ratio ν of tip and surface

$$K = \frac{4}{3} \left(\frac{1-\nu_{\text{tip}}^2}{E_{\text{tip}}} + \frac{1-\nu_{\text{surf}}^2}{E_{\text{surf}}} \right)^{-1}. \tag{2.29}$$

Besides the load force, additional attractive forces F_{attr} on this scale come into effect and have to be considered

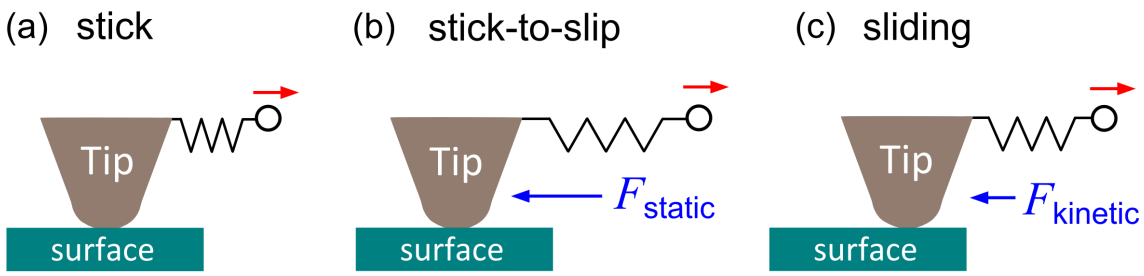

Figure 2.13: The transition from static to sliding friction. (a) A tip sticks to a surface and a spring force (b) starts to pull it out of its resting position. The tip starts to slide after static friction F_{static} was reached and the force F_{slide} which maintains a sliding with constant velocity is smaller.

$$F_{\text{n}} = F_{\text{load}} + F_{\text{attr}}. \tag{2.30}$$

Friction performs shear stress onto the surface which is defined by the frictional force per unit area

$$S = F_{\text{friction}}/A_{\text{cont}}, \tag{2.31}$$

These considerations and contact parameters determine lateral friction forces F_{friction}

$$F_{\text{friction}} = \pi S \left(\frac{R}{K}\right)^{2/3} F_{\text{n}}^{2/3} = C F_{\text{n}}^{2/3}. \tag{2.32}$$

For the sake of simplicity, the authors introduced a size-independent coefficient which describes an effective friction coefficient $\tilde{C}$ for a point-like single asperity

$$F_{\text{friction}} = C F_{\text{n}}^{2/3} = \tilde{C} R^{2/3} F_{\text{n}}^{2/3}. \tag{2.33}$$

Fig. 2.12 illustrates the dependence of lateral friction on normal forces. Besides material properties and constitutions of sample surfaces, especially the load force F_{load} is an important parameter to adjust a requested range of lateral friction in experiments.

2.4.2 Static and Sliding Friction

The force F_{static} to pull a macroscopic body out of its resting position is generally increased, compared to the force which affects the body F_{sliding} during sliding. The static friction coefficient is increased compared to the sliding friction coefficient

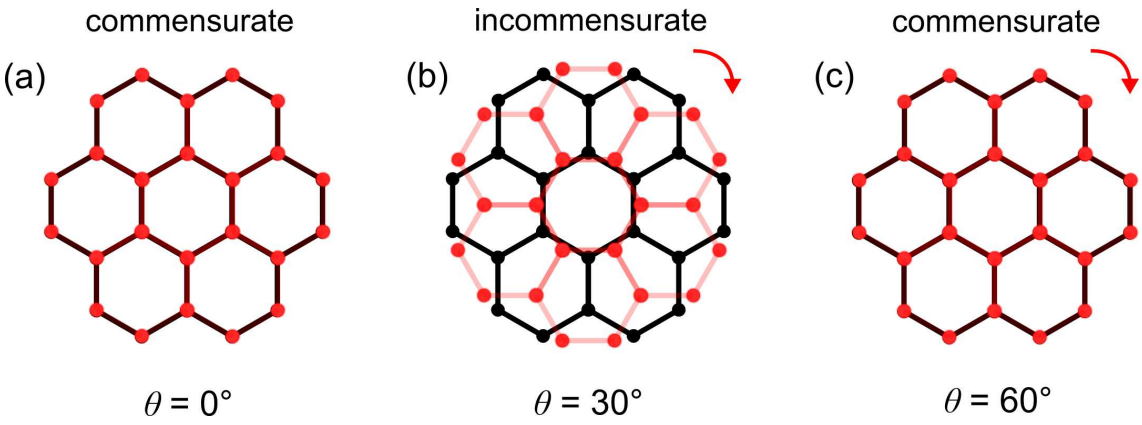

Figure 2.14: The frictional interaction between two graphite flakes depends on their relative orientation. If the honeycomb structures are aligned with respect to their 60° symmetry, sliding is described by a collective stick-slip movement of atoms (a, c). Flakes slide across each other without energy dissipation in an incommensurate case (b).

$$\mu_{\text{static}} > \mu_{\text{sliding}}. \tag{2.34}$$

Recently, microscopy experiments on the nanometer scale were performed to measure static and sliding friction between specialized and well-characterized surfaces. *Dietzel et al.* [47] measured the transition from static to sliding friction of nanoparticles on graphite surfaces and found a constant ratio of one half which is also theoretically predicted [48].
Frictional aging describes a dependence of static friction on the resting time between two bodies [49]. *Li et al.* [50] conducted several slide-hold-slide experiments between silicon tips and silicon wafers. The tip was brought into contact with the surface and the hold time for the transition from static to sliding friction was continually raised. They found that lateral friction increases with the logarithm of hold time and indicates a time dependence of static friction.
An increasing area at the interface with time due to creep of microcontacts (geometric aging) is one possible explanation for frictional aging [5]. *Liu et al.* [51] showed that a chemical origin can also explain an aging process of contacts, where covalent bonding leads to a logarithmically dependence of static friction with time.

2.4.3 Sliding Friction - Structural Lubricity

The contact area A_{contact} between two surfaces on the nanometer scale involves a large number of atoms. Surface atoms of crystalline materials are arranged in periodic arrays with defined lattice structures.
Frictional anisotropy and structural lubricity can affect the interaction when two materials slide over each other [52, 53, 54]. If lattice structures are equal and perfectly aligned, an interlocking of surfaces results and the interaction is described by a collective stick-slip movement of surface atoms [55].

Friction vanishes during sliding, if surface structures mismatch and an incommensurable contact results [56]. Energy dissipation does not take place and each surface atom follows its equilibrium position adiabatically [57].
Dienwiebel et al. [55] performed angle-dependent measurements on graphite where friction was detected for different orientations. A graphite flake was attached to the tip of a specialized cantilever and forced across the surface. The friction signal revealed angular distances of 60° between narrow regions which showed significant friction forces in contrast to wide ranges with vanishing small friction. The authors used the flake scenario, presented in Fig. 2.14, to describe the frictional anisotropy in their experiment.

2.5 Conclusion

In friction force microscopy (FFM) the torsion of a cantilever usually reflects frictional interactions between a tip and a sample surface. The Prandtl-Tomlinson model is a basic approach which describes quasi-static stick-slip movements of the tip caused by the atomic corrugation of the surface. The tip rests motionless in position of surface potential minima during scanning. If the spring force of the cantilever exceeds a critical value, a jump of the tip into a neighboring minima occurs. The tip follows the scanning movement in a discontinuous way, which is also denoted as atomic stick-slip.
A different approach is required for a description of dynamic oscillations of cantilever eigenmodes. The frequency of the oscillation is determined by the spring constant of the corresponding lever mode and the total kinetic energy does not dissipate instantaneously. Frictional interactions with a sample surface lead to damping of the oscillation and typical properties of vibrations like resonance frequency f_{res} and quality factor Q can be extracted.
A realistic interface on the nanometer scale consists of a large number of atoms. Load forces can deform surface and tip elastically, which influence lateral friction forces. The atomic coordination of surfaces can affect lateral interactions (structural lubricity) and can lead to friction anisotropy. The size and constitution of the interface between tip and surface, as well as the resting time can furthermore influence static friction and frictional aging.

3 Dynamic Friction Force Microscopy - Principle and Setup

The basic setup to detect frictional properties of a sample surface by using dynamic friction force microscopy is specified in the following chapter. After the principle of excitation is discussed in a first step, the ultra-high vacuum (UHV) chamber which is used as experimental environment is presented. Furthermore, the microscope itself including drive technology and detection technique is introduced. Experiments which are performed throughout this thesis required an improved scanning unit (AFM head) which is designed and manufactured within our work group. Moreover, the chapter also focuses on properties of the cantilever used as force sensor, electrical driving signals, as well as signal processing techniques.

3.1 Principle of Dynamic Friction Detection

In dynamic friction force microscopy a cantilever tip is brought in contact with a sample surface for a detection of frictional properties on the nanometer scale [12]. Resulting forces in Fig. 3.1 (a), acting in vertical direction with respect to the cantilever, provoke a normal deflection of the lever. Thus, the topography of a surface can be scanned [14].
Dynamic frictional interactions can act in lateral or longitudinal direction with respect to the cantilever beam. Accordingly, friction provokes the lever to fulfill torsional or bending deflections. In our case bending deflections, respectively bending oscillations at the first flexural mode (bending mode) caused by a dynamic excitation in Fig. 3.1 (b), are used as a force indicator.
The sample is modulated by an electrical signal for the dynamic excitation of lever bending

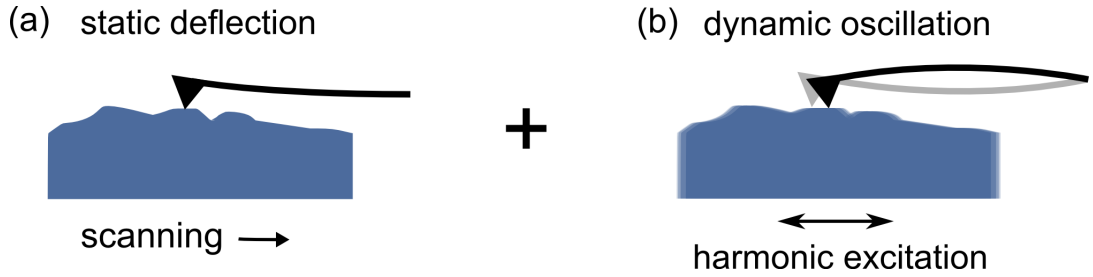

Figure 3.1: The principle of dynamic friction force microscopy: (a) The contact interaction of the tip and a sample surface leads to a static deflection of the cantilever beam which is linked with the topography. (b) The dynamic excitation of the lever bending mode is a measure of the friction interaction between tip and sample.

oscillations. In a simple case as an example, a fixed amplitude and frequency induce a harmonic surface movement. Oscillation characteristics are mainly governed by mechanical properties of the bending mode and excitation parameters, as well as the acting friction force between tip and surface.
Different modes of excitation are possible concerning the resonance f_{res} of the lever bending mode. An off-resonance excitation technique, applying a modulation frequency far below the resonance $f_{\mathrm{mod}} < f_{\mathrm{res}}$, can acquire local friction loops [12, 58]. A detailed oscillation analysis by stimulating the resonance f_{res} of the lever provides a direct access to damping properties of the tip-sample contact [59, 60].
One central aspect of this work is the development and application of an advanced modulation and analysis technique. The off-resonance modulation is fulfilled with an integer fraction of the resonance frequency f_{res}. A non-linear interaction at the contact excites bending resonance oscillations of the lever beam. Applying this new approach, quantitative friction information of a sample surface can be derived.

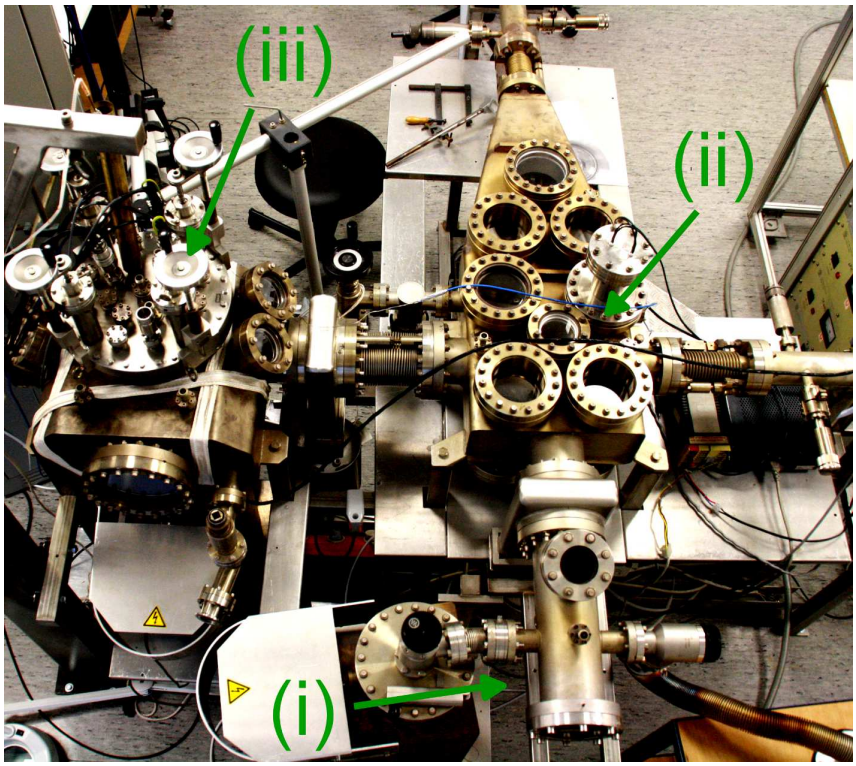

Figure 3.2: The setup of the ultrahigh vacuum (UHV) system is partitioned into three subchambers (i - iii). The sample is fed trough a load lock chamber (i) for the transfer from ambient conditions to vacuum conditions. Procedural steps like storage of samples and preparation of sample surfaces can be realized inside the preparation- and transfer chamber (ii). On top of the chamber a Knudsen cell for physical vapor deposition in UHV is mounted. Finally, friction force measurements on the nanometer scale are performed in the microscope chamber (iii).

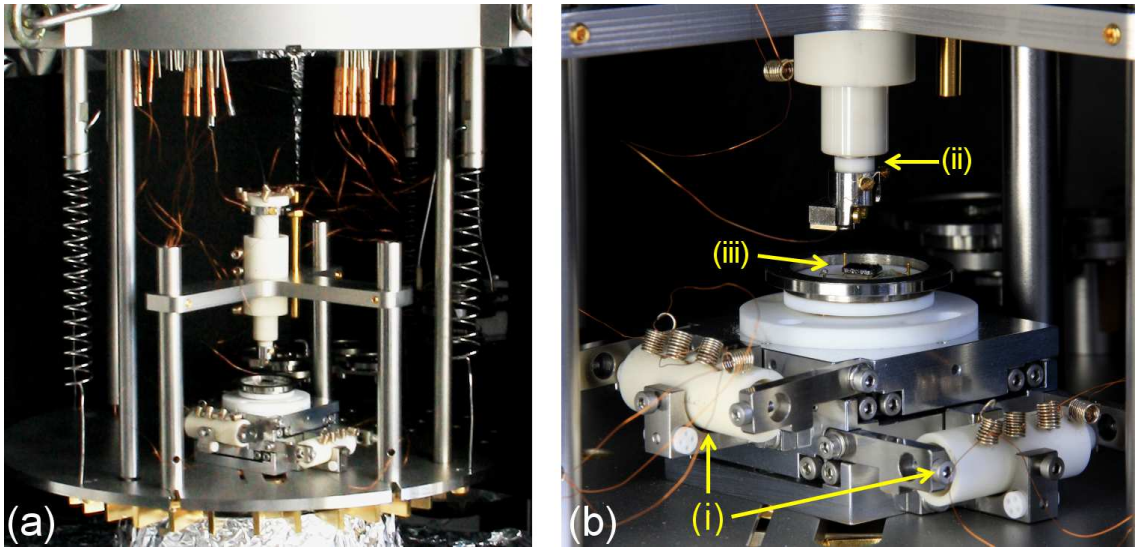

Figure 3.3: (a) The friction force microscope is attached to three springs which belong to an eddy current damping system. The damping magnets are placed underneath the microscope plate. (b) Two inchworm drives (i) enable the rough positioning of the sample in x- and y-direction with respect to the scanner unit. A third inchworm drive (ii) approaches the probe head to the sample surface in z-direction. The scanner tube is placed inside the drive tube and realizes the scanning movement of the AFM probe head during measurements. The sample is glued on a modulation piezo (iii) and placed on top of the sample plate.

3.2 Ultrahigh-Vacuum (UHV) Experimental Environment

Working at a base pressure of 10^{-9} millibar, a former industrially used ultra-high vacuum chamber was re-built for scientific use [61]. The system mainly consists of three chambers with different task areas. In order to introduce a sample into the vacuum, it is fed through the load-lock chamber (i) in Fig. 3.2. The sample passes through the transfer and preparation chamber for preparations and optional manipulations like physical vapor deposition or heating of the surface (ii). Finally, the sample is brought into the microscope chamber (iii) for experimental studies. UHV-gate-valves separate the three chambers and different working steps can be executed simultaneously under ultrahigh-vacuum conditions. The microscope is placed on a damping system to decouple building and ground vibrations. Electrical supplies like piezo and detection electronics are placed outside the chamber.

3.3 The Microscope

Surface measurements on the nanometer scale are performed by using a home-built atomic force microscope (AFM). The sample is placed on top of two inchworm drives which can move the sample in longitudinal x- and lateral y-direction with respect to the measurement sensor (Fig. 3.3). A third inchworm drive can approach the AFM head unit to the sample surface for a rough positioning.
The AFM head, containing cantilever and detection technique, is attached to a piezo tube

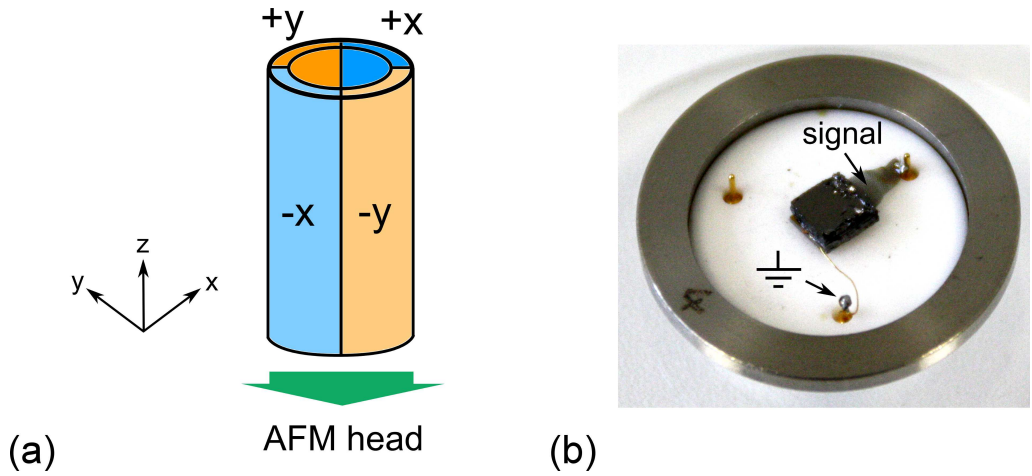

Figure 3.4: (a) Schematic illustration of a scanner tube. Bi-polar voltages applied to the electrodes of the tube quarters induce defined piezoelectric tube deflections in x- and y-directions. Mixing of x- and y-voltages leads to an expansion or contraction in z-direction. (b) The sample is placed on top of the sample plate which furthermore contains the electrical connections for the modulation piezo.

inside the inchworm drive (not visible in Fig. 3.3). The tube provides scanning movements of the head in x- and y-direction, as well as fine positioning in z-direction onto the sample surface.
The sample is glued to a modulation piezo for a modulation movement of the surface. The movement direction is aligned to the long-axis direction of the cantilever.

3.3.1 Fiber Interferometer

A fiber interferometer is applied to detect the static deflection and dynamic oscillation of the cantilever beam due to force interactions between tip and surface (Fig. 3.1) [62, 63]. The design of the interferometer is based on a fiber coupler, first presented by *Rugar et al.* [64]. Light is emitted from a laser diode (wavelength $\lambda = 780$ nm) and is brought into the coupler (Fig. 3.5). Light couples through a second fiber in propagation direction due to a splicing of single-mode fibers and is emitted at both end faces of the coupler. At one end a reference diode detects the light intensity and the other end is fixed above the cantilever beam. Light is reflected back into the fiber from the cleaved end face, as well as from the back of the cantilever beam. A path length difference $2 \cdot d$ concerning the distance from fiber end face to the lever beam occurs and both light components interfere with each other. Because of a minor reflection at the glass-vacuum interface, interference fringes can be described by a simple two-beam interference [65, 66]. The light propagates back and is detected from the detection photodiode. The intensity is converted into a proportional voltage signal U_{sig}. In order to avoid signal offsets, caused by a difference in the intensity of the reflected components, the reference diode signal is used to adjust the signal around the zero position. Thus, intensity fluctuations of the laser diode are also eliminated. Taking the voltage amplitude

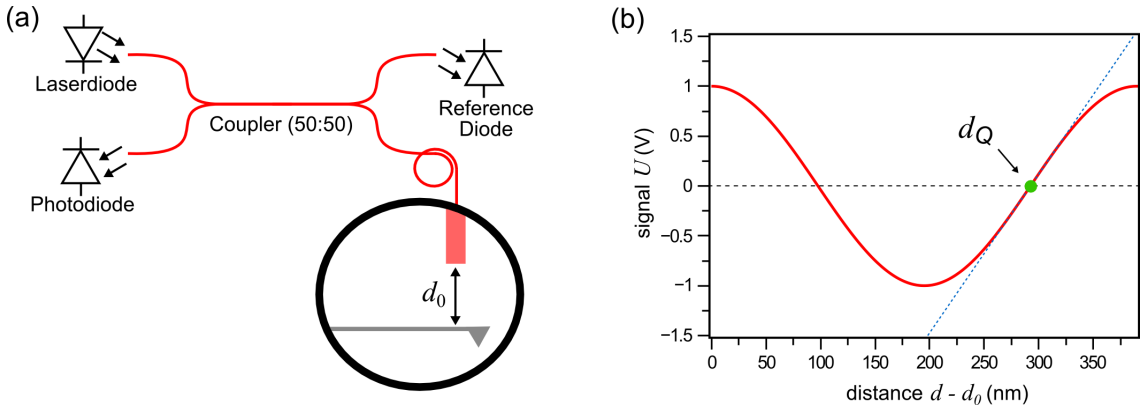

Figure 3.5: (a) A fiber coupler constitutes the essential part of a fiber interferometer. The light of a laser diode is brought into the coupler and propagates towards the cantilever. The light components reflected from the cantilever back side and fiber end face interfere with each other. The interference intensity propagates back and is detected by the detection photodiode. (b) The interferometer signal is described by two beam-interference, where the intensity depends on the distance d between fiber end face and cantilever. In the distances of d_Q signal variations are maximized and proportional to distance variations Δd.

$$U_0 = \frac{U_{\max} - U_{\min}}{2}, \tag{3.1}$$

and diode wavelength λ into account, the signal U_{sig} depends on the distance d between fiber end face and cantilever

$$U_{\text{sig}} = U_0 \cos \frac{4\pi \cdot d}{\lambda}. \tag{3.2}$$

At the periodically arranged quadrature points

$$d_Q = n \cdot \frac{\lambda}{8} \text{ with } n = 1, 3, 5, ..., N, \tag{3.3}$$

the maximum sensitivity with respect to the distance d can be derived from the derivation of the cos-function. Signal variations ΔU_{sig} are proportional to variations of the distance Δd. Taking the wavelength λ

$$s_\lambda = \frac{\lambda}{4\pi}, \tag{3.4}$$

and the amplitude U_0 into account, for a first approximation variations ΔU_{sig} are given by

$$\Delta U_{\text{sig}} = U_0 \cdot s_\lambda^{-1} \cdot \Delta d. \tag{3.5}$$

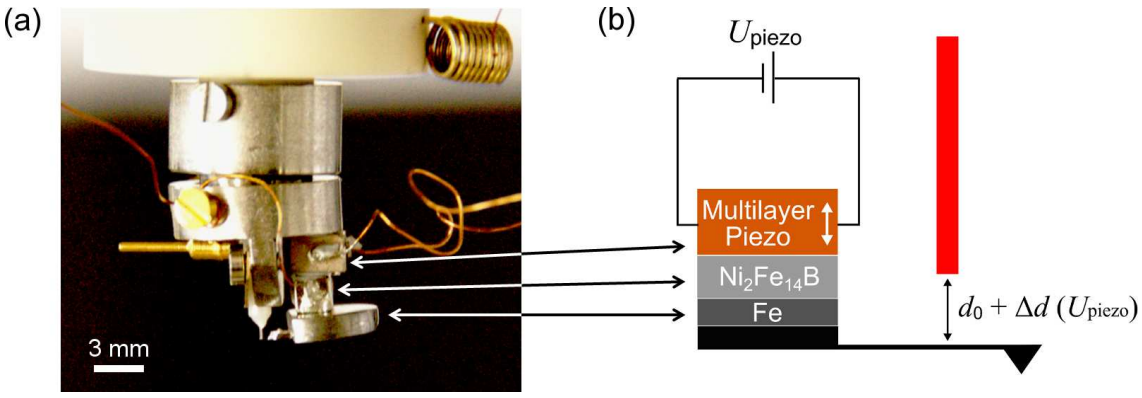

Figure 3.6: Cantilever and fiber end face form the main components of the microscope probe head. The lever is magnetically mounted on a stack including a miniature piezo actuator. A movably mounted ceramic ferrule contains the single-mode fiber to realize manual rough positioning of the fiber end face above the lever back side. Depending on an applied voltage U_{piezo}, the piezo actuator (Q-piezo) varies the distance between fiber end face and cantilever for fine positioning. This setup enables an adjustment of a sensitive distance d_{Q} before approaching the lever to sample surfaces.

Concerning a wavelength of $\lambda = 780$ nm, the factor s_λ is given by $s_{780\text{ nm}} = 62.07 \cdot 10^{-9}$ m. In order to match it with one of the periodic quadrature points d_{Q} to gain the maximum signal sensitivity during measurement, an improved scanning unit is designed for our setup.

3.3.2 AFM Head - The Scanning Unit

Without controlling the z-position of lever and fiber end face on the nanometer scale, the initial distance d_0 is determined arbitrarily. In contact, the scanning tube inside the inchworm drive can press the lever against a surface and a deflection results. Due to a voltage control over the tube, a distance variation Δd can be adjusted which matches with one of the periodic quadrature points d_{Q} to gain maximum signal sensitivity. A drawback of this approach is an undefined normal force F_z resulting from an initial and unknown deflection d_0 which also affects the longitudinal friction force F_x [46].
In order to avoid this drawback, a quadrature point d_{Q} has to be adjusted before the lever tip attaches the surface. An improved probe head is designed, realizing a pre-controlled distance variation $\Delta d(U_{\text{piezo}})$ depending on an operation voltage U_{piezo} (Fig. 3.6). A selectable DC voltage in a range of 0 - 100 V can be applied to a miniature multilayer piezo actuator[1] to fulfill the condition

$$d_0 + \Delta d(U_{\text{piezo}}) = d_{\text{Q}}. \tag{3.6}$$

The tip attaches the surface by using a feedback controlled piezo tube for an approach of the AFM probe head. Besides adhesive forces between tip and surface, an additional normal force F_z due to a normal deflection of the lever is eliminated. In contact, the feedback control can be adjusted to jump into the next quadrature point d_{Q}. The load

[1] Piezo Actuator PL033.30 \ Physik Instrumente (PI) GmbH & Co.KG

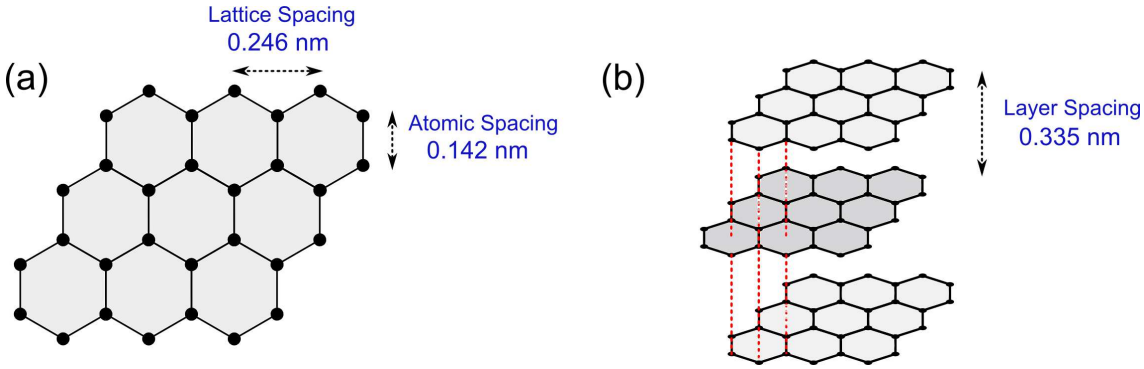

Figure 3.7: (a) Carbon atoms in graphite are covalently bonded and form a honeycomb structure. (b) The material consists of multi-layer structure with a layer spacing of 0.335 nm. Surface steps can arise due to a cleavage process of the topmost layers.

force, depending on the wavelength λ and normal spring constant k_z of the lever, increases for each jump m

$$F_z = m \cdot \frac{\lambda}{4} \cdot k_z. \tag{3.7}$$

In experiments these procedural steps can be used to adjust a required range of friction. In Fig. 3.6 the actuator is arranged in a stack, where the piezo bottom-side is glued to the base plate of the head. A $Ni_2Fe_{14}B$ cube is glued at the top-side which magnetically secures a soft iron plate (Fe). This construction attaches the cantilever to the head by avoiding appreciable lateral and longitudinal drift during measurements. In addition, the conductive parts of the stack are grounded to evade electrically charging of the lever with respect to the sample surface.
A ceramic ferrule for mounting the fiber is clipped to the head. This device provides a rough positioning of the end face to the cantilever in an appropriate scale of a few tens of microns.

3.3.3 Carbon Model System (HOPG) - Sample Material

Highly oriented pyrolytic graphite (HOPG) is a very popular and commonly used model sample material in scanning probe techniques [67]. The material consists of a multi-layer structure, where each graphite layer consists of sp^2 bonded carbon atoms which makes the surface chemically inert [67]. The layers are held together by van-der-Waals forces with a layer separation of 0.335 nm.
The material is built up of a great number of microcrystals, where each grain has its own lattice orientation. At the intersections between different grains, boundaries arise and disturb the crystal symmetry. The larger the grains, the higher the grade of graphite. The quality is described by the mosaic spread, where lower values describe a higher quality of the graphite [68]. For measurements within this thesis, high quality HOPG A-grade samples (mosaic spread: 0.4° - 0.8°), as well as lower quality HOPG B-grade samples

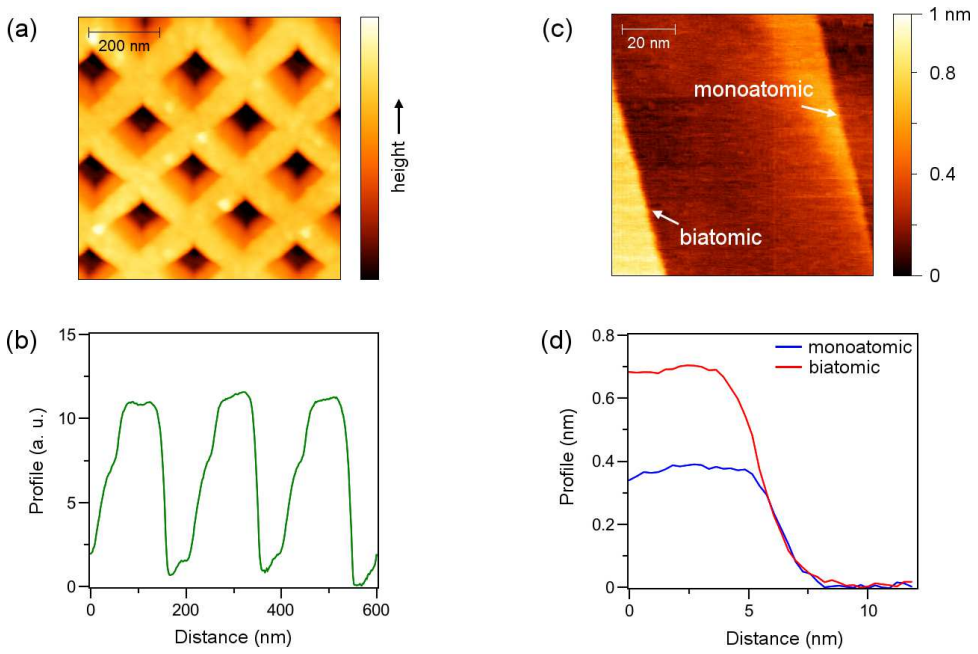

Figure 3.8: (a, b) A standard calibration grid with 200 nm x 200 nm periodicity is scanned to calibrate the scanner tube in x- and y-direction. (c, d) Surface steps on graphite with heights of a monoatomic and biatomic surface step are used for z-calibration.

(mosaic spread: 0.8° - 1.2°) are used.
The number of defects in the material is directly connected with the quality of the graphite. Smaller grains lead to surfaces with a higher density of surface defects. A detailed description is presented by *Pong et al.* [67] of various types of surface defects like cleavage steps, fibres and fibre clusters etc. on graphite.

3.3.4 Calibration of the Scanner Tube and Modulation Piezo

The scanner tube and modulation piezo have been calibrated for a correct reproduction of detected microscopy images with regard to the scanned x, y-area and z-topography as well as the modulation amplitude.
The displacement of the scanner tube depends on the applied voltage at the corresponding electrodes (Fig. 3.4). A standard calibration grid and atomic surface steps are used to find the correct scanning parameters in Fig. 3.8.
In order to determine the displacement of the modulation piezo in x-direction, a small area on a graphite sample is scanned in Fig. 3.9 (a). A voltage of 57 V is applied to the piezo and the area is scanned again in Fig. 3.9 (b). From the topography profile, a displacement of 58.6 nm can be recognized and consequently during measurements, a harmonic electrical signal with an amplitude of 1 V causes a harmonic piezo modulation of the sample with an amplitude of 1 nm.

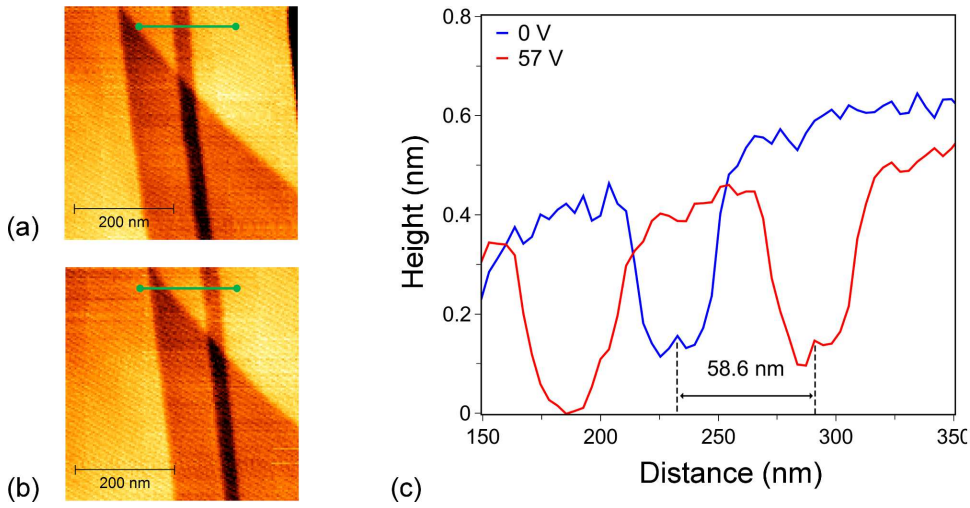

Figure 3.9: Calibration of the modulation piezo deflection depending on an applied voltage. A graphite surface is scanned showing structures. A voltage of 57 V is applied to the piezo and the surface is scanned again. A topography profile (green line) reveals a deflection of 58.6 nm resulting in a calibration factor of 1 nm/V.

3.3.5 Mechanical Properties of the PPP-CONTR Cantilever

A cantilever can be used as a sensor to detect forces on the nanometer scale. At its simplest, the cantilever consists of a lever beam and a conically converging, respectively a pyramidal tip. The tip is placed at one end of the lever and on the other end the beam is rigidly connected to the scanning unit. Forces acting on the tip elastically deform the lever in different ways depending on their direction. A deflection in one of the linearly independent x-, y- and z-directions can be characterized by simple spring constants k assuming the validity of Hooke's law [69]

$$F_x = -k_x \cdot \Delta x, \tag{3.8}$$
$$F_y = -k_y \cdot \Delta y, \tag{3.9}$$
$$F_z = -k_z \cdot \Delta z. \tag{3.10}$$

Δx, Δy and Δz describe the deflections in the corresponding directions. This causes the cantilever to perform a force F_x, F_y and F_y into the opposite direction, where the absolute value equals the exciting interaction force.
In Fig. 3.10 the different deflection modes are depicted. An interaction force acting in z-direction on the tip leads to a normal deflection of the cantilever. Friction forces along the lever in-plane x- and y-directions provoke a bending, respectively a torsion of the beam. In our setup the normal deflection is used to measure the topography of a sample surface, whereas the bending of the lever beam indicates the longitudinal friction interaction between tip and surface.
The cantilever spring constant k_x is derived from analytical expressions presented by *Sader* [69] for a quantitative analysis of friction forces. Starting with the spring constant in z-direction, k_z can be determined by the thickness t, width c, length L, as well as Young's modulus E of the used cantilever beam

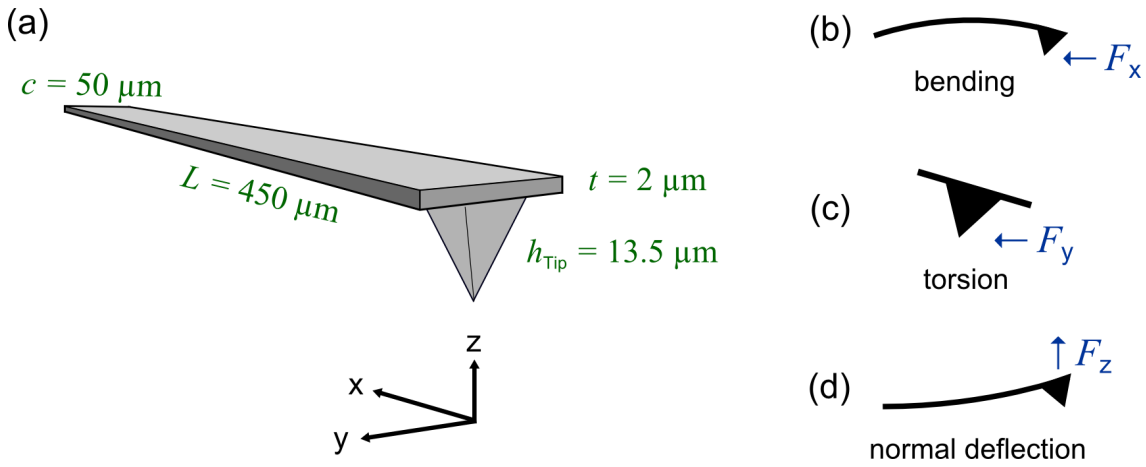

Figure 3.10: A cantilever is utilized as a force sensor on the nanometer scale. The dimensions and material of the lever mainly dominate its physical properties. (a) In our setup a typical silicon contact-mode cantilever PPP-CONTR is used for measurements. Young's modulus $E = 169$ GPa for the silicon (110) direction, $\Delta L = 10$ microns and a Poisson's ratio of $\nu = 0.22$ are considered for a calculation of its spring constants [70]. A longitudinal F_x (b), respectively a lateral friction force F_y (c) induces a bending or a torsion of the lever beam. Topographical interactions F_z (d) with the surface provoke a normal deflection of the lever.

$$k_z = \frac{E\, t^3\, c}{4(L - \Delta L)^3}. \tag{3.11}$$

In Fig. 3.10 the corresponding values for the lever PPP-CONTR[2] are specified. A constant $k_z = 0.2$ N/m results from Eq. 3.11 and matches with the value which is given by the manufacturer. The spring constants k_x and k_y behave proportionally to k_z by taking the lateral resistance R_x into account [69]

$$k_x = R_x \cdot k_z, \tag{3.12}$$
$$k_y = R_y \cdot k_z. \tag{3.13}$$

The lateral resistance R_x with respect to longitudinal forces for rectangular cantilevers is derived by two equations describing two different boundary conditions. In a first case, the tip is in rigid contact with the surface ($z = 0$) [69]

$$R_{x,\mathrm{contact}} = \frac{4}{3}\left(\frac{L - \Delta L}{h}\right)^2. \tag{3.14}$$

In a second case, this strict condition does not have to be fulfilled and the tip has the freedom to move in z-direction [69]

[2]PointProbe Plus Contact Mode Cantilever / NANOSENSORS$^{\mathrm{TM}}$

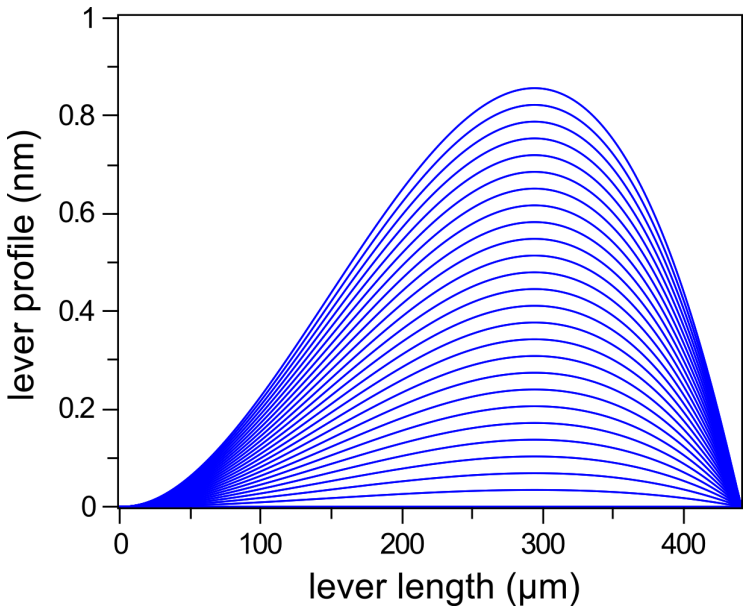

Figure 3.11: Side view of cantilever deflections due to longitudinal acting forces F_x at the tip in x-direction. The force range is $0 - 50$ nN with an increment of 2 nN. The maximum deflection is nearly arranged at the distance $3/4 \cdot L$ from the base of the lever.

$$R_{\mathrm{x,\ no\ contact}} = \frac{1}{3}\left(\frac{L - \Delta L}{h}\right)^2. \tag{3.15}$$

The longitudinal spring constants k_{x} for both conditions are

$$k_{\mathrm{x}} = \begin{cases} 70\ \mathrm{N/m}: \text{ no contact}, \\ 280\ \mathrm{N/m}: \text{ rigid contact}. \end{cases} \tag{3.16}$$

As a first approximation, it is assumed that the movement of the cantilever tip is between these two extremes during modulation. Therefore, the averaged value of Eq. 3.16 is chosen to specify the longitudinal force constant in our setup

$$k_x = 175\ \mathrm{N/m}. \tag{3.17}$$

Taking Poisson's ratio ν into account, the torsional mode of the lever is characterized by the lateral resistance R_{y} [69]

$$R_{\mathrm{y}} = \frac{2}{3\,(1+\nu)}\left(\frac{L - \Delta L}{h}\right)^2 \cdot \left(1 - \frac{\tanh\left(\frac{L-\Delta L}{c}\sqrt{6\,(1-\nu)}\right)}{\sqrt{6\,(1-\nu)}}\frac{c}{L - \Delta L}\right)^{-1}. \tag{3.18}$$

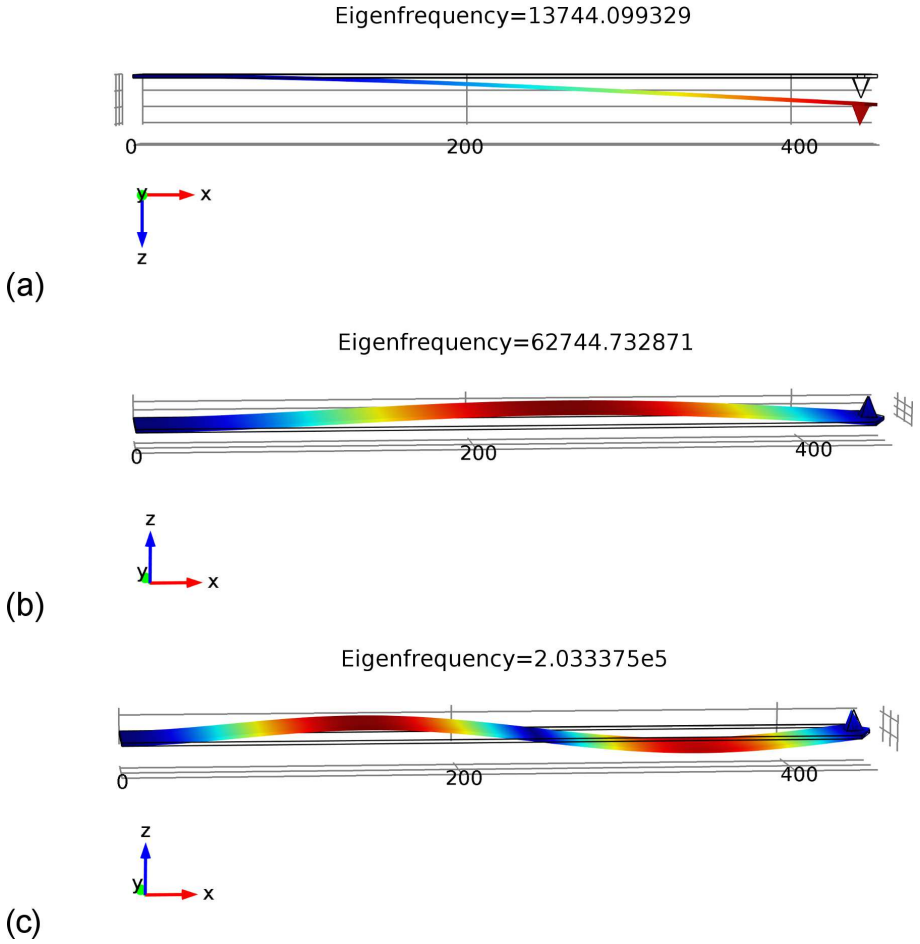

Figure 3.12: Finite-element-method (FEM) simulations for different eigenmodes and corresponding resonance frequencies f_{res} of the PPP-CONTR cantilever. (a) For free vibrations of the cantilever beam $f_0 = 13.7$ kHz results. (b, c) A longitudinal eigenfrequency of $f_{\mathrm{res}} = 62.7$ kHz (1st flexural mode (bending mode)), respectively $f_{\mathrm{res}} = 203.3$ kHz (2nd flexural mode result) results for a tip in contact with the surface.

and the lateral spring constant amounts to

$$k_{\mathrm{y}} = 125 \text{ N/m}. \tag{3.19}$$

In order to receive an impression of how the lever is bent due to a longitudinal acting force at the tip, a finite-element-method (FEM) is used to calculate the bending deflection of the lever in Fig. 3.11. The tip is in rigid contact with the surface and the side view exhibits that the maximum displacement is reached at nearly $3/4 \cdot L$ from the base of the lever.
In the setup the fiber is placed around this position above the cantilever back side to gain the maximum signal-to-noise ratio for dynamic bending oscillations. Therefore, one has to note that the detected lever deflection depends on the longitudinal position of the fiber with respect to the cantilever beam.

3.3.6 Eigenfrequencies of Cantilever Modes

A dynamic excitation of the cantilever is directly connected with the resonance characteristic of the lever beam. Depending on the interaction between tip and surface, it can be assumed that the cantilever subjects to oscillations at its resonance f_{res}. The knowledge of resonance frequencies for different oscillation modes is essential for an analysis of measured data. Arising frequency components in the dynamic signal, like higher harmonics or beat frequency, can be allocated. In Fig. 3.12 resonances of the lever are derived from finite-element simulations. The bending resonance amounts to $f_{\mathrm{res,\ bending}} = 62.7$ kHz, whereas the normal resonance $f_{\mathrm{res,\ normal}} = 13.7$ kHz is significantly lower. A comparison of both resonance frequencies results in a ratio of

$$f_{\mathrm{res,\ bending}}/f_0 = 4.6. \tag{3.20}$$

This ratio matches distinctly well with the result given by *Krischker* [61] of approximately 4.4 which is derived from the Euler-Bernoulli beam equation.
In the following experiments, the bending resonance frequency $f_{\mathrm{res,\ bending}}$ is primarily discussed and simply referred to as f_{res}. The tip is in contact with the surface during measurements and friction affects the bending resonance. Resulting from damping and further interactions forces, frequency shifts of the resonance frequency can occur. Intrinsic losses of the beam oscillation can be neglected in this context due to its comparatively high quality under UHV conditions [61].

3.4 Signal Analysis - Lock-In Detection Techniques

The detected interferometer signal in dynamic friction force microscopy consists of two voltage contributions (Fig. 3.13). A comparatively slow scanning movement causes a direct current (DC) voltage. In addition, the modulation of the sample causes dynamic bending oscillations of the lever which induces an alternating current (AC) voltage. Therefore, the interferometer signal U_{sig} comprises of both voltage components

$$U_{\mathrm{sig}} = U_{\mathrm{DC}} + U_{\mathrm{AC}}. \tag{3.21}$$

During measurements the tube realizes scanning movements in the x, y-plane. A fluctuating surface topography leads to normal deflections in z-direction of the lever. Due to the slow movement the detected interferometer signal is displayed as DC voltage. The voltage is applied to a digital feedback control[3] which controls the displacement of the tube in z-direction [71, 72]. Depending on the chosen feedback parameters the lever is consistently deflected and the interferometer signal matches with one of the quadrature points d_{Q}. Smallest deviations during scanning are revised by the feedback control which provides measurements with constant load ($F_z = \mathrm{const.}$). The feedback voltage contains topographical information of the sample surface and is monitored by a computer.
The second AC contribution is caused by a modulation movement of the sample surface.

[3] Signal Ranger MK2 DSP board/ Soft dB

A reference source applies a harmonic signal to the modulation piezo, where the frequency is in a range of several kilohertz. A friction induced bending oscillation of the cantilever beam is detected as AC voltage and the dynamic amplitude serves as an indicator for the acting friction force between tip and surface. A lock-in amplifier[4] extracts the oscillation amplitude during modulation [12]. Regarding a modulation frequency $f_{\mathrm{mod}} = \omega_{\mathrm{mod}}/(2\pi)$ of the reference source, the lock-in signal is given by [73]

$$U_{\mathrm{AC}}(\omega) \propto \frac{1}{\Delta T} \int_{t-\Delta T}^{t} U_{\mathrm{sig}}(\upsilon)\ \sin(\omega_{\mathrm{mod}}\,\upsilon + \varphi_{\mathrm{mod}})\ d\upsilon. \tag{3.22}$$

The amplifier supports an auto-controlling of the phase φ_{mod} and accordingly this method supplies a signal which is proportional to the dynamic amplitude component with reference to the modulation frequency f_{mod}. A computer simultaneously monitors the lock-in signal and the topography.
In order to gain direct access to the whole frequency spectrum of cantilever oscillations, the setup is extended by a fast data acquisition card (DAC) which provides a real- time monitoring of the dynamic component U_{AC} [74].
The lock-in method is utilized as a band-pass filter in the frequency domain, extracting the amplitude of one frequency component in an idealized case. This frequency component matches the modulation frequency f_{mod} and consequently the cantilever oscillation amplitude $A(f_{\mathrm{mod}})$ can be detected. The signal sensitivity s of the lock-in can be adjusted from micro-volts to several milli-volts and the integration time ΔT amounts to a range of milli-seconds. Hitting the noise floor of the interferometer signal can be compensated by an increased sensitivity and integration time of the lock-in amplifier.
Due to this sensitive and fast oscillation analysis, these properties make the lock-in detection a valuable tool for the imaging of frictional properties on the nanometer scale, simultaneously to the detection of the topography. Its limitation to extract just one frequency component has resulted in the following developments.

3.4.1 Cantilever Off-resonance Modulation Technique

Developed by *Göddenhenrich et al.* [12], the lock-in technique is used to measure local friction loops, where the frequency is chosen well below the resonance of the cantilever $f_{\mathrm{mod}} < f_{\mathrm{res}}$. Later on, a similar approach was presented by *Yamanaka et al.* [75] for torsional excitation. They found that for small modulation amplitudes A_{mod} the tip sticks to the surface, referred to as static friction regime. The tip overcomes the sticking regime and starts to slide across the surface for larger modulation amplitudes. Consequently, one forth and back modulation cycle exhibits a local friction loop and the enclosed area of this loop represents the dissipated energy. An additional scanning movement reveals frictional properties of the sample surface, but a constant modulation amplitude impedes a quantitative analysis of friction forces on surfaces.
Furthermore, *Colchero et al.* [73] and *Krotil et al.* [58] presented an enhanced interpretation of friction loops by applying this technique.
Haugstad [76] used the non-linear characteristic of the stick and slip interactions. He found

[4]SR 830 DSP Lock-in Amplifier / Stanford Research Systems

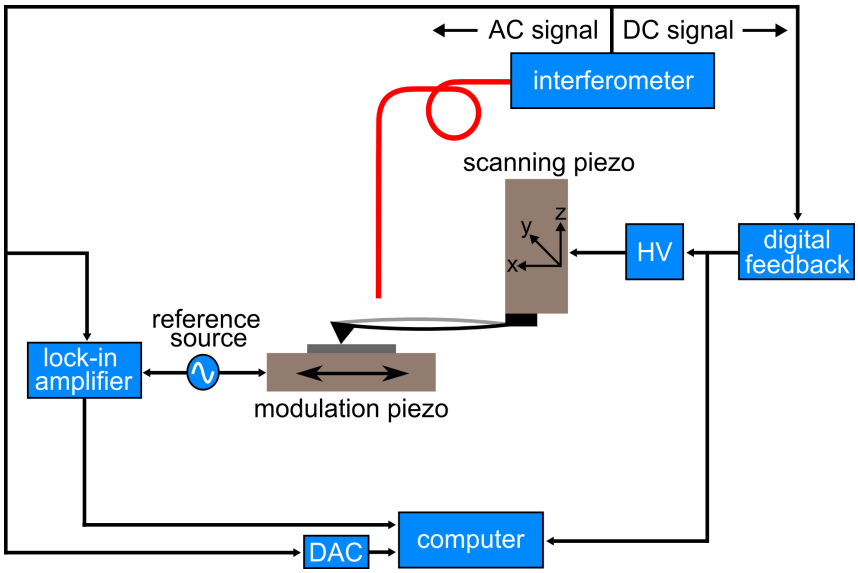

Figure 3.13: A reference source generates the modulation signal f_{mod} which is applied to the modulation piezo. The contact between tip and sample induces dynamic bending oscillations which are detected by the laser interferometer. The topography leads to static defection signal which is controlled by a feedback. A lock-in amplifier extracts the dynamic signal with respect to the reference source. In addition, the signal can be monitored by a data acquisition card.

that the ratio between the third and the first harmonic component due to non-linear tip-sample interactions is a sensitive measure to characterize static-to-sliding transitions on polymer films.

3.4.2 Cantilever Resonance Modulation Technique

A further development of the lock-in technique is the resonance excitation $f_{\mathrm{mod}} = f_{\mathrm{res}}$ of the cantilever vibration mode. *Spychalski-Merle et al.* [59] presented a spectroscopy mode which performs local resonance curves on a sample surface, where the quality factor Q reveals friction losses of the cantilever oscillation during modulation. Different friction contrast mechanisms were investigated during scanning surfaces. It is found that for small amplitudes the tip sticks to the surface and the image contrast is dominated by shifts of the resonance frequency f_{res} due to the presence of surface gradients. With increasing modulation amplitude, stick-slip interactions arise and the tip starts to slide across the surface. Here, the primary contrast mechanism is allocated to frictional damping during the slip phases.
Reinstädtler et al. [60] focused on the shape of resonance curves depending on load and modulation amplitude. The shape of curves is Lorentzian for low amplitudes indicating a linear oscillator. With increasing amplitude the curves flatten out which is explained by the transition from linear stick interactions to non-linear stick-slip events of the tip.
Kawagishi et al. [77] studied different contrast mechanisms at the resonance for different sample systems like self-assembled monolayer domains, silicon and silicon dioxide, graphite and mica by using the lock-in technique.

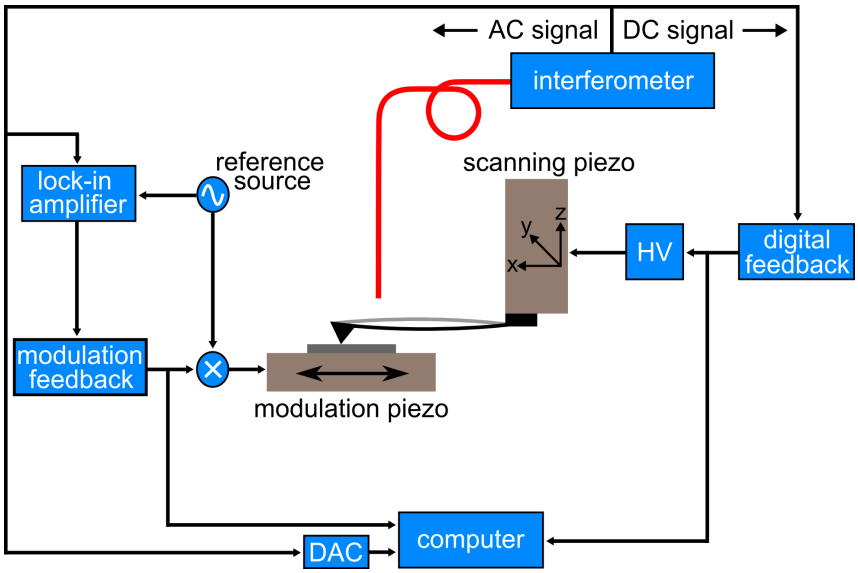

Figure 3.14: A fiber interferometer is used to detect the dynamic cantilever bending (AC) caused by a modulation of the sample and the static cantilever deflection (DC) due to the scanner movement. The signal from the digital feedback controller corresponds with the topography. For friction imaging a second modulation feedback controls the modulation amplitude by keeping the cantilever resonance amplitude constant at the set-point near the transition from non-linear to linear oscillation. (*Figure is published in Applied Physics Letters, 104 (2014) 113105*)

3.4.3 Cantilever Fractional Resonance Excitation Technique

Within this thesis, the lock-in technique is used for the detection of resonant cantilever response caused by static-to-sliding transitions between tip and surface. Stick-slip interactions during off-resonant modulation excitations $f_{\mathrm{mod}} < f_{\mathrm{res}}$ of the lever bending mode are responsible for the presence of bending resonance oscillations f_{res}. The experimental setup and corresponding measurements performed within this thesis are published in *F. Mertens et al. Applied Physics Letters, 104 (2014) 113105.*
The lock-in amplifier provides an extraction of higher harmonics in the signal with respect to the exciting reference and modulation frequency f_{mod}. An off-resonant modulation frequency which matches with an integer fraction of the resonance $f_{\mathrm{mod}} = f_{\mathrm{res}}/3$, excites dynamic oscillations at resonance f_{res}. In Fig. 3.14 the lock-in technique extracts the resonant cantilever response as third harmonic of the modulation frequency.
Furthermore, the appearance of a resonance amplitude $A(f_{\mathrm{res}})$ depends on the modulation amplitude A_{mod} and is directly related to the transition from static-to-sliding friction. A second modulation feedback controls the modulation amplitude by keeping the cantilever resonance amplitude constant at the set-point near the transition from non-linear to linear oscillation for friction imaging. Moreover, this technique is less sensitive to surface gradients which isolate friction imaging from cross-talk of the topography.
In order to gain a direct access to the cantilever real-time oscillation, the lock-in technique is not applicable. Therefore, the setup is extended by a fast data acquisition card which detects the signal with high time resolution.

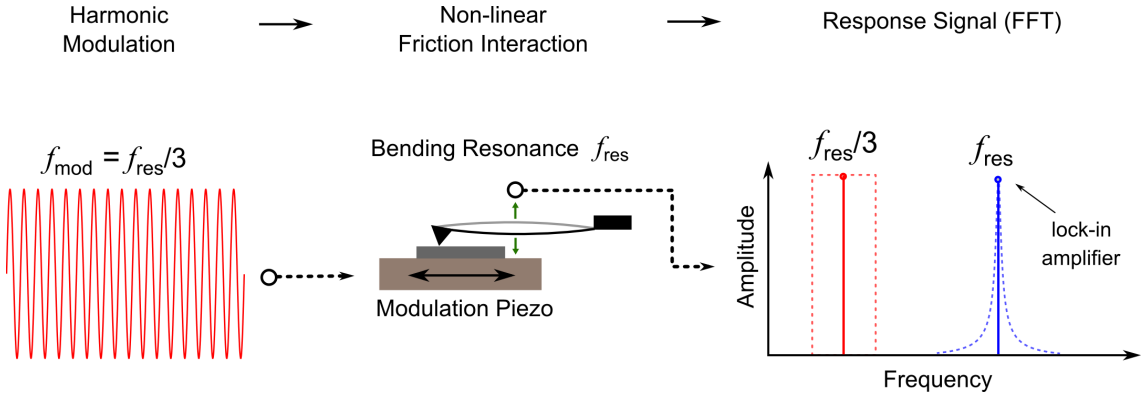

Figure 3.15: The single-frequency and off-resonant $f_{\text{res}}/3$ modulation signal (red) is applied to the modulation piezo. The non-linear interaction between tip and sample excites dynamic bending oscillation of the cantilever bending mode. The electrical signal of the interferometer is detected by a data acquisition card (DAC). The fast Fourier transformation of the time signal exhibits all frequency components in the response oscillation. In this illustration, a resonance oscillation f_{res} component is extracted by a lock-in as third harmonic of the modulation frequency which is caused by the non-linear interaction between tip and sample (blue).

3.5 Signal Analysis - Data Acquisition Card

The dynamic bending oscillation of the cantilever beam is detected by a laser interferometer. The sample rate of the detection technique has to be fast enough for a processing and digital sampling of the analogous electrical signal. The lower limit for the sample rate f_{rate} to detect a frequency in the signal f_{signal} is given by the Nyquist rate

$$f_{\text{rate}} > 2 \cdot f_{\text{signal}} \tag{3.23}$$

Including the bending resonance frequency of around $f_{\text{res}} = 60$ kHz, U_{AC} is additionally applied to a fast data acquisition card[5]. The acquisition card provides a rate of 10^7 samples per second. Thus, one bending resonance period can be sampled with 166 samples which allows a full reconstruction of the signal including frequency f_{res} and amplitude $A(f_{\text{res}})$.
In contrast to the lock-in technique, a fast Fourier transformation (FFT) can extract all frequency components from the detected signal simultaneously. In our case a frequency bandwidth between 10 kHz - 100 kHz is considered to be appropriate.
Concerning one acquisition cycle, the fast Fourier transformation calculates the components of a two-sided spectrum for the detected samples [78]

$$F(t) = \sum_{k=-\infty}^{\infty} \underline{c}_k \, e^{(i\,k\,\omega\,t)}. \tag{3.24}$$

The complex coefficients $\underline{c}_k$ $(k > 0)$ provide half the amplitudes A_k concerning each frequency component in the real-time signal

$$A_k = 2 \cdot |\underline{c}_k| \,. \tag{3.25}$$

[5] 12-Bit, Ultra High-Speed Multifunction Board *PCI-DAS4020/12* / Measurement Computing

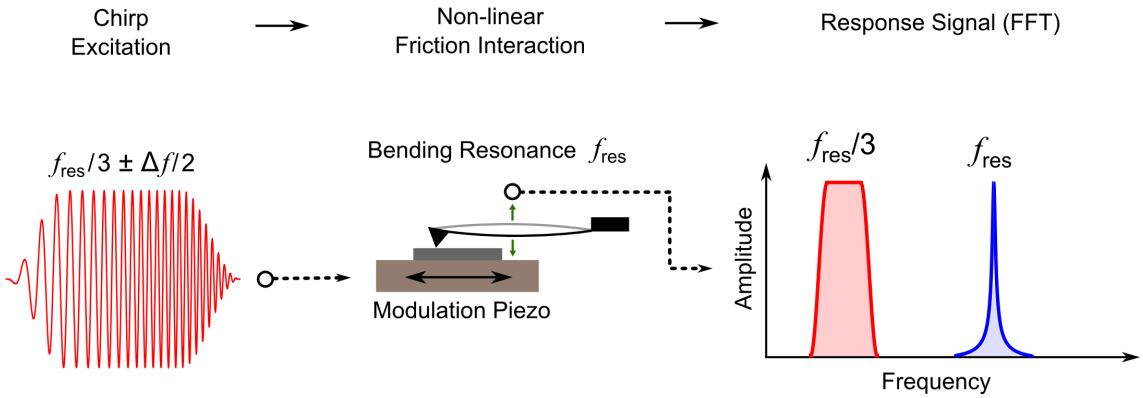

Figure 3.16: A modified chirp pulse is applied to the modulation piezo to excite dynamic bending oscillations (red). The pulse is multiplied by a Tukey window to avoid abrupt signal variations during measurements and contains a frequency range around $f_{res}/3$. The response oscillation of the bending mode is analyzed by a fast Fourier transformation. The signal processing contains all relevant resonance parameters at f_{res} like frictional damping and frequency shifts of the non-linear bending oscillation (blue).

The frequency separation Δf between adjacent frequency components has to be sufficiently small for an appropriate resolution of distributions in the frequency domain like resonance curves. Depending on sample rate f_{rate} and number of samples N, the separation Δf is determined by

$$\Delta f = \frac{f_{rate}}{N}. \tag{3.26}$$

A resolution of $\Delta f = 50$ Hz is considered to be adequate for the detection of resonant cantilever modes in the relevant frequency ranges. The resulting rate of $5 \cdot 10^6$ samples per second and number of samples $N = 10^5$ furthermore support an adequate Fourier processing time during measurements.
In order to avoid a broadening of components A_k in the frequency domain due to the leakage effect, the time signal is multiplied by a Hamming window function before the Fourier analysis is executed [79].

3.6 Band Excitation (BE) Technique

The response of an oscillatory system is essentially governed by damping. During scanning measurements, a single-frequency excitation is not applicable to detect energy dissipation and resonance frequencies. An exhibition of the full resonance characteristics needs a series of response oscillations concerning a shift of the single-frequency excitation. This procedure has the drawback of a long measurement time concerning data acquisition and processing.
In order to overcome this disadvantage, *Jesse et al.* [44] introduced the band excitation (BE) method to detect resonance curves and phase shifts of cantilevers. Basically, an excitation pulse is used to stimulate the oscillation of the lever. The pulse in Fig. 3.16 provides a frequency band around a mid-frequency f_0 with a tunable bandwidth Δf and

is generated by an arbitrary waveform generator[6]. A fast Fourier transformation of the real-time response oscillation contains the basic resonance properties of the system.
An adaption of this technique concerning the non-linear $f_0 = f_{\mathrm{res}}/3$ mode is performed in our setup (Fig. 3.16). *Kareem et al.* [45] discussed the application of a linear chirp function $A(t)$ with an offset in the frequency domain to gain an excitation pulse covering an adequate frequency band

$$A(t) = A \cdot \sin(\alpha(t + t_{\mathrm{off}})^2). \tag{3.27}$$

In order to provide a frequency Δf range of the pulse around a mid-frequency f_0, an upper f_{up} and a lower f_{low} cutoff frequency have to be assigned

$$\Delta f = f_{\mathrm{up}} - f_{\mathrm{low}}. \tag{3.28}$$

The low cutoff frequency f_{low} is determined by the parameter α in units rad s^{-2} and t_{off}

$$f_{\mathrm{low}} = \frac{\alpha\, t_{\mathrm{off}}}{\pi}, \tag{3.29}$$

The duration of the pulse t_{dur} determines the high cutoff frequency f_{up}

$$f_{\mathrm{up}} = \frac{\alpha\,(t_{\mathrm{dur}} + t_{\mathrm{off}})}{\pi}. \tag{3.30}$$

The chirp function $A(t)$ is additionally multiplied by a window function [45] to avoid abrupt signal variations during measurements. This modification by a Tukey window function in Fig. 3.16 leads to a pulse with soft transitions between minimal and maximal signal amplitude to evade artificial peaks in the response [45].
During measurements the chirp pulse continuously excites the sample surface. In combination with a scanning movement of the cantilever tip, the signal processing of the dynamic lever response contains characteristics of the resonance for each image pixel with regard to the tip-sample interaction. The drawback of a long processing time due to a calculation of each fast Fourier transformation evokes a slow scanning speed and images with lower resolution.

3.7 Conclusion

Dynamic friction measurements are performed in an ultra-high vacuum (UHV) chamber, which is used as experimental environment. The microscope is placed on an eddy current damping system and a fiber interferometer is used for the detection of cantilever deflections.

[6] Arbitrary Waveform Generator 33500B / Agilent Technologies

A sample modulation in lateral direction is the basic principle of dynamic friction force microscopy. Frictional interactions between tip and surface along the long-axis of the cantilever excite dynamic bending oscillations of the lever beam. Different excitation techniques are possible with respect to the resonance of the bending mode f_{res}. Off-resonant, as well as resonant modulation techniques lead to different contrast mechanisms in friction images. A fractional excitation approach is developed within this thesis which can map local friction. An off-resonant modulation frequency, which matches with an integer fraction of the resonance frequency $f_{\mathrm{mod}} = f_{\mathrm{res}}/3$, induces dynamic oscillations at resonance f_{res}.
A lock-in detection scheme extracts the resonant cantilever response as third harmonic of the modulation frequency. An additional feedback loop controls the resonant response, which corresponds with the transition from static-to-sliding friction of the tip-sample interaction. A band excitation (BE) method is adapted to the system for a more detailed investigation of friction interactions. The signal processing contains all relevant resonance parameters at f_{res} like frictional damping and frequency shifts.
Furthermore, an analytical approach, as well as finite-element-method (FEM) simulations are used to determine the spring constants and eigenfrequencies of different cantilever modes of the used PPP-CONTR cantilever.

4 Fractional Resonance Excitation and Stick-Slip Interactions

The stick-slip mechanism is a frictional phenomenon which is responsible for a wide variety of movement and oscillation states in nature. On length scales of several hundreds or even thousands of kilometers, the arising of earthquakes can be interpreted as stick-slip motion [80]. The slip part represents the quake and the stick part relates to the seismic resting period [80]. The weal squeal of railways and the acoustic violin play are further examples of stick-slip interactions [81, 35]. Scaling down to microscopic dimensions, elastic colloidal crystals can be brought into vibrational resonance which is also allocated to the stick-slip mechanism [82]. Atomic stick-slip occurs even on the nanometer scale if a cantilever tip is forced across the potential of an atomic lattice [8].
In particular, the transition from static-to-sliding friction has been the focus of several studies by friction force microscopy recently [50, 51, 49]. This transition is closely connected to stick-slip processes and can influence the sequential order of movement states. An increased static friction force due to frictional aging during the stick part can occur and delays the stick-to-slip jump. The relative orientation of atomic lattices can furthermore affect frictional interactions and consequently frictional anisotropy can influence atomic stick-slip [55].
The discontinuous stick-slip mechanism is also responsible for non-linear lever oscillations in dynamic friction force microscopy. Off-resonant, as well as resonant excitations at the tip-sample contact can induce non-linear cantilever vibrations [12, 59]. Within this chapter, a modulation technique is developed which displays friction at the stick-to-slip transition and maps local friction forces with high sensitivity.
Some paragraphs and figures of this chapter have already been published in F. Mertens et al. Applied Physics Letters, 104 (2014) 113105.

4.1 Non-linear Cantilever Response - Experiment and Simulation

The modulation of a surface in dynamic friction force microscopy causes oscillations of the cantilever beam (Fig. 4.1) which reflect tribological properties of the sample.
Here, experimental data are presented which illustrate the dynamic oscillation response with regard to the excitation frequency f_{mod} under UHV conditions. The detection of non-linear cantilever oscillations suggests that the interaction at the tip-sample contact consists of stick and slip parts.
A phenomenological model is developed to simulate the non-linear movement states and to give an insight into the sequential structure of friction induced non-linear cantilever oscillations.

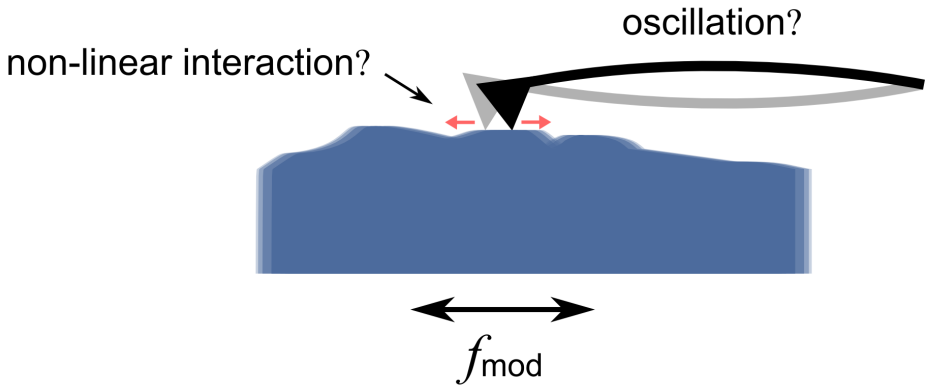

Figure 4.1: The modulation of a sample surface in longitudinal direction induces bending oscillations of the cantilever beam. However, it is not clear how a resonant oscillation depends on an off-resonant modulation frequency f_{mod} and amplitude A_{mod} , as well as the non-linear friction interaction between tip and surface in dynamic friction force microscopy.

4.1.1 Experiment: Non-linear Amplitude Response

The longitudinal modulation technique in Fig. 3.1 (b) is conducted to detect cantilever bending oscillations as a response to off-resonant frequency excitations. The reference source in Fig. 3.13 generates a harmonic voltage signal and the data acquisition card (DAC) is used to monitor the interferometer signal.
A harmonic vibrating graphite surface (HOPG) excites the longitudinal cantilever mode with a modulation amplitude of several nanometers $A_{\mathrm{mod}} = 7$ nm. Non-linear friction interactions at the tip-sample contact induce dynamic vibrations of the cantilever beam. Below the bending resonance, an off-resonant frequency range from 10 kHz to 55 kHz is examined. At a given modulation frequency of the reference source, the second to fifth harmonic component of f_{mod} is extracted from the fast Fourier transformation of the averaged cantilever oscillation in Fig. 4.2 (a). Furthermore, the cantilever amplitude response around the resonance frequency $f_{\mathrm{res}} \approx 60$ kHz is plotted as first harmonic of the modulation frequency (Fig. 4.2 (b)) by applying a much lower modulation amplitude $A_{\mathrm{mod}} = 1$ nm to preserve the cantilever tip.
The signal amplitude in Fig. 4.2 (a) is increased and above the noise floor at certain frequencies and for different harmonics. In order to gain insight into the off-resonance excitation mechanism, it can be recognized that the increased signal i.) - iv.) is exclusively excited at integer fractions of the resonance frequency $f_{\mathrm{mod}} = f_{\mathrm{res}}/n$ with $n = 1, ..., 5$. Evidently, non-linear interactions between tip and surface lead to different movement states, where the oscillation is partially fulfilled in resonance. The off-resonant excitation at $f_{\mathrm{mod}} = f_{\mathrm{res}}/3$ induces a significant resonance oscillation and obviously operates at its best, because of the highest signal-to-noise ratio.
Moreover, an increased signal can be observed at two further modulation frequencies v.) and vi.). Here, the fourth and fifth harmonic component of the 2nd flexural mode of the lever beam are excited. A resonant frequency of $f_{\mathrm{res}} \approx 190$ kHz can be determined which nearly matches the predicted frequency from simulations.
In order to receive a further understanding of the resonant lever response, the data acqui-

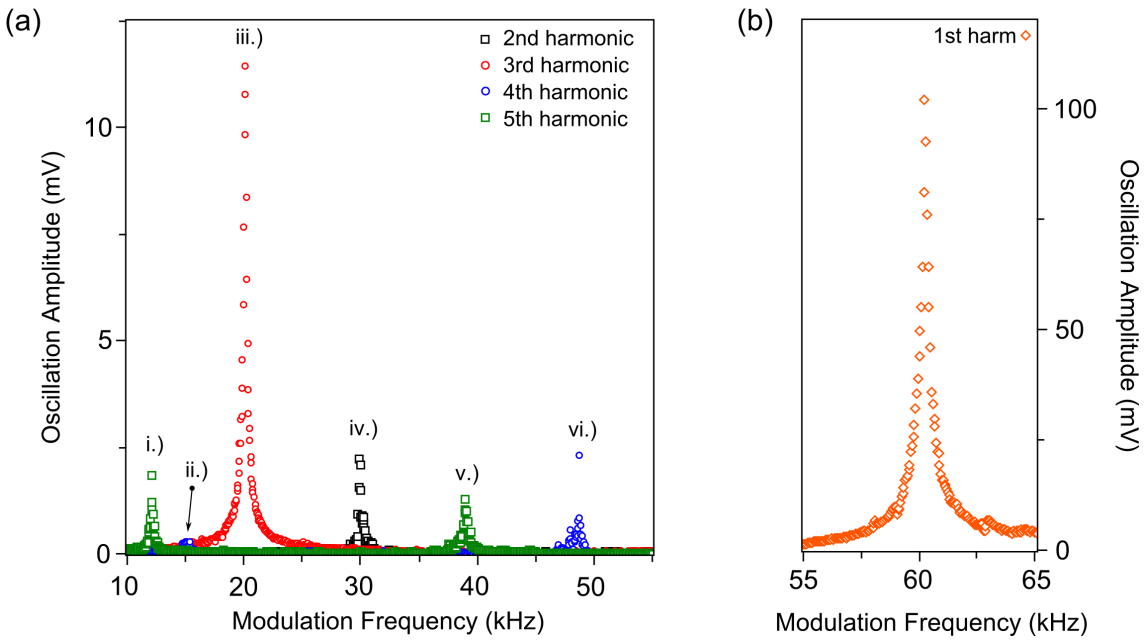

Figure 4.2: (a) The amplitude response for the second to fifth harmonic caused by a harmonic off-resonance modulation of the sample surface in longitudinal lever direction with a fixed amplitude of $A_{\mathrm{mod}} = 7\,\mathrm{nm}$. At integer fractions of the bending resonance i.) - iv.) the signal of the corresponding harmonics is increased, indicating resonance oscillations of the bending mode. Furthermore, the fourth and fifth harmonic reveal an increased signal at integer fractions of the 2nd flexural mode resonance v.) and vi.). Obviously, the best signal to noise ratio is achieved for $f_{\mathrm{mod}} = f_{\mathrm{res}}/3$. (b) Amplitude response of the cantilever bending mode around its resonance frequency of $f_{\mathrm{res}} \approx 60$ kHz.

sition card is used to detect the averaged real-time bending oscillation over a defined time period at a modulation frequency of $f_{\mathrm{mod}} = f_{\mathrm{res}}/3$. At similar load forces of a few tens of nanonewtons and for a fixed modulation amplitude $A_{\mathrm{mod}} = 1.4$ nm, the oscillation on graphite and silicon is monitored. The optimal excitation frequencies are separately used for both sample surfaces.

The real-time oscillations are depicted on the left part of Fig. 4.3 and the corresponding fast Fourier transformations from 10 kHz to 80 kHz are depicted on the right. The real-time oscillations show a non-linearity consisting of different oscillation components for both samples. The Fourier transformations exhibit that the non-linear oscillations consist of a modulation component $f_{\mathrm{mod}} = f_{\mathrm{res}}/3$, as well as a resonant lever component f_{res}. Consequently, it can be concluded, that the cantilever bending mode oscillates partially in resonance and also vibrates at the modulation frequency during modulation.

The non-linearity of the oscillations can be determined for a further discussion of this feature. At a given modulation amplitude, the ratio between third harmonic amplitude $A(f_{\mathrm{res}})$ and modulation amplitude $A(f_{\mathrm{res}}/3)$ indicates a degree of non-linearity $\mathcal{N}$ for the contact

$$\mathcal{N} = \frac{A(f_{\mathrm{res}})}{A(f_{\mathrm{res}}/3)}. \tag{4.1}$$

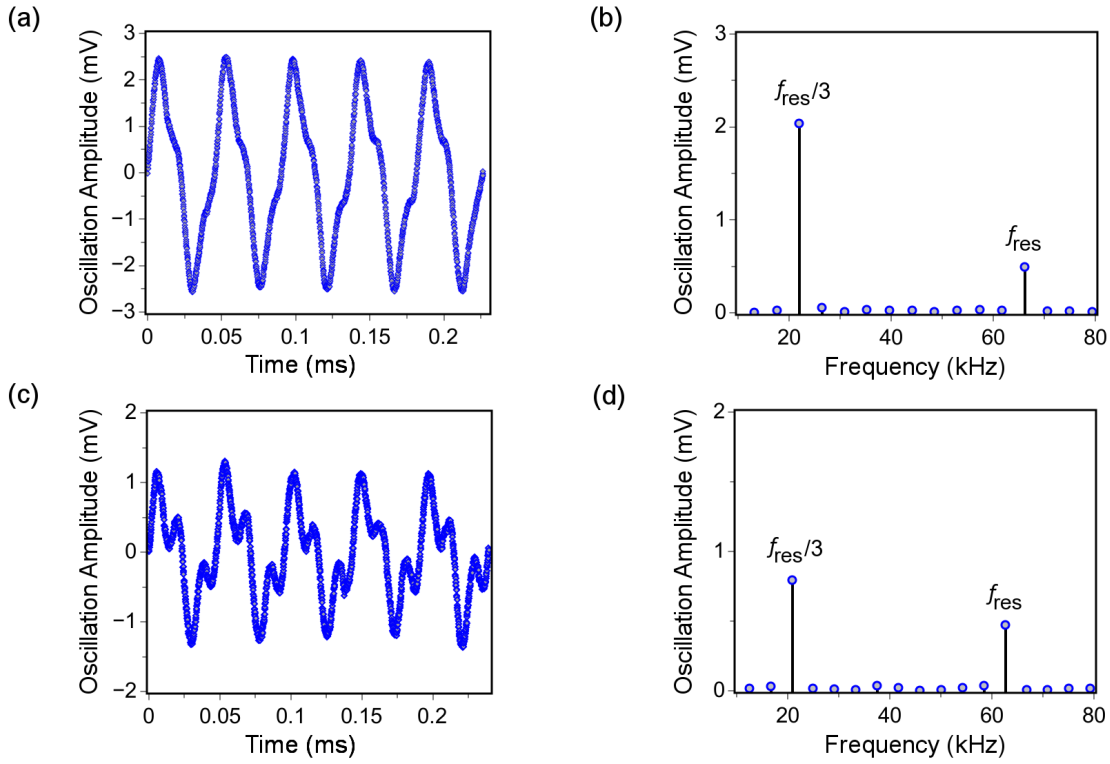

Figure 4.3: (a, c) Real-time acquisition of the lever bending oscillation at a fixed modulation frequency of $f_{\mathrm{mod}} = f_{\mathrm{res}}/3$ on silicon (top) and highly oriented pyrolitic graphite (bottom). (b, d) The corresponding fast Fourier transformations of the bending oscillations. A resonance frequency f_{res} in the response appears besides a modulation frequency $f_{\mathrm{mod}} = f_{\mathrm{res}}/3$ component. The third harmonic component is caused by a non-linear friction interaction at the contact between tip and sample.

The Fourier transformations exhibit that the non-linearity of the oscillation on graphite is increased compared to the oscillation on silicon

$$\mathcal{N}_{\mathrm{HOPG}} > \mathcal{N}_{\mathrm{silicon}}. \tag{4.2}$$

In summary, taking into account that all experimental parameters are similar, the oscillation is mainly governed by the friction interaction between tip and surface.
The modulation frequency f_{mod} between cantilever tip and sample surface is responsible for the movement state of the lever bending mode. At an off-resonant excitation $f_{\mathrm{mod}} = f_{\mathrm{res}}/3$, a distinct non-linear and dynamic bending oscillation of the lever is excited. The friction interaction triggers the non-linearity of the oscillation and the distribution of modulation and resonance parts in the real-time oscillation.

4.1.2 Simulation: Phenomenological Spring-Mass System

In order to emulate the movement states of the experimental non-linear amplitude response, a phenomenological model represents the experimental setup. Motivated by a

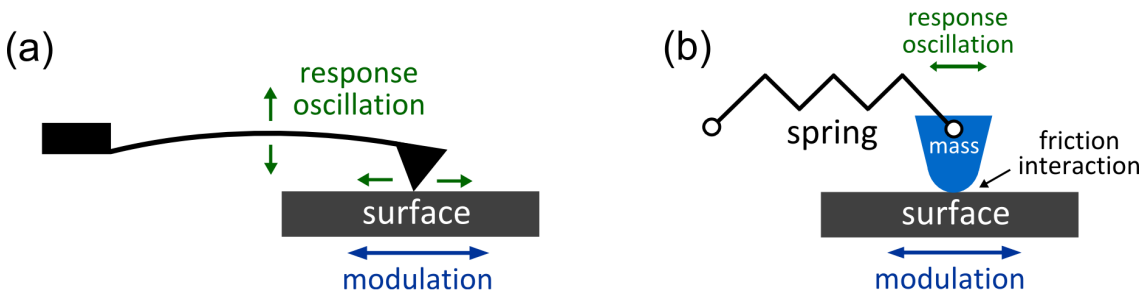

Figure 4.4: (a) Schematic picture of the cantilever tip in contact with the sample surface. The longitudinal friction force leads to lever bending oscillations caused by a modulation of the sample surface. (b) A phenomenological model is used to describe the cantilever response oscillation. The lever is represented by a spring which is coupled to a mass in contact with the modulation surface.

friction-driven macroscopic system [35], the bending mode of the cantilever is represented by a spring-mass system. Dynamic oscillations of the lever can be described by the equation of motion presented in Chap. 2. A modification of this equation describes the spring-mass system and can be used to calculate the temporal development of oscillations. The mass is placed on top of a vibrating surface oscillating at the modulation frequency f_{mod}. The resonance frequency f_{res} of the system is determined by the spring constant k_{spring} and mass m of the system (Fig. 4.4)

$$f_{\mathrm{res}} = \frac{1}{2\pi} \cdot \sqrt{\frac{k_{\mathrm{spring}}}{m}}. \tag{4.3}$$

The resonance frequency of the spring-mass system $f_{\mathrm{res}} = 60$ kHz is preassigned to match simulated and experimental oscillations of the bending mode. The spring constant is chosen as the averaged spring constant $k = 175$ N/m in the experiments and the mass of the system is consequently given by

$$m = \frac{k}{4\pi^2 \cdot f_{\mathrm{res}}^2} = 1.23 \cdot 10^{-9} \text{ kg}. \tag{4.4}$$

The harmonic modulation of the surface is fulfilled with the modulation frequency f_{mod} and amplitude A_{mod} in longitudinal direction

$$x_{\mathrm{surface}}(t) = A_{\mathrm{mod}} \cdot \sin(2\pi \cdot f_{\mathrm{mod}} \cdot t). \tag{4.5}$$

As described in Sec. 2.3.1 the interaction between mass and surface is given by conservative and dissipative forces. Due to the comparably high spring constant, a contribution of the atomic surface potential $F(x) = -\partial V(x)/\partial x$ is neglected and the total force accelerates the mass m

$$F = F_{\mathrm{spring}} + F_{\mathrm{dissipative}}. \tag{4.6}$$

In this representation, friction forces adhere the mass to a planar surface. A displacement of the mass m leads to a conservative spring force F_{spring} which is described by Hooke's law

$$F_{\text{spring}} = -k_{\text{spring}} \cdot x_{\text{mass}}. \tag{4.7}$$

In order to specify $F_{\text{dissipative}}$ in this case, viscous damping and constant friction are considered for the interaction with respect to the relative velocity $v_{\text{r}} = v_{\text{mass}} - v_{\text{surface}}$. The viscous damping term[16]

$$F_{\text{viscous}} = -\gamma \cdot v_{\text{r}}, \tag{4.8}$$

is proportional to the relative velocity v_{r} between mass and surface. The resulting linear damped harmonic oscillator is not suitable to describe the experimental non-linear amplitude response.
The non-linear interaction term F_{const} is given by a constant friction force $F_{\text{friction}} >= 0$ [34] which is independent regarding the sliding velocity

$$F_{\text{const}} = -F_{\text{friction}} \cdot \text{sgn}(v_{\text{r}}). \tag{4.9}$$

Taking the conservative and dissipative forces into account, Newton's equation of motion describing the spring-mass oscillation can be derived

$$m \cdot \ddot{x}_{\text{mass}} = -k_{\text{spring}} \cdot x_{\text{mass}} - F_{\text{friction}} \cdot \text{sgn}\left(v_{\text{r}}\right) - \gamma \cdot v_{\text{r}}. \tag{4.10}$$

The temporal evolution of the mass position x_{mass} is calculated by using a numerical algorithm (see Appendix). The Euler Richardson method is suitable to solve Newton's equation of motion including velocity-dependent friction forces [83]. All acting forces are determined to calculate the mass position. Using the actual acceleration $\ddot{x}_{\text{mass}}$, the half-step method determines velocity $\dot{x}_{\text{mass}}$ and position x_{mass} for the next time step $t + \Delta t$ by calculating midpoint values $\dot{x}'_{\text{mass}}$ and x'_{mass} at $t + \Delta t/2$. The algorithm provides all necessary system parameters of the mass and off-resonant surface movement to simulate the mass oscillation x_{mass}.

4.1.3 Simulation: Amplitude Response Caused by Modulation Excitation

The equation of motion Eq. 4.10 is the initial point to describe the experimental data. In a first step the equation is used to simulate the off-resonant amplitude response of the bending oscillation in Fig. 4.2. A friction force of $F_{\text{friction}} = 20$ nN is assumed and viscous damping is neglected to match experiment and simulation [34].
The algorithm calculates the mass oscillation for each off-resonant frequency f_{mod} by applying a modulation amplitude of $A_{\text{mod}} = 10$ nm. A fast Fourier transformation extracts the relevant frequency components from the calculated mass oscillation. The simulated amplitude response in Fig. 4.5 (a) exhibits a qualitative agreement for the even and odd

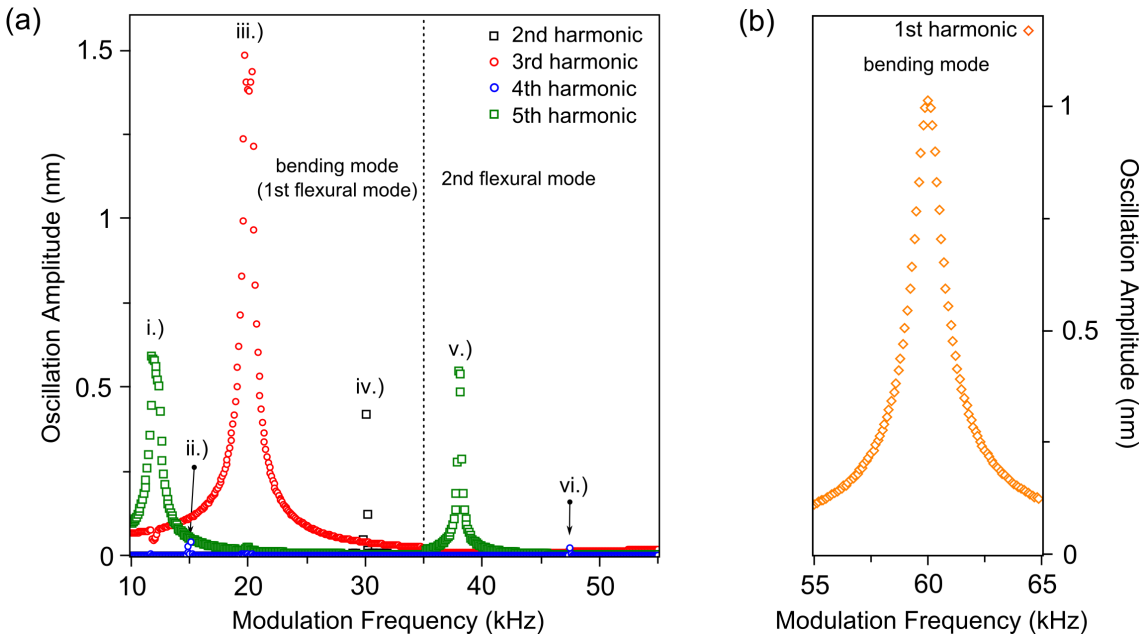

Figure 4.5: (a) Simulated amplitude response of the second to fifth harmonic with a friction force $F_{\text{friction}} = 20$ nN and a modulation amplitude of $A_{\text{mod}} = 10$ nm. The signal at integer fractions i.) - iv.) of the resonance matches qualitatively the experimental data in Fig. 4.2. (b) Simulated amplitude response of the bending resonance mode $\gamma = 0.9 \cdot 10^{-6}$ Ns/m with a modulation amplitude of $A_{\text{mod}} = 1$ nm.

integer harmonics. Signals are excited at integer fractions of the resonance frequency $f_{\text{mod}} = f_{\text{res}}/n$ with $n = 1, ..., 5$ like in the experiment. Furthermore, the third harmonic component features the best signal to noise ratio.
An excitation of response oscillations for the 2nd flexural mode are also simulated. The spring constant is chosen as $k = 1755$ N/m to match the resonance of the spring-mass system with the experimental resonance frequency of the 2nd flexural mode.
Viscous damping $\gamma = 0.9 \cdot 10^{-6}$ Ns/m ($F_{\text{friction}} = 0$ nN) is considered to simulate the amplitude response of the bending mode resonance. The data are received as first harmonic around $f_{\text{res}} = 60$ kHz in Fig. 4.5 (b).
The real-time oscillations of the cantilever bending mode in Fig. 4.3 can also be described by Eq. 4.10. In order to reproduce the oscillation characteristics, a friction force of $F_{\text{friction}} = 120$ nN is estimated for the contact between a silicon tip and a silicon surface. A considerable smaller friction force of $F_{\text{friction}} = 70$ nN for the second contact is required, consisting of a silicon tip and a graphite surface. A modulation amplitude of $A_{\text{mod}} = 1$ nm is applied for both simulations and viscous damping is neglected.
Using the simulations to make a qualitative statement, the degree of non-linearity apparently depends on the friction force. For a given modulation amplitude, a higher friction interaction causes a smaller $\mathcal{N}$ compared to lower friction forces. Contrarily, the oscillation amplitude is increased in the time domain for higher interaction forces.
In Figure 4.7 the simulated development of $\mathcal{N}$ and the sum of the Fourier amplitudes $A = A(f_{\text{res}}/3) + A(f_{\text{res}})$ depending on the acting friction force F_{friction} are depicted. These data confirm the trend of increased oscillation amplitudes and decreased non-linearity

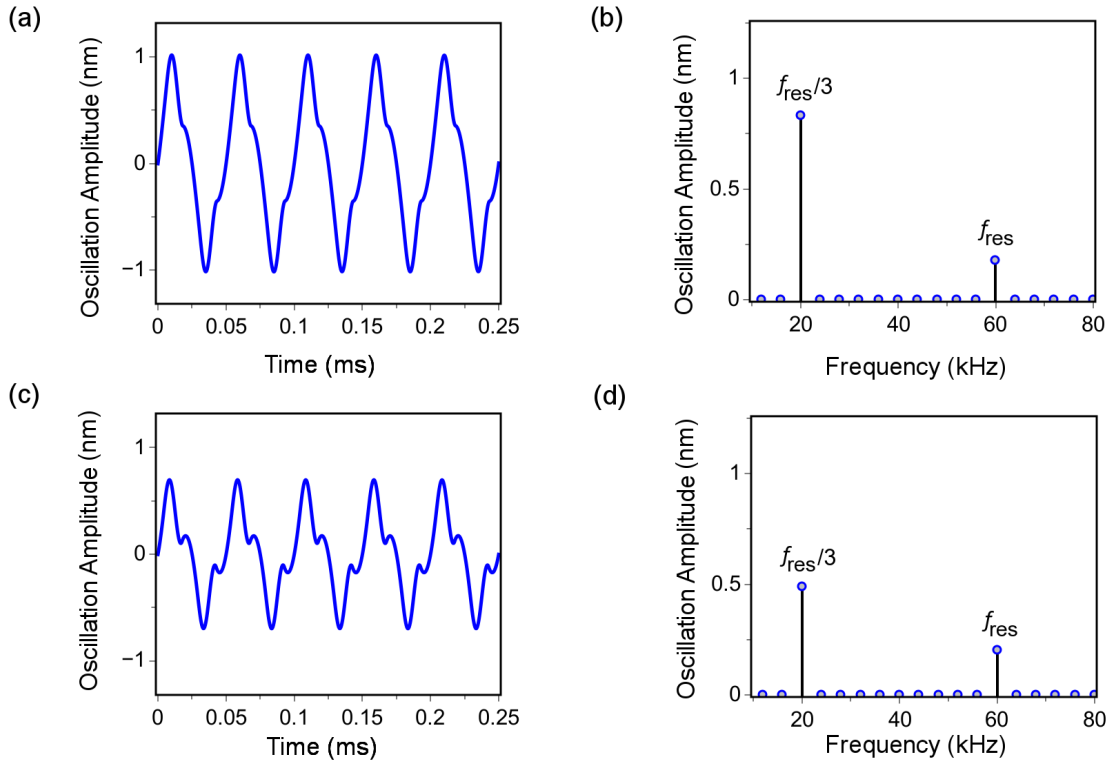

Figure 4.6: Simulated oscillation at a fixed modulation frequency of $f_{\mathrm{mod}} = f_{\mathrm{res}}/3 = 20$ kHz. A friction force of $F_{\mathrm{friction}} = 70$ nN (a, b), respectively a friction force of $F_{\mathrm{friction}} = 120$ nN (c, d) is chosen to match experimental (Fig. 4.3) and simulated data qualitatively.

for higher friction until the non-linear to linear transition is reached. At the transition point, friction is sufficient to bound the mass to the surface and the oscillation follows the modulation movement directly.

4.1.4 Non-linear Stick-Slip Interactions

Experimental and simulated data show that an off-resonant longitudinal modulation at integer fractions of f_{res} excites resonance oscillations of the bending mode. In order to characterize the movement states, especially the composition of the oscillation in the time domain, it is assumed that the excitation mechanism is found in stick and slip parts of the tip [59]. In analogy to the resonance oscillation of a violin string caused by a steady movement of a bow, the cantilever oscillation consists of static and sliding friction parts. Here, in the case of a harmonic excitation, the longitudinal friction force regulates an energy transfer between modulation and lever vibration by applying the stick-slip mechanism.
The relative velocity v_{r} between tip and surface is given by

$$v_{\mathrm{r}} = v_{\mathrm{tip}} - v_{\mathrm{surface}}, \tag{4.11}$$

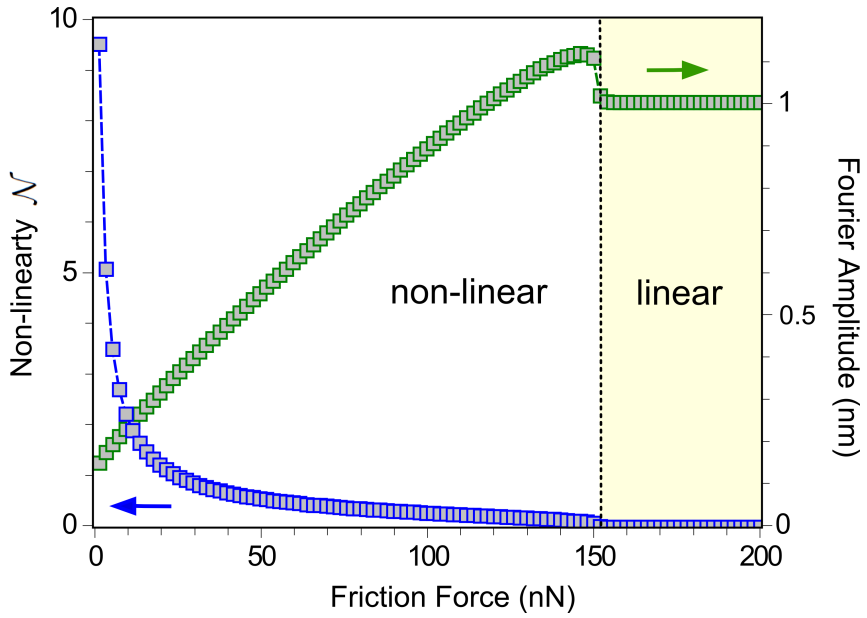

Figure 4.7: At a given modulation amplitude $A_{\mathrm{mod}} = 1$ nm the response oscillation amplitude, as well as the non-linearity depend on the acting friction force F_{friction} (2 nN - 200 nN). Simulated data confirm that the degree of non-linearity disproportionately drops with increasing friction. Instead, the sum of the Fourier amplitudes $A = A(f_{\mathrm{res}}/3) + A(f_{\mathrm{res}})$ increases until the transition from linear to non-linear oscillation is reached. At the transition point, a remaining non-linearity disappears and the oscillation is fulfilled with the modulation amplitude A_{mod}.

A relative movement between tip and surface is performed for $|v_{\mathrm{r}}| > 0$. The tip slides across the surface which is referred to as slip part. In the case of $v_{\mathrm{r}} = 0$, the movement of tip and surface is equal and the tip sticks to the surface.
Due to a permanent relative motion between tip and surface, the bending oscillation alternates between both interaction parts. The transition from static to sliding friction will take place if the restoring lever force $F_{\mathrm{spring}} = -k_{\mathrm{spring}} \cdot x_{\mathrm{mass}}$ overcomes the longitudinal acting friction force $F_{\mathrm{friction}} >= 0$ between tip and surface

$$|F_{\mathrm{spring}}| > F_{\mathrm{friction}}. \tag{4.12}$$

Furhtermore, re-adherence of the tip will arise for small lever deflections $|F_{\mathrm{spring}}| < F_{\mathrm{friction}}$ if the relative velocity v_{r} vanishes

$$|v_{\mathrm{r}}| \to 0. \tag{4.13}$$

This type of non-linear interaction forms the basic principle of friction induced oscillations. In Fig. 4.8 the oscillation sequence is schematically illustrated for the case of a constant surface movement. Within this representation, stick and slip parts are fulfilled successively and consequently a non-linear oscillation is maintained.
Instead of a constant surface movement, the non-linear oscillation caused by a harmonic oscillation of the surface is also constituted by the stick-slip interaction between tip and surface. The non-linearity of the oscillation $\mathcal{N}$ is directly associated with the ratio of stick and slip parts during oscillation. Furthermore, this ratio obviously depends on the

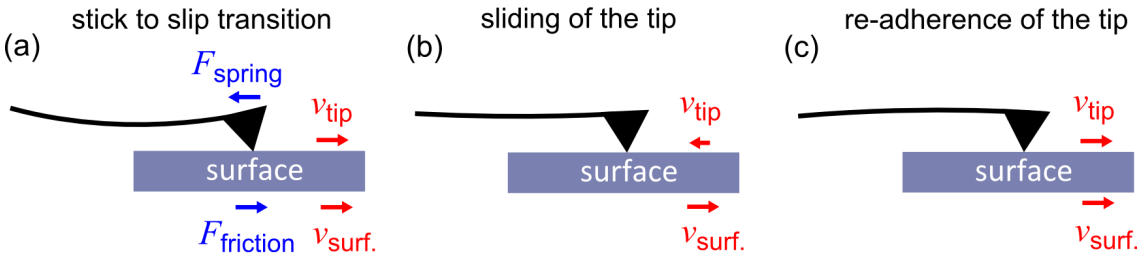

Figure 4.8: A surface movement with constant velocity leads to stick-slip interaction of a cantilever tip which is in contact with the surface. (a) The restoring lever force overcomes the sticking force and the tip starts to slide over the surface. (b) The cantilever relaxes and the tip slides in the opposite direction. (c) The tip adheres to the sample surface due to vanishing relative velocity.

acting friction force. A detailed analysis of the stick-slip interaction in correlation with the non-linear oscillation is presented in the next section.

4.2 Resonant Cantilever Response of Static-to-Sliding Transitions

In a dynamic case, stick and slip interactions are responsible for friction induced and non-linear oscillations. Otherwise, the transition from static-to-sliding friction is of interest regarding physical phenomenons like frictional aging or frictional anisotropy. On the nanometer scale, these effects have been under investigation recently [50, 51, 49].
For the $f_{res}/3$ modulation a cantilever resonance response is approved in the preceding section and furthermore, a transition from linear to non-linear bending oscillation is assumed. In order to give an idea of how stick-slip interactions are correlated with the transition from linear to non-linear oscillation during an off-resonant surface modulation, the lever response oscillation depending on the modulation amplitude is investigated. Thus, the composition of the non-linear oscillation is illustrated. This insight paves the way to introduce a sample surface imaging technique which maps friction forces at the static-to-sliding transition.

4.2.1 Resonant Cantilever Response of Static-to-Sliding Transitions

The fast Fourier transformation of a non-linear cantilever bending oscillation for a given modulation amplitude A_{mod} exhibits that the real-time oscillation consists of a modulation $f_{mod} = f_{res}/3$ and a bending resonance f_{res} component. Furthermore, it is assumed, that the interaction between tip and surface consists of stick and slip parts whose ratio depend on the acting friction force.
The transition from linear to non-linear cantilever response is experimentally investigated in a next step. A graphite surface is scanned to find an appropriate area with few defects

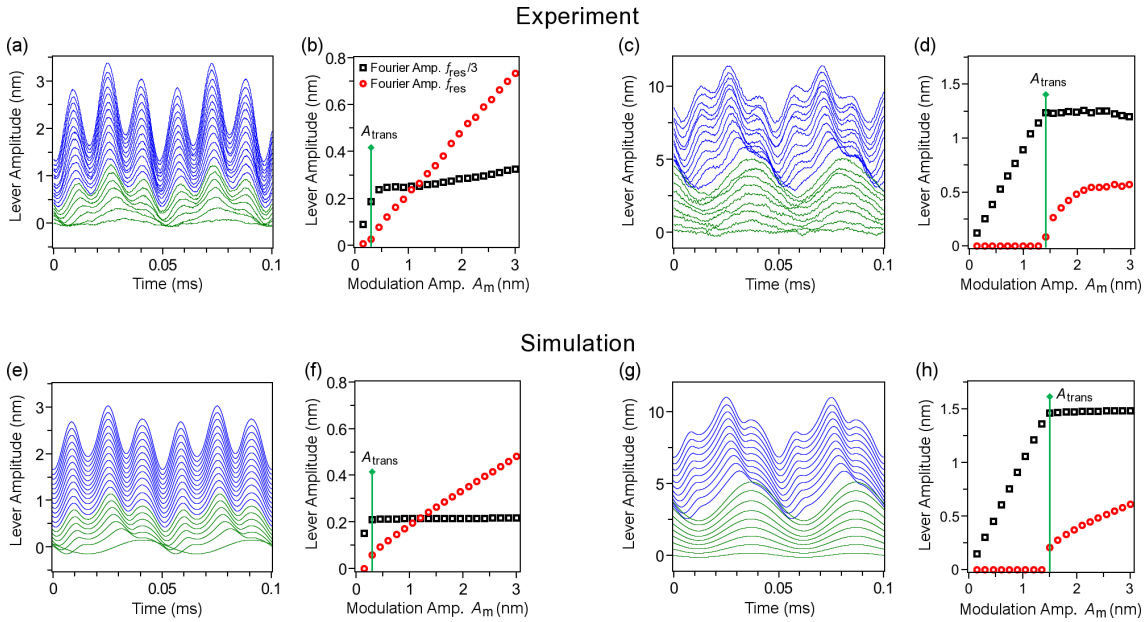

Figure 4.9: Experimental (a)-(d) and simulated (e)-(h) local transitions from linear (green line) to non-linear (blue line) lever oscillation by applying a modulation frequency $f_{\mathrm{res}}/3$. The modulation amplitude A_{mod} is stepwise increased and the lever oscillations in the time domain are shown as a waterfall plot. The Fourier amplitudes of $f_{\mathrm{res}}/3$ and f_{res} in the response are taken from the fast Fourier transformation. At the transition amplitude A_{trans} the resonance component arises. A substantial variation of A_{trans} between a freshly cleaved HOPG ((a) and (b)) surface and a contaminated HOPG surface ((c) and (d)) can be observed. Simulated data show the qualitative development of the frequency components for both friction contacts (e)-(h). (*Figure is published in Applied Physics Letters, 104 (2014) 113105*)

for an experimental run. Starting at low-level, the modulation amplitude is increased stepwise and the modulation frequency is set to one third of the resonance frequency. The amplitudes of both frequency components are determined from the fast Fourier transformation of the averaged real-time oscillation and damping induced resonance shifts have been compensated.

The real-time oscillations, as well as the development of both frequency components $A(f_{\mathrm{res}}/3)$ and $A(f_{\mathrm{res}})$ concerning two different friction contacts are depicted in Fig. 4.9 (a) to Fig. 4.9 (d) and indicate a transition from linear to non-linear bending oscillation of the lever.

The first contact consists of a sharp tip in combination with a freshly-cleaved HOPG surface. For the clean HOPG surface in Fig. 4.9 (b) only the first data indicates a linear response oscillation. After the transition amplitude $A_{\mathrm{trans}} = 0.3$ nm is exceeded the response oscillation becomes non-linear, according to an arising third harmonic component in the fast Fourier transformation. A second contact consists of a contaminated HOPG surface in contact with a blunt tip. The surface is exposed to air for an extended time. The data in Fig. 4.9 (d) show a similar transition behavior, but the onset of the non-linear response occurs at a much higher modulation amplitude $A_{\mathrm{trans}} = 1.4$ nm.

The phenomenological model in Sec. 4.1.2 is used to understand the underlying tip-sample interaction in Fig. 4.10. In this case, the interaction between spring-mass system and the

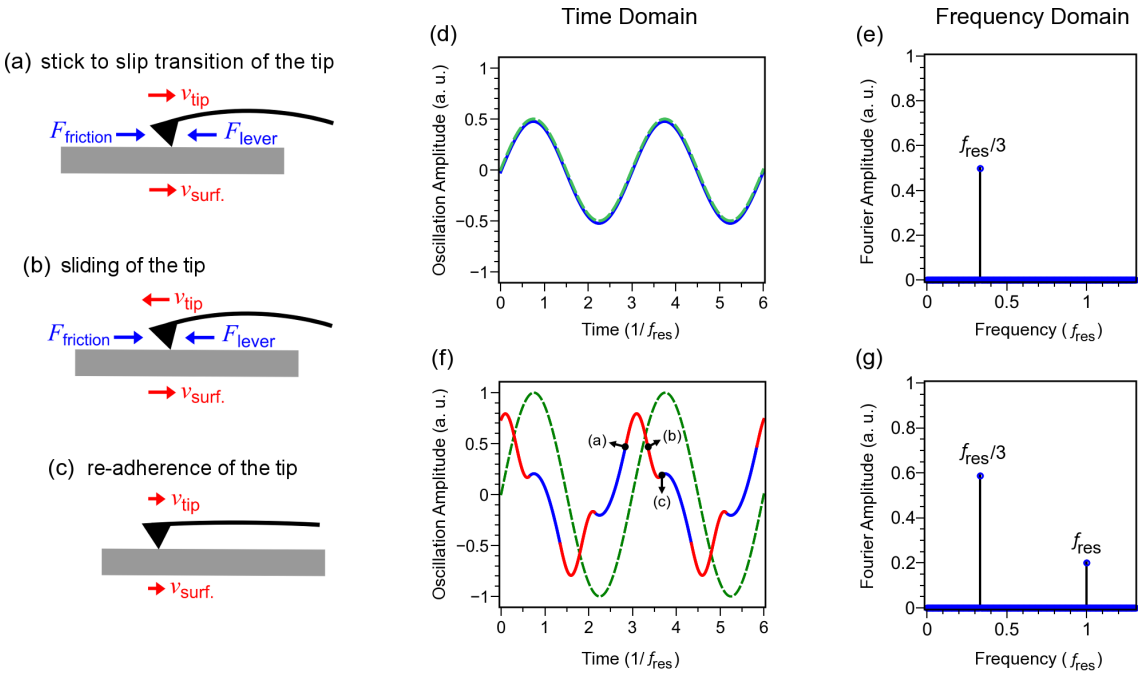

Figure 4.10: Simulated cantilever tip and sample surface interactions during a modulation using a frequency $f_{mod} = f_{res}/3$. For an insufficient modulation amplitude (green dashed line), the tip follows the modulation movement (blue line) and a linear cantilever response results (d). In the Fourier analysis (e), the lever frequency matches the frequency of the modulation $f_{res}/3$. With increasing modulation amplitude, the restoring force of the lever overcomes the friction threshold, and a resonance content (red line) in the response oscillation can be recognized (f). In the Fourier analysis (g), a resonance content f_{res} appears as third harmonic of the modulation frequency $f_{res}/3$. Adherence of the tip occurs (c) if the relative velocity between tip and sample becomes vanishingly low. (*Figure is published in Applied Physics Letters, 104 (2014) 113105*)

surface consists of a constant longitudinal force value $F_{friction}$ and no distinction between static and sliding friction is taken into account [34]. Viscous damping is furthermore neglected.

During the off-resonant $f_{res}/3$ excitation, the response oscillation differs between two states of oscillation. Concerning small modulation amplitudes, the friction force adheres the mass to the surface and a linear response results in Fig. 4.10 (d).

After the transition amplitude is reached, a non-linear oscillation is excited. The mass slips partially across the surface while the spring-mass system oscillates at its natural frequency f_{res} (Fig. 4.10 (g)).

The experimentally transition from linear to non-linear cantilever response is reproduced in Fig. 4.9 (e) - (h). For the first contact a friction force of $F_{cleaved} = 30$ nN is required to match experiment and simulation Fig. 4.9 (e) and (f). Here, the longitudinal position of the fiber, with respect to the cantilever, affects the slope of the resonance component. A considerable higher friction force of $F_{contaminated} = 210$ nN is estimated for the second contact due to higher load and a contact between a blunt tip and a contaminated surface [46].

Higher friction forces enlarge the linear response range due to increased stick parts of the lever tip. In Fig. 4.11 (a) the resonant lever response $A(f_{res})$ are simulated for different

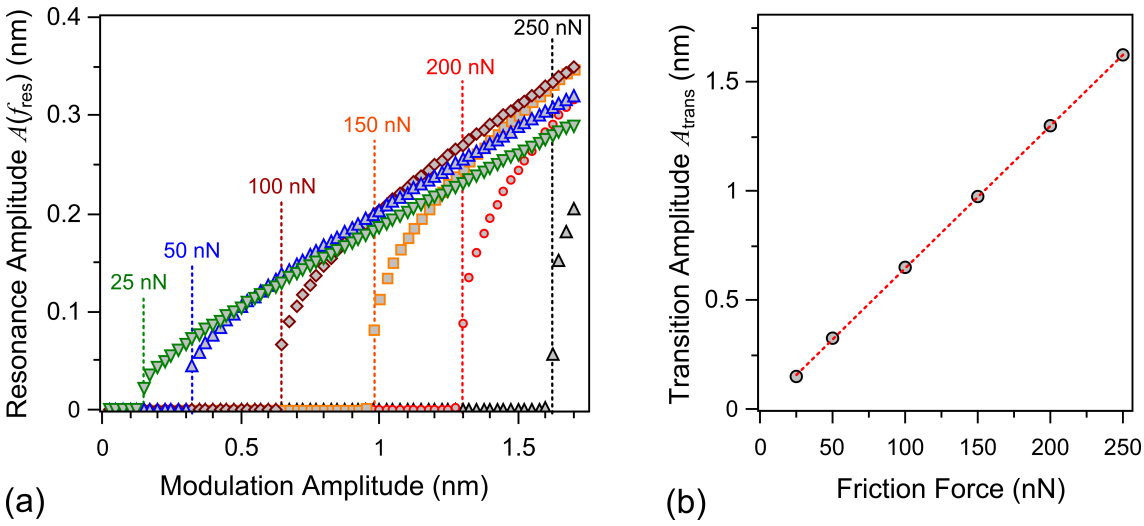

Figure 4.11: (a) Simulations of resonant lever responses $A(f_{\mathrm{res}})$ caused by an increasing of the modulation amplitude. The transition amplitudes A_{trans} from linear to non-linear oscillation can be determined concerning different friction forces F_{friction}. (b) The corresponding amplitudes A_{trans} linearly depend on the acting friction force F_{friction}.

friction forces F_{friction}. The resulting transition amplitudes A_{trans} linearly depend on the acting friction force. The arising of resonance signal is directly related to F_{friction}.
As a conclusion, a resonant cantilever response appears if the transition from stick-to-slip, respectively static-to-sliding friction takes place. Moreover, the transition amplitude A_{trans} is directly related to the acting friction force between tip and surface.

4.2.2 Synchronization, Stick-Slip Transitions and Frictional Aging

Stick and slip interactions are directly connected with the transition from static-to-sliding friction. An increased static friction force due to frictional aging during the stick parts can influence the sequential flow of stick-slip transitions and modifies the non-linear oscillation. Experimental and simulated data show that stable non-linear oscillations occur if the modulation frequency matches an integer fraction of the resonance frequency $f_{\mathrm{mod}} = f_{\mathrm{res}}/n$ with $n = 1, ..., 5$. The effective Q factor governs the frequency distribution around these frequencies. Moreover, the best signal to noise ratio is being achieved for an $f_{\mathrm{res}}/3$ excitation frequency.
In these cases a synchronization between cantilever and modulation oscillations is assumed as the determining factor. For the $f_{\mathrm{res}}/3$ excitation, the non-linear oscillation consists of stick parts leading to a modulation frequency component $f_{\mathrm{res}}/3$ and slip parts leading to a resonance frequency component f_{res} in the time domain. These two frequency components are synchronized and a non-linear lever oscillation with a defined period results. In contrast to other frequencies a stable non-linear oscillation with a defined period is not possible due to a periodical mismatch between modulation and resonance oscillation parts.
In Fig. 4.12 the simulated relative velocity v_{r} for $f_{\mathrm{res}}/3$ excitations is depicted with respect to an increasing modulation amplitude. The cantilever tip reaches relative velocities up

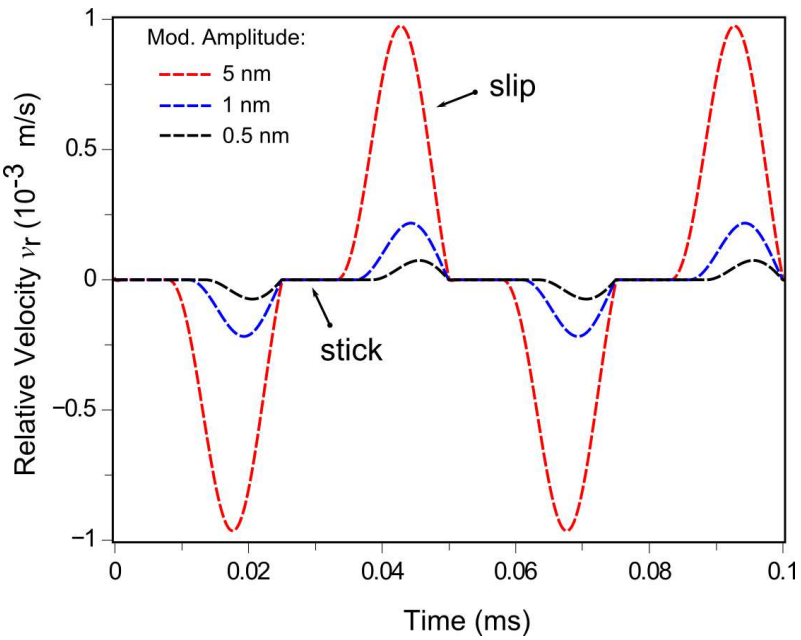

Figure 4.12: Simulated relative velocities v_r concerning different modulation amplitudes A_mod for a $f_\mathrm{res}/3$ excitation. Velocities up to several hundreds of micrometers per second between tip and surface can be reached. During the stick parts the relative velocity vanishes. Stick and slip parts are synchronized and consequently an oscillation with a defined period results. Moreover, for increasing modulation amplitudes the proportion of stick parts decreases.

to several hundreds of micrometers per second in experiments.
Resting times of the tip during the stick parts are in the range of several microseconds to tens of microseconds. In common experiments which measure an influence of frictional aging on the nanometer scale, hold times are in a range of several seconds to minutes [50]. Sticking periods in dynamic friction force microscopy are consequently $10^5 - 10^6$ times shorter. Apparently, frictional aging has not to be considered for discussions of stick-slip induced non-linear cantilever oscillations.
In summary, a simple constant friction force F_friction is sufficient to describe off-resonant induced non-linear cantilever oscillation which consist of stick and slip parts between tip and surface.

4.3 Non-linear Friction Imaging Technique

The transition amplitude A_trans from linear to non-linear oscillation is supposed to depend linearly on the friction force. In order to realize a friction imaging technique which makes use of this transition, the modulation amplitude can be controlled by a feedback setup.
The experimental setup, discussed in Chap. 3, can be used as feedback-controlled amplitude excitation technique, as well as a constant amplitude excitation imaging technique. The non-linear lock-in signal is used to control the modulation amplitude for the feedback controlled imaging technique in Fig. 3.14. Varying longitudinal interactions between tip and sample affect the non-linear response of the cantilever and the control voltage of the

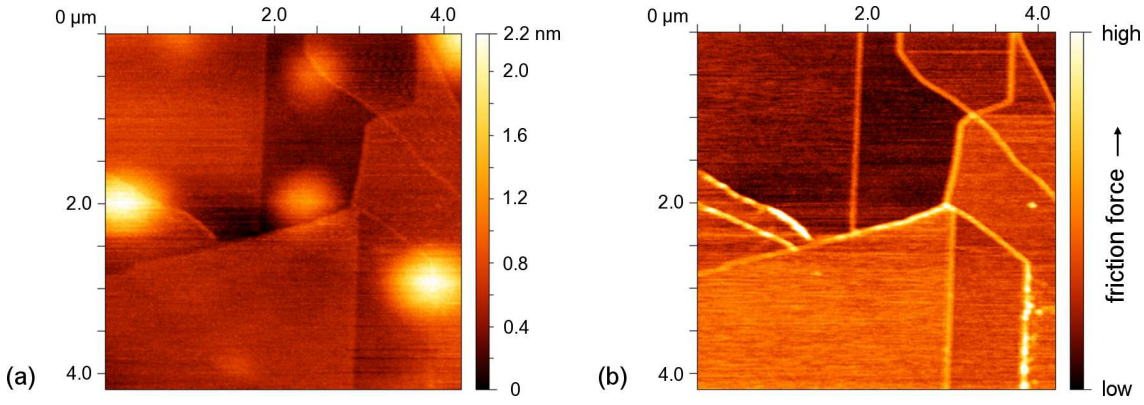

Figure 4.13: Image recording on a contaminated HOPG surface. (a) The topography signal from the digital feedback shows atomic steps, as well as bubble like structures possibly caused by micron size inclusions. (b) The simultaneously recorded signal of the feedback controlled transition amplitude A_{trans} as a measure of the friction information. Atomically steps are shown as highlighted lines caused by an increased modulation amplitude. Furthermore, small surface defects can be seen as highlighted spots. In addition, an area contrast between different parts of the friction image can be recognized. (*Figure is published in Applied Physics Letters, 104 (2014) 113105*)

modulation amplitude is a direct measure of the friction force.
In contrast, an excitation of the modulation piezo with constant amplitude can also reflect tribological properties of surfaces.

4.3.1 Feedback-Controlled Amplitude Excitation Imaging Technique

The steep increase in the non-linear cantilever response which is caused by the onset of tip sliding can be used as feedback signal to control the modulation amplitude A_{mod}. Simultaneously, a scanning movement of the cantilever in constant deflection mode detects

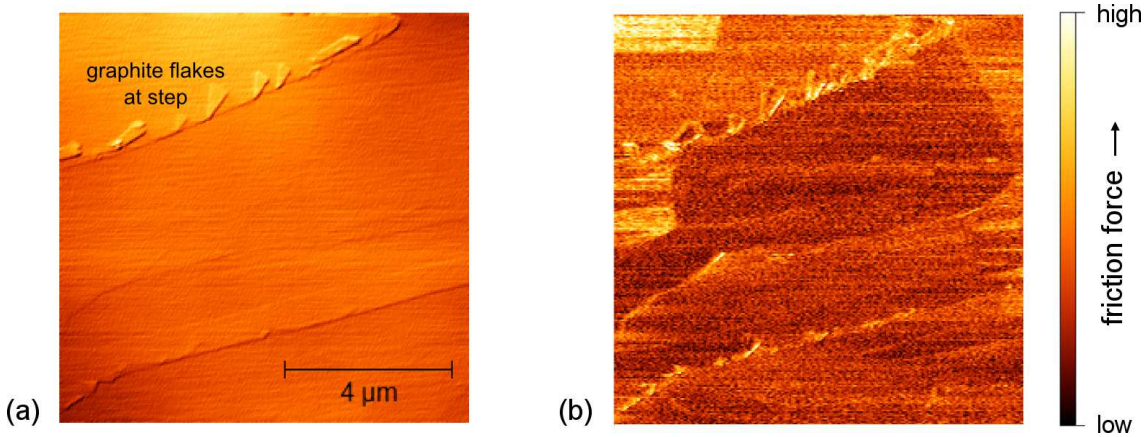

Figure 4.14: Modulation feedback technique applied on a graphite B-grade surface. (a) The gradient image of the surface topography reveals abrasion at surface steps due to higher load forces. (b) In the friction image graphite flakes and smaller grains are detected.

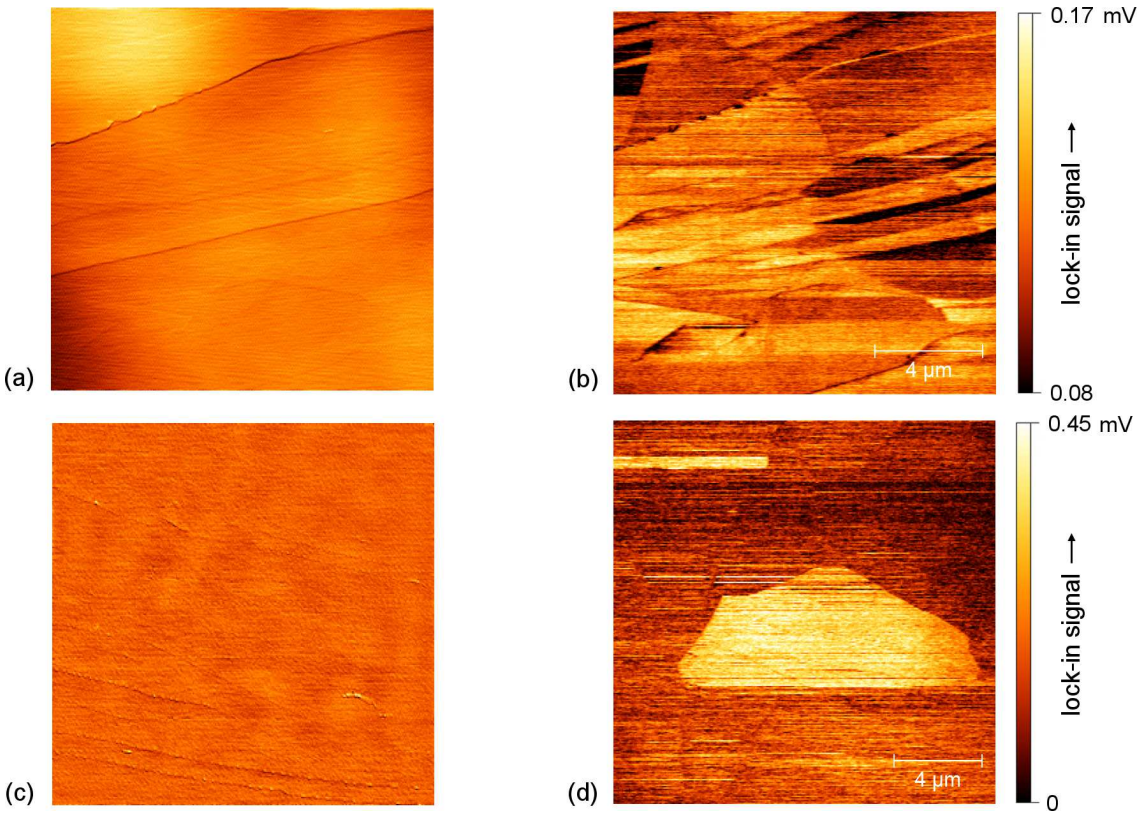

Figure 4.15: Constant excitation imaging technique on an HOPG B-grade surface. (a, c) The gradient images of the topography show a flat surface with a few surface steps. (b, d) The corresponding dynamic friction images are dominated by contrast inversions and reveal the shapes of graphite grains.

the topography of the sample surface.
The modulation feedback setup (Fig. 3.14) applies the $f_{\mathrm{res}}/3$ signal to the modulation piezo and the third harmonic signal is extracted by the lock-in amplifier. The feedback maintains a defined lock-in signal at the transition amplitude A_{trans} to provide a modulation amplitude which reflects the friction interaction at the tip-sample contact. As already pointed out, increasing friction results in an extended linear oscillation range and causes extended sticking parts. Applying this technique during the scanning of a surface, the feedback signal displays a higher modulation amplitude at higher friction contacts to reach the increased transition amplitude A_{trans}. A detection of the feedback signal consequently contains a local friction information of the tip sample contact.
This method is applied on a graphite A-grade surface (mosaic spread: 0.4° - 0.8°) which shows a small density of surface steps because of a high grain size. The surface is contaminated due to an extended storage under vacuum conditions. A blunt cantilever tip is used as force sensor. As presented in Sec. 2.4.1, higher load forces provoke higher friction forces and the level of A_{trans} is increased. An increased modulation level ensures a feedback controlled imaging of friction. This technique breaks down in the case of low load forces and low friction. In this case, even a modulation amplitude full range is not applicable to induce an appreciable resonance signal.

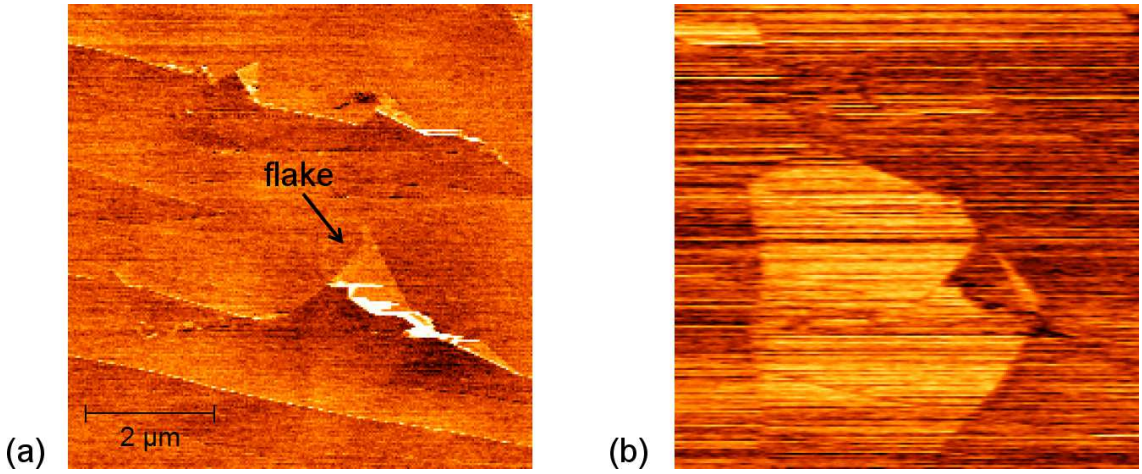

Figure 4.16: (a) Besides surface steps, the topography image depicts a folded graphite flake which is turned over by the cantilever tip in constant excitation mode. (b) In the dynamic FFM image, the flake shows a darker contrast as the grain and confirms that the contrast formation can be explained by the flake scenario.

The scanning of the HOPG surface exhibits atomic steps as highlighted lines caused by higher friction at step edges (Fig. 4.13). An area contrast between different parts of the image can be recognized which could be caused by friction anisotropy. Different grain orientations could influence the friction force at the local tip-sample contact.
The modulation feedback technique is furthermore applied on a clean HOPG B-grade (mosaic spread: 0.8° - 1.2°) surface. The lower quality of the sample causes smaller grain sizes and a higher density of grain boundaries and surface steps. A higher load force causes abrasion at surface steps which can be recognized in the gradient image of the topography (Fig. 4.14 (a)). Graphite flakes are pulled off from the surface at the edge.
In the friction image an area contrast can be recognized which has the typical size and shape of a graphite grain. A separated flake at the surface step is attached to the tip and the contact consists of two graphite surfaces. A varying lattice orientation of the underlying surface leads to frictional anisotropy. The friction force at the tip-sample contact is affected by a matching or mismatching of the graphite lattices concerning their 60° symmetry [55]. The modulation amplitude is decreased on the grain due to a commensurate matching of the layers.
In summary, the modulation amplitude feedback technique depicts tribological properties of surfaces in the view of friction anisotropy and increased friction forces at surface defects.

4.3.2 Constant Amplitude Excitation Imaging Technique

A constant amplitude excitation of the harmonic vibrating sample surface leads to a lock-in signal which can directly be detected as friction information. In contrast to a feedback controlled modulation amplitude, the reference source in the experimental setup (Fig. 3.13) applies a harmonic voltage signal with constant amplitude to the modulation piezo. The simulated development of the resonance amplitude $A(f_{\mathrm{res}})$ in Fig. 4.17 depicts that the lock-in signal is not clearly attributable. Furthermore, the third harmonic signal dis-

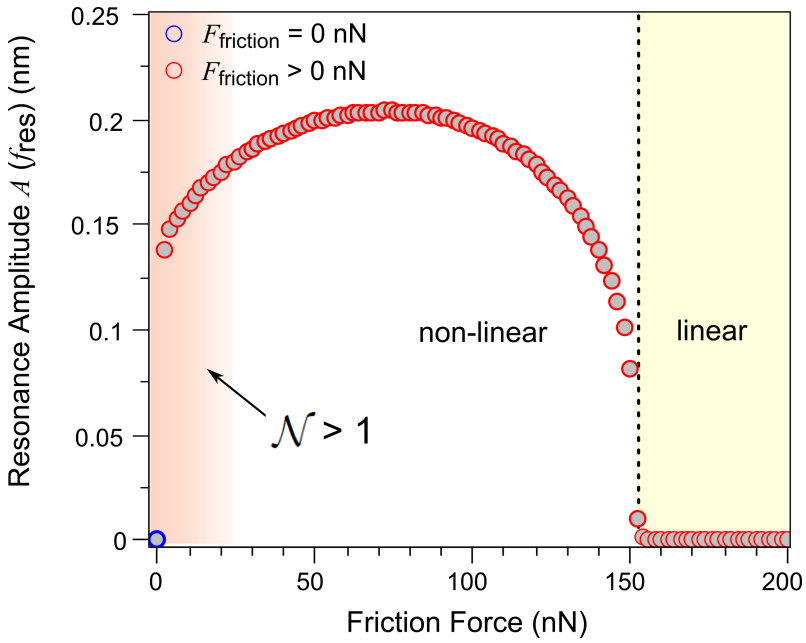

Figure 4.17: The red circles show the simulated resonance amplitude $A(f_{\text{res}})$ of Fig. 4.7. The ambiguity of the signal development impedes an interpretation of friction images. In addition, the blue circle is added to depict the response for a vanishing small friction interaction.

appears at higher friction forces.
This technique is applied on an HOPG B-grade sample surface with a modulation amplitude of $A_{\text{mod}} = 1$ nm. The topography image (Fig. 4.15 (a)) shows a flat surface with a few surface steps. The dynamic friction image (Fig. 4.15 (b)) reveals areas of varied signal amplitudes, where the contrast mechanism permanently flips. These contrast flips can be explained by the presence of a graphite flake which is attached to the tip as well. During scanning, the flake rotates and adjusts oneself to the surface lattice orientation. The frictional interaction rapidly changes and therefore the lock-in signal as well.
The constant excitation mode is also usable to reveal a contrast mechanism caused by graphite grains in Fig. 4.15 (d). A grain is highlighted due to a frictional interaction between the attached graphite flake and the surface. When the flake rotates, the frictional influence vanishes and the contrast in the image disappears. In Fig. 4.16, a folded graphite flake is turned over on the surface by the cantilever tip and therefore the lattice orientation is changed. The dynamic friction image shows a different contrast on the flake and confirms that the contrast formation can be explained by the flake scenario.
The development of the resonance amplitude $A(f_{\text{res}})$ in Fig. 4.17 in the low-friction range ($\mathcal{N} > 1$) can be used as an imaging technique (Chap. 6). Low load forces lead to low friction on HOPG and a resonance component is not induced during the scan of surfaces in the case of vanishingly low friction (blue circle). By hitting a frictional barrier in this range, for example, resonance pulses are excited (red circles) and the lock-in releases a short signal. The fractional resonance excitation technique is applied to metallic nanoparticles in a next step for an investigation of tip-sample interactions on different materials.

4.4 Conclusion

The fractional resonance excitation in the direction of the cantilever long-axis excites oscillations of the cantilever beam at resonance if the modulation frequency matches an integer fraction of the cantilever bending mode resonance $f_{\mathrm{mod}} = f_{\mathrm{res}}/n$ with $n = 1, ..., 5$. Moreover, the best signal to noise ratio is achieved for an excitation of the third harmonic $f_{\mathrm{mod}} = f_{\mathrm{res}}/3$. A fast Fourier transformation of the bending real-time oscillation exhibits that the vibration is composed of modulation f_{mod}, as well as resonance frequency f_{res} components.
Based on this experimental data, a phenomenological spring-mass system is developed to simulate the oscillation state of the lever bending mode at fractional excitations. Here, a constant friction value F_{friction} provokes a non-linear oscillation of the spring-mass system. Stick and slip interactions between tip and surface excite resonance oscillations of the cantilever beam. If the relative velocity between tip and surface vanishes, the friction adheres the tip to the surface and the cantilever vibrates at the modulation frequency f_{mod}. Due to the dynamic movement of the system, the lever spring force can overcome the friction force and the tip starts to slide over the surface, where the beam vibrates at its resonance frequency f_{res} until the relative velocity vanishes again. It is found that a synchronization of stick and slip parts is responsible for the non-linear oscillation at $f_{\mathrm{mod}} = f_{\mathrm{res}}/3$.
The friction force determines the non-linearity of the oscillation for a given modulation amplitude. The static-to-sliding transition is directly related to the transition from linear to non-linear oscillation. The transition amplitude A_{trans} of the modulation linearly depends on the acting friction force F_{friction}.
Furthermore, a constant force F_{friction} sufficiently describes the conditions during the static friction range. A discontinuity between static and sliding friction is not considered and consequently an influence of frictional aging is not observed during the very short resting times of several microseconds.
In the last step a surface imaging technique is developed which maps local friction at the transition from stick-to-slip on graphite. A lock-in amplifier extracts the resonance amplitude $A(f_{\mathrm{res}})$ of the cantilever oscillation and a feedback controls the modulation amplitude A_{trans} at the transition from linear to non-linear bending oscillations. Images reveal an influence of friction interactions between two graphite layers. The commensurate or incommensurate matching of an attached graphite flake with the underlying surface [55] influences the feedback controlled modulation amplitude. Consequently, a contrast mechanism can be allocated to graphite grains which can be detected due to frictional anisotropy.

5 Dynamic FFM on Antimony Nanoparticles

Nanoparticles on surfaces represent an important sample system for the investigation of tribological properties between two materials [84, 85]. Various particle materials, ordered crystalline structures and defined contact areas of interfaces, are an advantage for the design and analysis of friction force experiments on the nanometer scale [86].
In friction force microscopy the torsional signal of the cantilever is affected by the slope of asperities and local gradients on the surface which influence the friction signal [87]. For torsional resonance microscopy (TR mode) it is found that the signal is less sensitive to variations in the topography [88]. In dynamic friction force microscopy (dynamic FFM) the resonance signal depends on the strength of the friction interaction. Furthermore, the topography of sample surfaces influences a contrast formation in dynamic friction images [61]. Variations of local surface gradients can cause shifts of the resonant frequency and lead to signal variations [59].
For a better understanding of a topographical crosstalk, the fractional resonance technique is applied to metallic nanoparticles with diameters of up to a few tens of nanometers and heights of up to several nanometers.
The signal contrast between the underlying sample material and the metallic particles offers further information about the resonance signal, respectively friction interactions on different materials.

5.1 Antimony Nanoparticles on HOPG

An evaporator (Knudsen cell) is mounted at a feedthrough on top of the UHV transfer chamber (Fig. 3.2) and vaporizes antimony onto sample surfaces in ultra-high vacuum at around 360 °C. Deposited antimony on graphite surfaces forms nanoparticles [89]. The

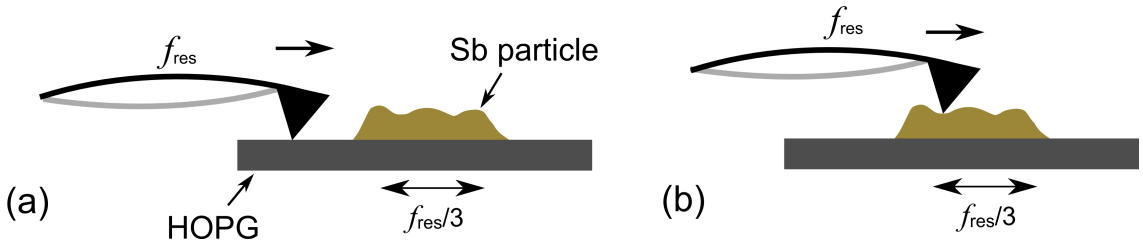

Figure 5.1: A cantilever scans a graphite surface (a) and an antimony nanoparticle (b). The sample is modulated at $f_{res}/3$ and a friction contact between tip and substrate excites resonance oscillations f_{res} of the cantilever beam. The resonance amplitude $A(f_{res})$ is monitored and provides information about friction interactions on HOPG and antimony (Sb).

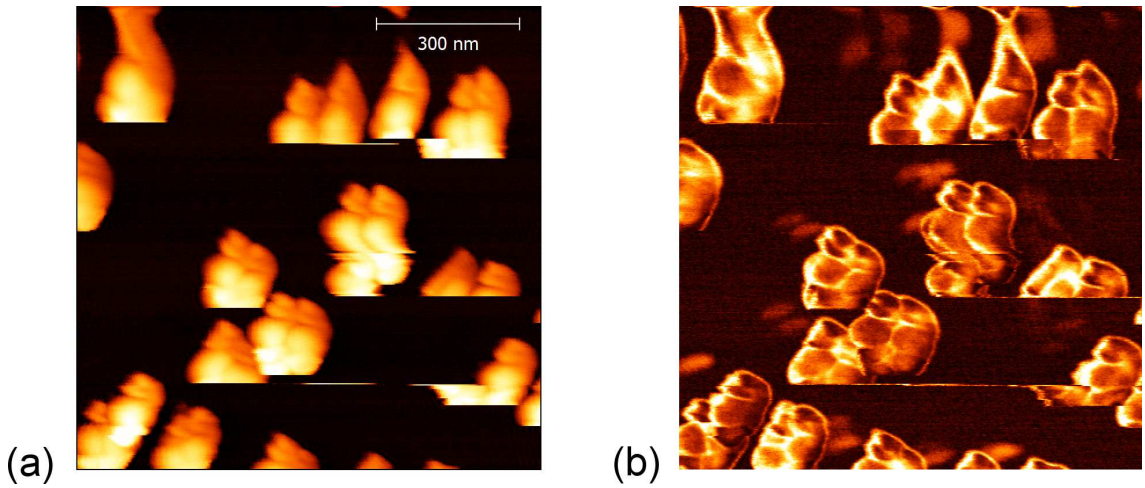

Figure 5.2: (a) Topography image of antimony nanoparticles on an HOPG A-grade surface. The interaction with a cantilever tip pushes them away and prevents a fully imaging of their shape. (b) Signal of the bending resonance oscillation caused by an off-resonance sample modulation at $f_{\mathrm{res}}/3$.

size of the particles can be controlled by the deposition rate and time. Sb_4 clusters conglomerate on the surface and amorphous nanoparticles start to grow with spherical shape [89, 90, 91]. At diameters of about 120 nm, antimony particles change their shape and fingerlink structures start to grow caused by a transition from an amorphous to a crystalline structure [90].
The fractional resonance method is applied to metallic nanoparticles on a graphite surface for an investigation of the non-linear signal response on different materials. The topography of particles shows high surface gradients and can influence the mechanic properties of cantilevers. Material dependent amplitudes and gradient induced frequency shifts of the free bending resonance frequency result and influence the contrast in dynamic friction images.

5.1.1 Nanoparticles on a High-Quality Graphite Surface

In a first experimental cycle, antimony is evaporated onto a graphite A-grade surface in Fig. 5.2. Amorphous nanoparticles cover the surface and are scanned with a cantilever tip in contact mode. The topography image (Fig. 5.2 (a)) shows particles with their typical shape and size.
Additionally, the surface is modulated with a constant modulation amplitude at $f_{\mathrm{res}}/3$ for a frictional excitation of the bending mode. The interaction of particles with the plane surface of the high-quality graphite sample is obviously weak and the tip pushes them out of their stable positions during scanning. Once the surface is scanned, a substantial manipulation in the arrangement of particles results and reproducible conditions are not possible. Moreover, the high mobility prevents long-term measurement at particles.
Focusing on friction, the resonance signal in Fig. 5.2 (b) indicates a topographical influence concerning the signal amplitude. The signal ampliutde on particles is obviously increased

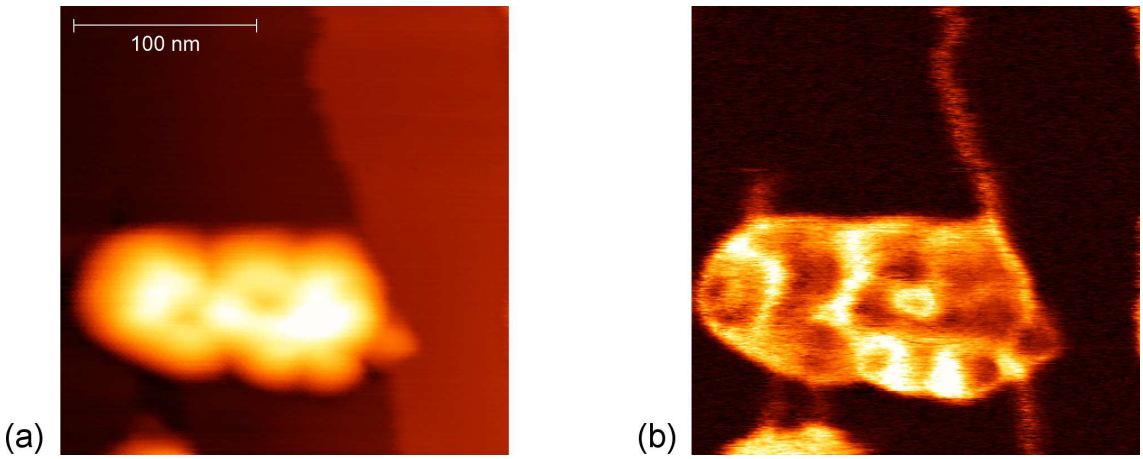

Figure 5.3: (a) The topography shows an antimony nanoparticle on a HOPG B-grade surface which is trapped between two surface steps. (b) Besides an increased signal at defects, the resonance signal on the particle is higher compared to the HOPG surface. Furthermore, signal variations on the particle are caused by topographical variations.

in contrast to the signal amplitude on the graphite surface. Nevertheless, the signal fluctuates and shows darker and brighter areas. A second sample system is prepared for a more detailed investigation of a topographical influence on the signal amplitude.

5.1.2 Nanoparticles on a Low-Quality Graphite Surface

In order to overcome the drawback of a high particle mobility on surfaces, antimony is evaporated onto a graphite sample with lower quality. HOPG B-grade samples exhibit surfaces with an increased amount of defects. A higher interaction at surface steps provides a stabilization of particle positions and prevents sliding and rotations of the particle. Fig. 5.3 depicts an antimony particle which is trapped between two surface steps and is scanned with a modulation amplitude of $A_{\mathrm{mod}} = 1.5$ nm and a frequency of 20.33 kHz. The particle stays firmly in the defect limited area, even after repeated imaging scans. Surface steps can be recognized in the friction image due to an interaction with the cantilever tip. Furthermore, the resonance amplitude is higher on the nanoparticle compared to the signal on the bare graphite surface. This indicates increased non-linear interactions on antimony.
The signal on antimony shows considerable variations due to a crosstalk with the particle topography. *Bhushan* [87] introduced the ratchet mechanism to discuss a topographical influence on friction during scanning a rough surface. Here, the tip-sample interaction depends on the slope of an asperity and the scanning direction in conventional FFM experiments. The friction signal is higher when the tip scans up a surface slope and smaller when it scans the slope down [92].
Fig. 5.4 shows a topography profile of the nanoparticle (Fig. 5.3) and the corresponding lock-in signal for a forward (trace) and backward (retrace) scan. Signal variations for both scans are similar and indicate that the signal amplitude does not depend primarily on the scanning direction.

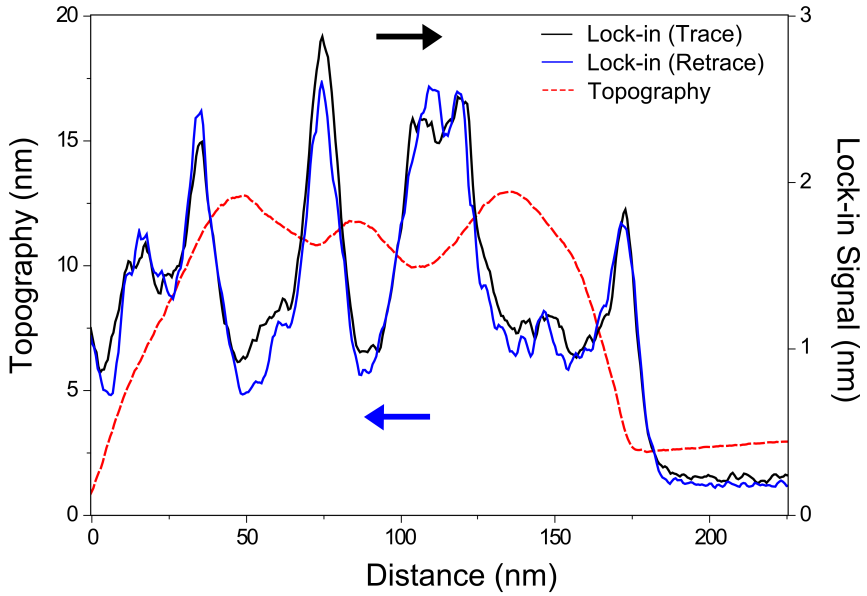

Figure 5.4: The topography profile (red dashed line) of an antimony nanoparticle shows variations in the topography slope. The single-frequency lock-in signal for a forward (trace) and backward (retrace) scan are similar and indicate a surface gradient induced shift of the free bending resonance frequency f_{res}.

Variations of local surface gradients of the particle topography causes shifts of the free bending resonance frequency f_{res} towards higher and lower frequencies [59]. Apart from an increased signal contribution on the right edge of the particle, it seems that the transition from a negative to a positive particle slope leads to an increased signal. A gradient induced frequency shift is a first explanation which causes signal variations of the lock-in and does not depend on the scanning direction. The frequency shift cannot be compensated by the single-frequency lock-in mode. Signal fluctuations in friction images occur and may give the impression of different friction interactions.
This example specifies limitations of the off-resonant modulation $f_{\mathrm{res}}/3$ and single-frequency lock-in technique regarding nanoparticles with heights of several nanometers.

5.2 Topography and Friction Image Sequence on an Antimony Nanoparticle

An antimony nanoparticle on HOPG is selected for further investigations of topography induced resonance shifts on particles. A single-frequency modulation is applied to the modulation piezo and the resonance amplitude $A(f_{\mathrm{res}})$ is extracted as third harmonic by the lock-in amplifier. The modulation frequency is stepwise increased in a range from 19 kHz to 21.5 kHz and a whole topography and friction image is monitored at each frequency step.
In Fig. 5.5, three images of the sequence are depicted which show the topography and lock-in signal with respect to different excitation frequencies. The friction signal on the

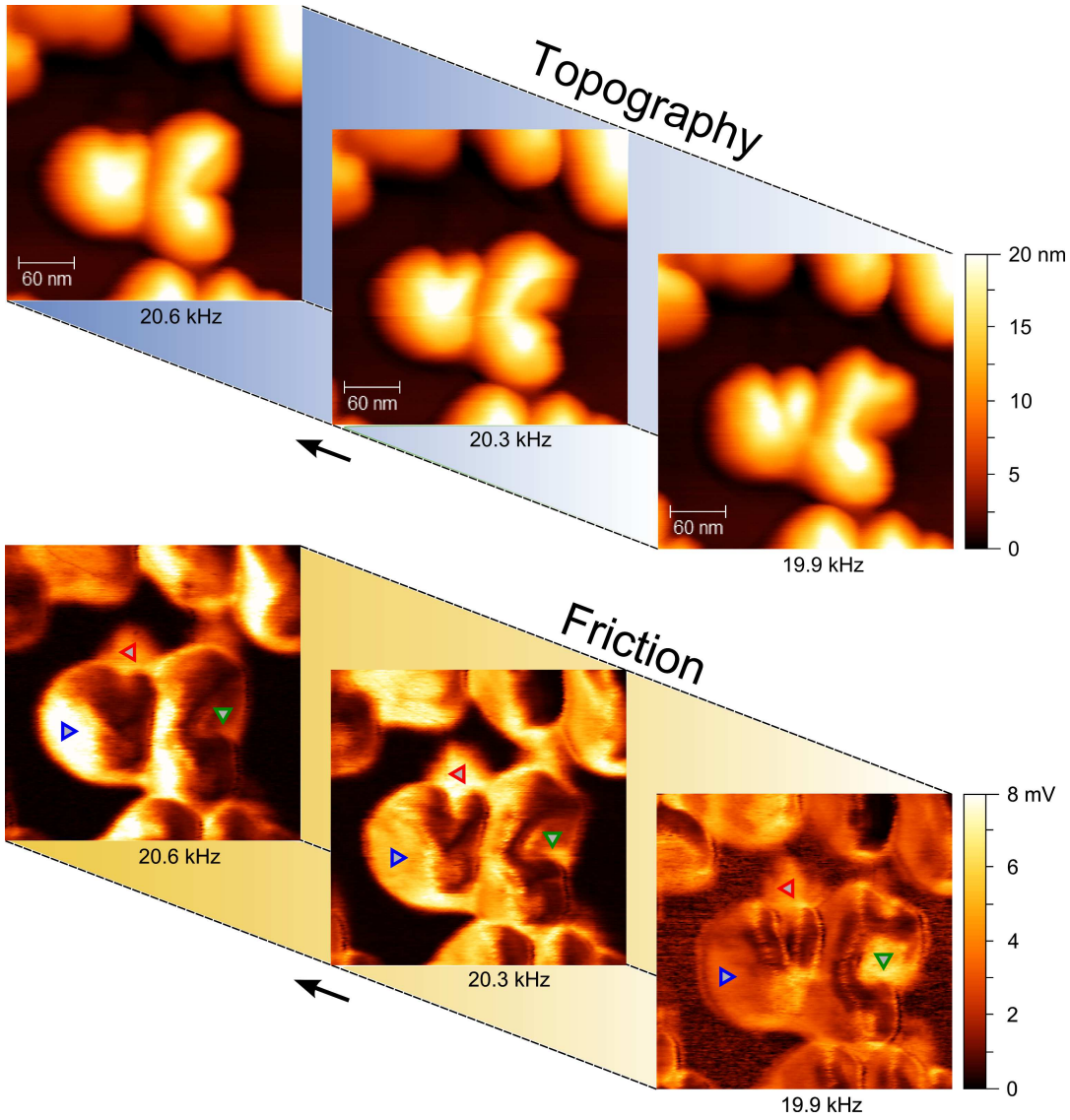

Figure 5.5: The figure depicts an excerpt of an image sequence on an antimony nanoparticle for three different modulation frequencies f_{mod}. The signal is extracted as third harmonic of the modulation frequency $A(f_{\mathrm{res}})$. (a) The shape of the particle in topography changes due to modulation induced abrasion. (b) Signal variations in the friction images are caused by variations of the topography and suggest a contrast dependence in friction images on the modulation frequency.

nanoparticle is dominated by contrast fluctuations. With increasing frequency, dark areas on the left side of the particle get brighter, whereas bright areas on the right side get darker. Furthermore, the underlying graphite surface contributes its maximum signal at a modulation frequency of 19.8 kHz.
Resonance signals $A(f_{\mathrm{res}})$ for different areas on the particle are extracted in Fig. 5.6. The blue mark depicts the lock-in signal for the left particle slope, the green mark corresponds with the signal on the right slope and the red mark shows the signal for antimony debris on the surface. In addition, a resonance curve of the graphite surface is extracted from the

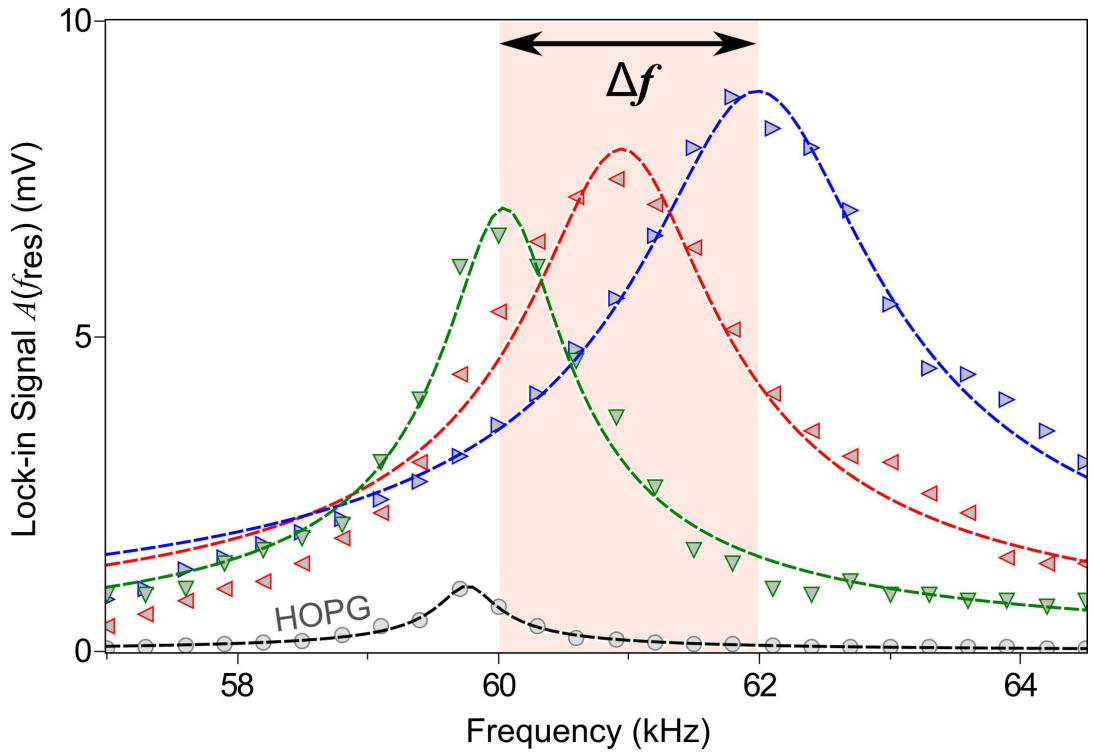

Figure 5.6: Resonance curves on antimony (green, red, blue) and HOPG (black) extracted from the image sequence in Fig.5.5. Topography induced resonance shifts cover a frequency range of about $\Delta f = 2$ kHz. The resonance frequency on HOPG is below the frequencies on antimony. The quality factor on antimony (red curve) is $Q_{\mathrm{Sb}} = 46$ and on HOPG $Q_{\mathrm{HOPG}} = 138$.

image series and reveal that the Q-factor on HOPG is increased compared to antimony factors.

Resonance curves exhibit that a maximum signal contribution on antimony varies in range of $\Delta f = 2$ kHz. Besides friction interactions between tip and sample, a contribution of the surface potential in Eq. 2.21 influences the resonance frequency f_{res} if an elasticity of the contact is not considered. This affects the effective spring constant k_{eff} [93]. The cantilever gets stiffer for a positive particle slope and less stiffer for a negative particle slope. By taking a lever spring constant of 175 N/m and frequency variations in an interval of 2 kHz into account, the effective spring constant can vary within a range of about ± 6 N/m during scanning a particle for a first estimation. With regard to the frequency on HOPG, greater variations of the effective spring constant are possible.

Extracting the resonance amplitude $A(f_{\mathrm{res}})$ at a fixed modulation frequency, differences in the signal are primarily caused by topography-induced frequency shifts of the resonance. Therefore, a single-frequency friction image depicts artificial signal variations caused by local surface gradients of the topography and does not represent the friction interaction between tip and sample entirely.

During monitoring the sequential images, the particle changes its shape and size. The interaction between a silicon cantilever tip and an antimony nanoparticle causes abrasion of the particle. The form of the particle changes towards a more spherical shape and the ablated volume is distributed over the surface.

5.3 Resonance Curves on Graphite and Antimony

The signal amplitude $A(f_{\mathrm{res}})$ on antimony is considerably higher in comparison to the signal amplitude on the underlying graphite surface, as can be seen in friction images. Series of frequency sweeps from 19 kHz to 21.5 kHz around $f_{\mathrm{res}}/3$ are conducted for an investigation of the non-linear signal coupling on graphite and on an antimony nanoparticle. The modulation amplitude A_{mod} is stepwise increased in a range of 0.5 nm to 5 nm for each sweep. The lock-in amplifier extracts the resonance amplitude around f_{res} in Fig. 5.7.

As a first interpretation, a non-linear interaction force between cantilever tip and antimony excites non-linear oscillations with a large resonance proportion $A(f_{\mathrm{res}})$, whereas on graphite the amount of the resonance amplitude is lower due to smaller interactions between tip and surface. Furthermore, the resonance amplitudes rise with increasing modulation amplitudes. In this case, the amount of energy which is transferred to the resonance oscillation increases with increasing modulation amplitude and results in higher resonance amplitudes $A(f_{\mathrm{res}})$.

The effective quality factors are taken from the resonance curves in Fig. 5.8 for each evaluable frequency sweep. The quality factors on graphite are greater and rise more quickly compared to the factors on antimony which indicates higher damping on antimony.

Moreover, the quality factors rise with increasing modulation amplitude. The modulation frequency has to match $f_{\mathrm{res}}/3$ more exactly to reach a synchronization between modulation and resonance oscillation and to excite the non-linear oscillation state with regard to increasing modulation amplitudes. This effect is obviously more important for contacts with lower damping where the quality of resonance curves rises faster.

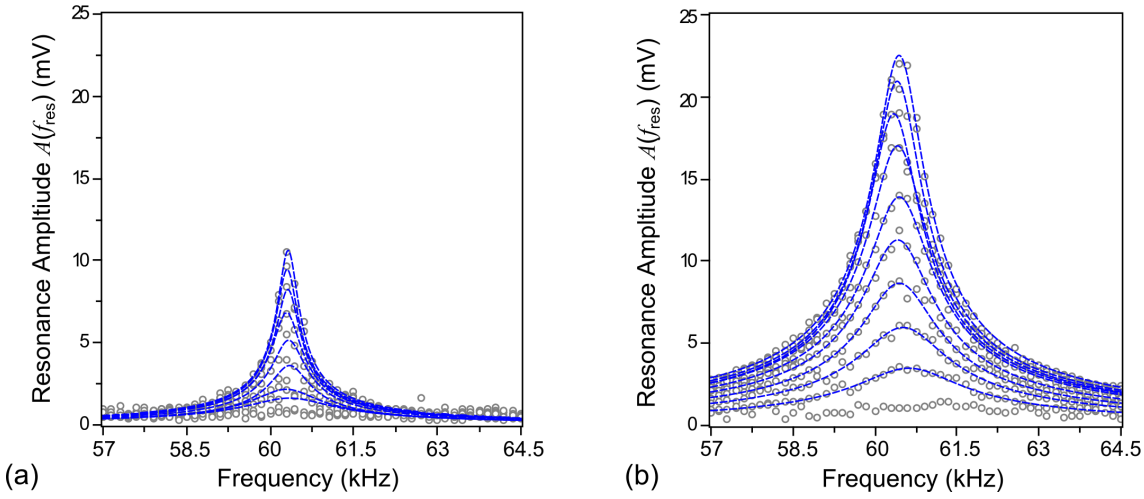

Figure 5.7: Series of single-frequency sweeps on HOPG (a) and on an antimony nanoparticle (b) with increasing modulation amplitude A_{mod} from 0.5 nm to 5 nm in 0.5 nm steps. The amplitude of the resonance curves rises with increasing modulation amplitude. The signal excitation, as well as the width of the resonance curves on antimony is greater than on HOPG.

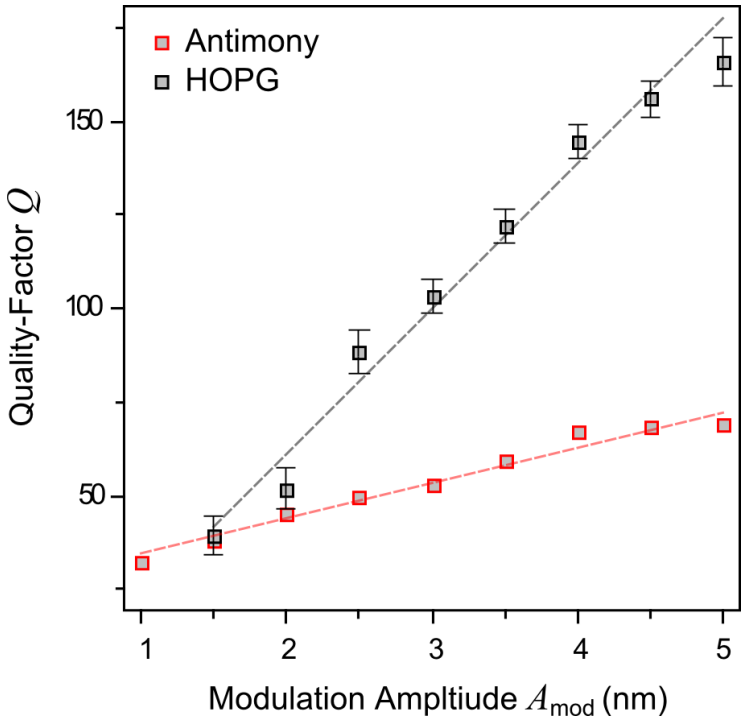

Figure 5.8: Effective quality factors on HOPG and antimony. The quality factors of the non-linear oscillations on HOPG, as well as on antimony increase with increasing modulation amplitude.

5.4 Single-Frequency Excitation and Band Excitation Method on Antimony

Topographical variations of nanoparticles have a strong impact on the lock-in signal of the single-frequency and off-resonant modulation technique as pointed out in the previous sections. In Fig. 5.9 (b), antimony nanoparticles were scanned with this technique (A_{mod} = 2.8 nm) and the friction image shows the mentioned contrast mechanism. On antimony the signal is increased, but strongly influenced by variations of local surface gradients.
The excitation signal of the band excitation method (Fig. 3.16) covers a whole frequency range in a required range Δf around the free resonance frequency f_{res} of the cantilever bending mode. The signal analysis of the oscillation response exhibits local resonance curves during scanning the surface. The excitation pulse in Fig. 5.9 (c) covers a frequency range from 18 kHz to 22 kHz with an amplitude of 2.5 nm. The maximum amplitudes $A(f_{\mathrm{res,\ max}})$ of each resonance curve are extracted for dynamic friction imaging.
The dynamic friction image shows nearly homogenous contrast on graphite and antimony. Contrarily to single-frequency excitations, the signal amplitudes $A(f_{\mathrm{res,\ max}})$ are lower compared to the single-frequency signal on the graphite surface. Obviously, the difference between both excitation signals affect the non-linear oscillation state of the bending mode on antimony and the used experimental parameters lead to a contrast inversion. In this case, increased stick parts due to higher friction interactions in the band excitation method on antimony prevent a distinct amount of resonance oscillations in the slip parts (compare Fig. 4.17). The excitation amplitude is not suitable to excite high resonance signals on

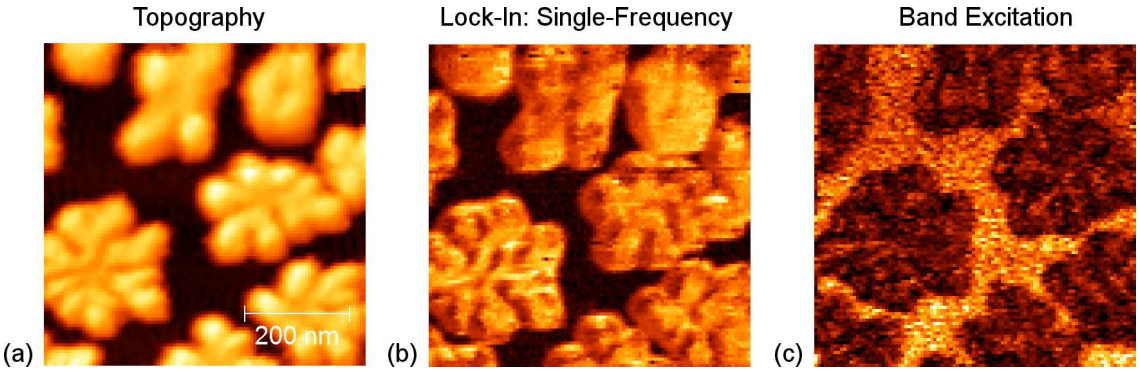

Figure 5.9: (a) Topography of antimony nanoparticles. Contrarily to single-frequency lock-in mode f_{res} (a), the amplitude of the band excitation (BE) method (c) on antimony is smaller compared to signal amplitudes on HOPG.

antimony and the signal on HOPG is clearly emphasized.
Moreover, in Fig. 5.10 (a, b) the frequency $f_{\mathrm{res,\,max}}$ of the signal is monitored during scanning and a rough estimation for the effective quality factor Q can be calculated

$$Q = \frac{f_{\mathrm{res,\,max}}}{\Delta f}, \tag{5.1}$$

where Δf represents the bandwidth of the curve. This approach is used to minimize computation times for the data analysis during scanning.
Frequencies $f_{\mathrm{res,\,max}}$ in Fig. 5.10 (a) are shifted towards higher values for positive particle slopes and shifted towards lower frequencies for negative particles slopes. This result clearly confirms that frequency shifts are caused by variations of local surface gradients.
A rough estimation of effective quality factors in Fig. 5.10 (b) furthermore confirms that the quality on graphite (i) $Q_{\mathrm{HOPG}} = 260$ is increased compared to the quality on antimony (ii) $Q_{\mathrm{Sb}} = 80$. In the next chapter, the fractional resonance excitation technique is applied to surface defects on the bare carbon model system HOPG for a systematic investigation of cantilever interactions at defects.

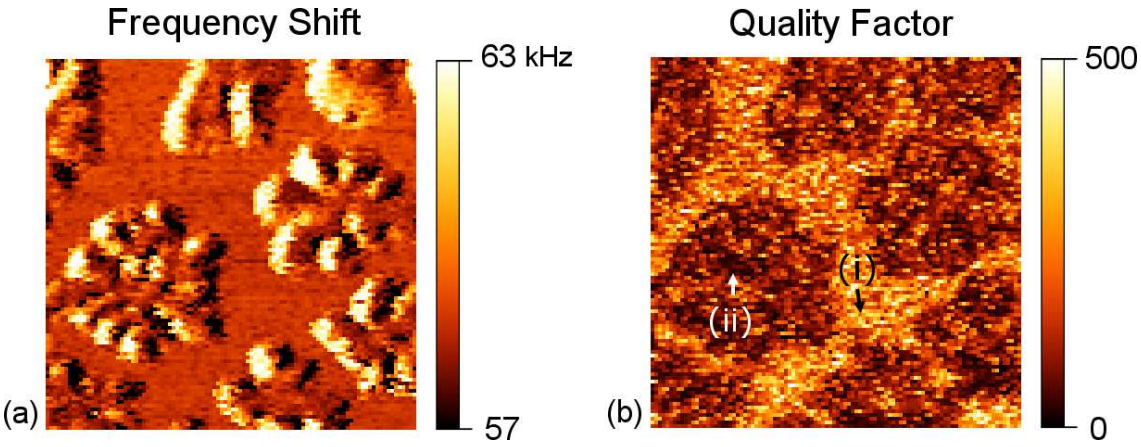

Figure 5.10: The band excitation (BE) method exhibits maps of frequency shifts (a) and effective quality factors (b) on nanoparticles (ii) and the underlying graphite surface (i).

5.5 Conclusion

Off-resonant excitations in dynamic friction force microscopy on antimony nanoparticles exhibit that the cantilever resonance response is strongly affected by the topography of the particles. Variations of surface gradients cause shifts of the resonance frequency f_{res} and lead to signal variations in friction images.
A friction image sequence reveals resonance curves on antimony and HOPG and exhibits that the maximum signal contribution on antimony varies in a range of $\Delta f = 2$ kHz. Besides friction interactions between tip and sample, a contribution of the surface gradient influences the resonance frequency f_{res} and affects the effective spring constant k_{eff}. A single-frequency friction image consequently depicts artificial signal variations caused by variations of local surface gradients in the topography and does not represent the friction interaction between tip and sample entirely.
The effective quality factors on graphite are higher and rise more quickly compared to the factors on antimony. This indicates that damping on antimony is increased compared to graphite whereas non-linear friction interactions are stronger between tip and substrate.
The band excitation method reveals resonance curves for each image pixel during scanning and the signal analysis depicts maps of maximum amplitudes $A(f_{\mathrm{res,\ max}})$, frequency shifts $f_{\mathrm{res,\ max}}$ and quality factors Q. Contrarily to single-frequency excitations, the band excitation amplitudes on antimony are lower compared to the underlying graphite surface. Frequency shifts with regard to different slopes on nanoparticles confirm that an off-resonant and single-frequency excitation is not entirely suitable to reproduce friction interactions on nanoparticles.

6 Dynamic FFM: Image Contrast of Graphite Surface Defects

Defect structures in carbon materials have a strong impact on their physical properties [94, 95, 96, 16]. Especially for the monolayer carbon material graphene those defects play an important role for the electrical conductivity and mechanical stiffness [97, 98, 99, 100, 101, 102, 103, 104]. For a detailed understanding of the influence of defects, however, it is important to analyze their exact structure and configuration. Here, dynamic friction force microscopy (dynamic FFM) is used to study surface defects on the carbon model system HOPG (highly oriented pyrolytic graphite).
Defects on graphite can occur in several different configurations [67]. For example surface steps are mainly caused by cleavage processes of topmost layers. [105]. Grain boundaries constitute another type of defect and occur at the intersections between different crystalline orientations. Line defects cause discoordinations of the atomic lattice and disrupt the crystal symmetry. Using scanning probe techniques, surface defects on an atomic scale have been investigated and reported in several studies [94, 95, 96, 16, 106, 105, 107]. Scanning tunneling microscopy (STM) has been used, for example, to resolve the superlattice structures of boundaries, describing the image contrast by Moiré patterns [95, 96].
Here, the image contrast of surface defects (steps and grain boundaries) in dynamic FFM is focused [12, 75, 73, 76, 74]. In this technique the tip is always in contact with the surface, while the sample position is modulated laterally at one third of the cantilever resonance. Non-linear frictional tip- sample interactions lead to an excitation of the cantilever eigenresonance. This resonance amplitude is recorded as the dynamic friction signal during scanning. It is found that the signal of the dynamic FFM technique gives direct access to frictional properties of surfaces and can resolve defects with very high sensitivity. Surface

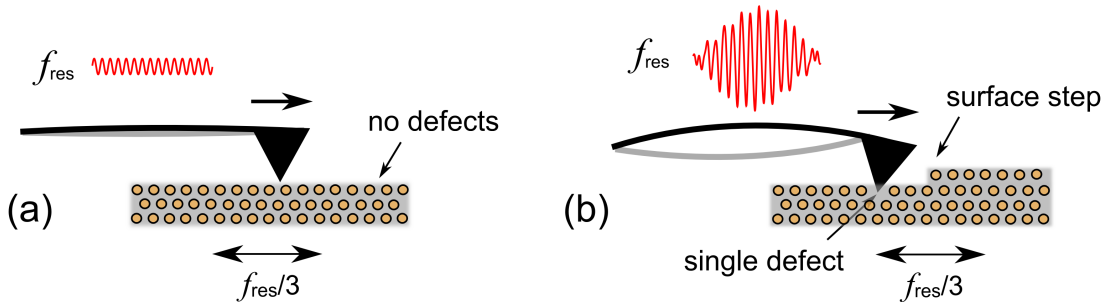

Figure 6.1: (a) The off-resonance modulation $f_{res}/3$ of a defect-free surface with low load leads to small interactions at the tip-sample contact and causes a small oscillation amplitude $A(f_{res})$ of lever bending oscillation. (b) Increased interaction forces at defects can lead to an increased resonance response $A(f_{res})$ and can cause a contrast mechanism in friction images.

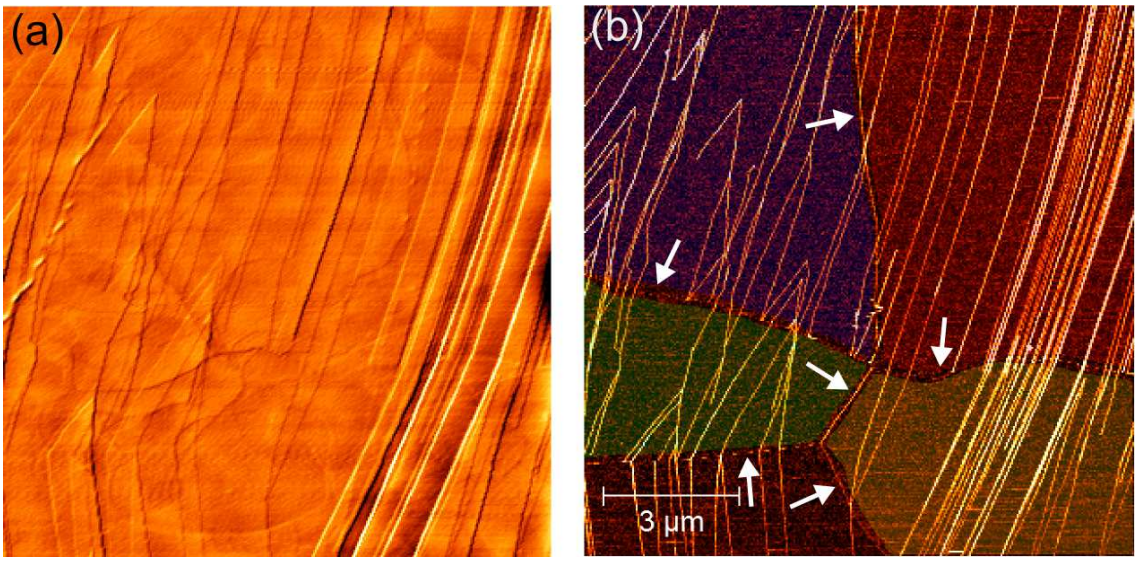

Figure 6.2: (a) High pass filtered and gradient shaded AFM image of the topography of an HOPG surface. (b) Simultaneously obtained dynamic friction image, i.e. the amplitude at $f_{\mathrm{res}} = 3 \cdot f_{\mathrm{mod}}$ from the lock-in amplifier, showing surface steps and grain boundaries (indicated by arrows). Graphite grains are highlighted in different colors. Image parameters were: $f_{\mathrm{mod}} = 20.02$ kHz, $A_{\mathrm{mod}} = 2$ nm.

steps as well as grain boundaries can be identified, and model simulations are presented which can explain the image contrast.
Further, a rapid band excitation scheme (frequency chirps) is used to obtain the complete resonance curves around the defects, revealing changes in the quality factor Q and resonance frequency f_{res} of the dynamic lever oscillations [59, 77, 60]. In particular, it is found that the elastic properties at step edges influence the image contrast in dynamic FFM.
The content of this chapter is submitted to a peer-reviewed journal (F. Mertens et al., "Dynamic friction force microscopy using fractional resonance excitation: Image contrast of graphite surface defects", (2015)).

6.1 Surface Steps and Grain Boundaries

An HOPG B-grade (mosaic spread: 0.8° - 1.2°) sample is used in experiments which provides a suitable model surface with a significant amount of surface defects and an averaged grain size of a few microns. The sample is cleaved with a scotch tape under ambient conditions and directly inserted in the load lock of the UHV system.
A fresh and sharp cantilever tip (PPP-Contr) is used and furthermore load forces are kept below 5 nN during measurements to avoid surface modifications.
In the following experiments two different types of excitation and detection schemes are applied. On the one hand, the sub-resonance single-frequency $f_{\mathrm{res}}/3$ excitation is applied to the sample while the cantilever oscillation signal at its resonance is detected by a lock-in amplifier (Fig. 3.15). The single frequency lock-in detection scheme performs signal analysis with a very high sensitivity, but has limitations in cases where the resonance

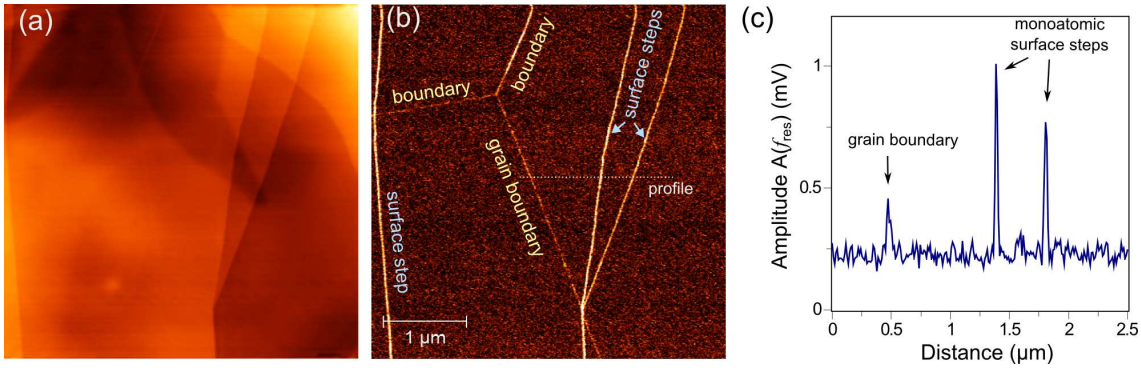

Figure 6.3: A zoom of Fig. 6.2 showing details of the topography. (b) The dynamic FFM image reveals a bi-atomic surface step (bottom center) which crosses a grain boundary and is split into two mono-atomic steps. The non-linear interactions between tip and surface defects cause an increased resonance signal $A(f_{\text{res}})$. (c) Line profile from (b) showing the dynamic FFM signal over a grain boundary and two subsequent steps.

frequency of the cantilever shifts due to the tip-sample interaction. Therefore, on the other hand, a band excitation (BE) method (Fig. 3.16) is used to analyze the cantilever response in the full frequency spectrum.

6.1.1 Graphite Surface Defects imaged by Dynamic FFM

First, the single frequency lock-in technique is used for imaging. The topography of a large area scan on HOPG shows a high occurrence of surface steps, as expected for the here used sample grade (Fig. 6.2 (a)). The simultaneously acquired dynamic friction image (Fig. 6.2 (b)) shows these step edges as bright lines. As outlined above the dynamic friction image represents the oscillation signal amplitude of the cantilever at its resonance frequency while the sample is laterally modulated at one third of the resonance frequency. The image contrast is therefore directly related to non-linear tip-sample interactions. Bright structures indicate areas with enhanced non-linear tip-sample interaction, as expected at step edges and surface defects. The modulation frequency f_{mod} was adjusted to obtain an optimized image contrast at the surface steps and defects. This was achieved by tuning the third harmonic signal response of the lock-in amplifier slightly off the resonance maximum observed in defect-free areas of the graphite surface.
Apart from an enhanced friction signal at the step edges, a network-like structure of less pronounced bright lines is visible. These are grain boundaries which are not visible in the topography. For better visibility, the corresponding grains are lightly colored in Fig. 6.2 (b). A closer inspection reveals that grain boundaries act as weak links during the cleavage process, where surface steps can arise or change their direction. A zoom into a surface area, where three grain boundaries converge into one point is shown in Fig. 6.3 (b). In the lower part of the image a double step is identified that splits two monoatomic steps at the position where a grain boundary crosses, a typical coincidence. A line profile of the dynamic FFM signal is shown in (c), passing one grain boundary and two surface steps. The signal amplitude across the grain boundary is clearly above noise level, but smaller than the contribution from the step edges.

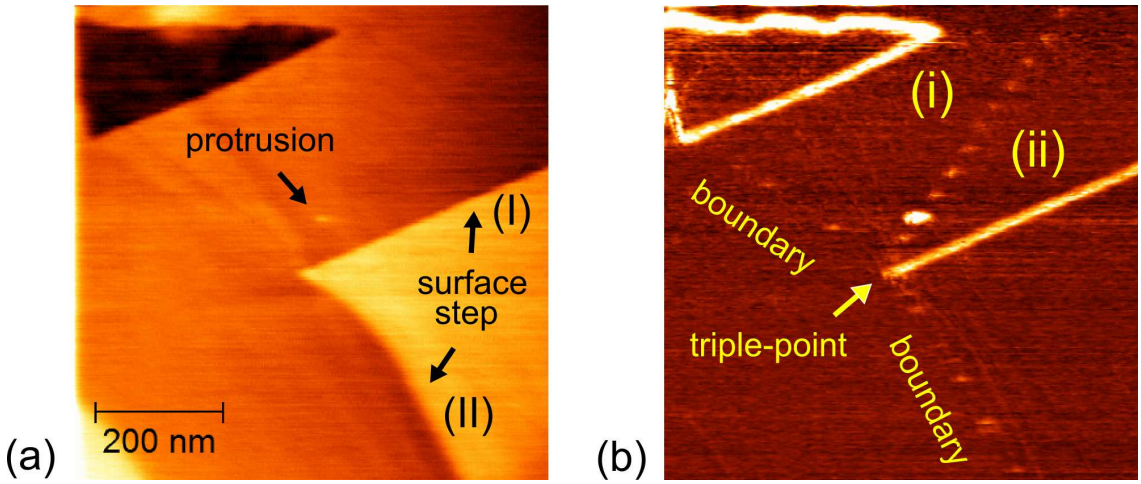

Figure 6.4: (a) Topography and (b) friction image on graphite, detected by using the fractional excitation technique. A small tilt angle between two rotated graphite grains (i) and (ii) forms a superlattice structure which is resolved with the AFM tip. Periodically distributed defects are revealed due to their increased frictional interaction. A protrusion provokes the highest friction contribution to the signal, whereas a topographical influence caused by other defects is not observed. Image parameters were: $f_{\mathrm{mod}} = 20.21$ kHz, $A_{\mathrm{mod}} = 7$ nm.

A comparison of topography and dynamic FFM images shows distinct differences. The topography image shows the surface steps on the top layer, as well as subsurface structures and steps in the graphite layers underneath. For example, a diagonally traversing step is clearly visible on the upper right corner and a darker area with lower topography is seen in the upper left corner. Those features are not seen in the dynamic FFM signal which is sensitive only to surface defects in the top layer. Furthermore, three grain boundaries converging into one point are clearly visible in the dynamic FFM signal in the upper left corner, which are not seen in the topography (except a faint signal of the upper center grain boundary).
This contrast formation indicates that dynamic friction images reveal surface defects with high sensitivity at low load. A low resonance signal $A(f_{\mathrm{res}})$ is excited on defect-free surface areas due to low non-linear interaction forces at the tip-sample contact ($\mathcal{N} > 1$ in Fig. 4.17). In contrast, at defects considerable increased non-linear interactions excite short resonance pulses which can be detected by the lock-in.

6.1.2 Small-Angle Tilt Grain Boundaries

A second example in Fig. 6.4 depicts grain boundaries which converge towards a point and additionally show a periodical superstructure. Again, the dynamic FFM signal in (b) clearly shows the grain boundary, while no corresponding contrast is seen in the topography image (a). Interestingly, within the periodic structure of the grain boundary in Fig. 6.4 (b) there is one local high signal contribution which is also observed in the topography Fig. 6.4 (a), whereas other defects cannot be recognized. One grain boundary extends across the surface from the middle of the image to the top right corner. It divides two grains with different lattice orientations labeled with (i) and (ii). The grain boundary

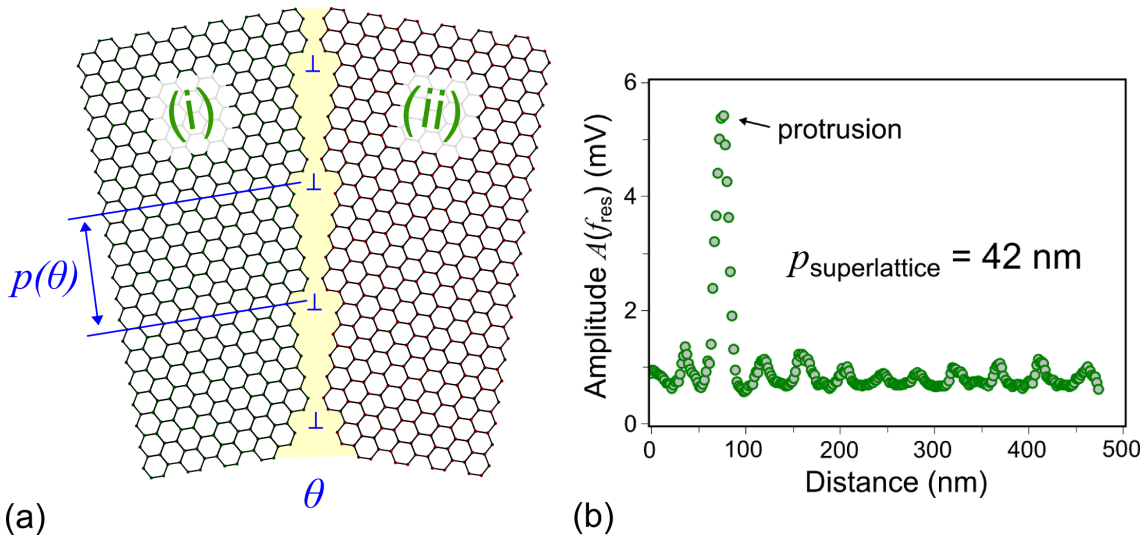

Figure 6.5: In a simple picture (c), the rotation angle θ between two grains (i) and(ii) determines the superlattice periodicity of tilt grain boundaries. A line profile (d) depicts the oscillation amplitude at defects with a periodicity of 42 nm.

shows an oscillating image contrast with a periodicity of about 42 nm (see line profile in Fig. 6.5 (b)). This is a superlattice structure which develops at the boundary between two grains with a very small tilt angle between different lattice orientations. Fig. 6.5 (a) graphically demonstrates the relation between tilt angle and periodicity $p_{\text{superlattice}}$ [95, 96]. The structure is described by a Moiré pattern [96] where distances between defects depend on the tilt angle θ

$$p_{\text{superlattice}} = \frac{b}{2 \cdot \sin(\theta/2)}. \tag{6.1}$$

The value b describes the Burgers vector which here is the lattice constant 0.246 nm of the graphite lattice [95].
With the periodicity of about $p_{\text{superlattice}} = 42$ nm and assuming a small-angle tilt grain boundary, Eq. 6.1 can be simplified and the tilt angle θ is found to be

$$\theta = \frac{b}{p_{\text{superlattice}}} = 0.34^\circ \tag{6.2}$$

Realistic contact sizes between tip and surface are in the range of several nanometers and only substructures of tilt-grain boundaries with very small tilt angels can be resolved in dynamic friction force microscopy [46].
In Fig. 6.6 the superlattice periodicity is depicted as a function of the tilt angle θ. For small angles a hyperbolic function describes the periodicity, where smaller angles lead to increasing distances between surface defects. Obviously, only substructures of tilt angle boundaries concerning angles approximately smaller than 1.5° can be resolved.
Another interesting feature of the dynamic FFM signal is found when comparing the two

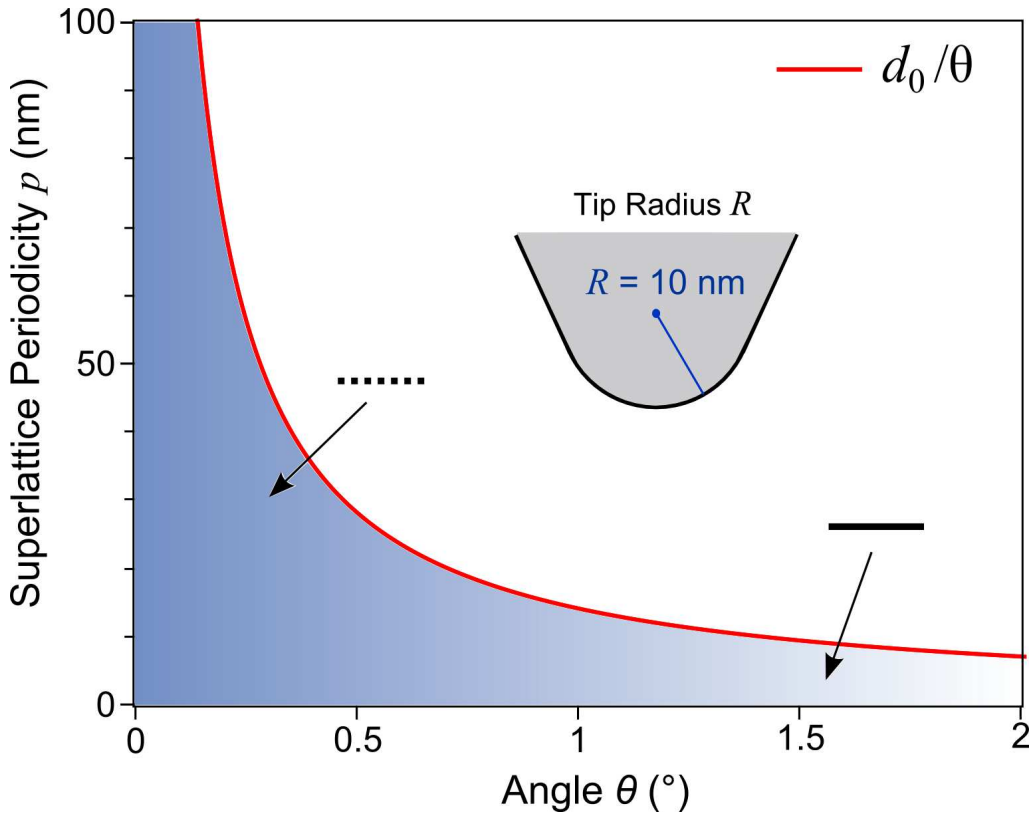

Figure 6.6: Schematic illustration for the detection of a superlattice periodicity with an AFM tip. The periodicity of the structure behaves hyperbolic (red line) concerning small tilt angles. The lower limit of structural resolution is limited by the tip radius and consequently only Moiré patterns caused by very small tilt angles can be resolved.

surface steps (I) and (II) which are found with the height of a monoatomic layer in the topography. Surface step (I) is located on top of the surface and contributes a noticeably signal to the dynamic FFM signal. In contrast, surface step (II) presumably runs beneath the topmost layer and does not noticeably affect the friction signal.
These examples typify that the dynamic FFM signal with the lock-in technique can give a very high signal sensitivity to subtle surface defects like grain boundaries, which are otherwise not or barely observed in the topography signal. However, at this point is unclear what gives rise to the different image contrasts for grain boundaries and steps. Therefore, the dynamic FFM image signal is simulated for several defect types based on an atomic friction model.

6.1.3 Lateral Interaction Forces at Surface Defects

An algorithm, presented by *Hölscher et al* [16] (Sec. 2.2.1), is used as starting point for calculations of dynamic interactions of a cantilever tip at surface defects.
In contrast to an undisturbed crystalline surface, the atomic surface coordination is altered and leads to variations in the interaction potential. Atoms from the first layer of a 2D-

crystalline structure are removed to simulate a step edge. At the position of the surface defect in Fig. 6.7 (a), an increased lateral surface potential results which is also referred to as Schwoebel-Ehrlich barrier [108, 109]. Furthermore, an example for a 3D-crystalline structure is depicted in Fig. 6.7 (b).
The variations in the surface potential at the position of a step edge can be used to simulate increased lateral forces during stick-slip movements of a cantilever tip in friction force microscopy experiments [16].
For a first approximation, a single atom is removed from the surface to simulate the lateral surface potential of a grain boundary in Fig. 6.7 (c, d). As in the case of a surface step, variations in the surface potential arise which lead to increased lateral interaction forces at the defect.
This approach is used to calculate the non-linear interaction of a cantilever tip at a surface defect during modulation. The cantilever tip experiences an increased lateral force during scanning over the defect due to distortions of the atomic lattice.

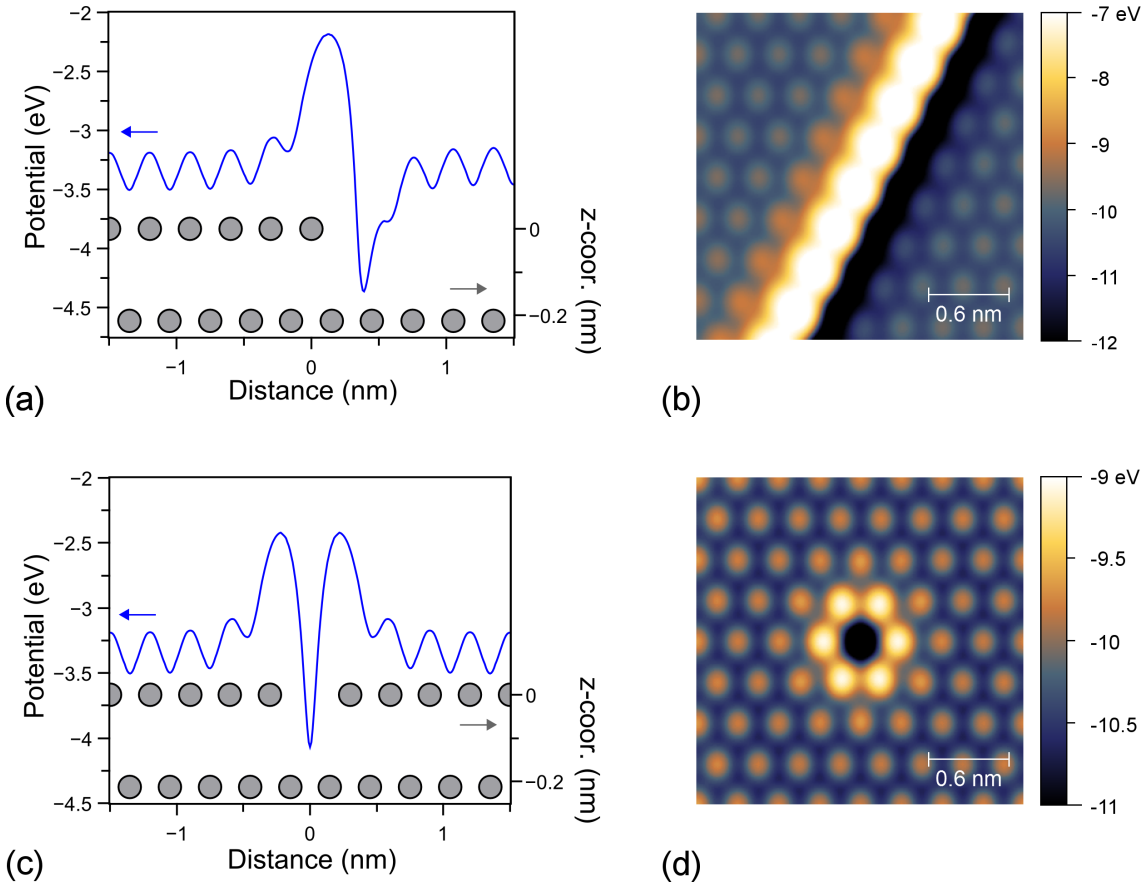

Figure 6.7: (a) Atoms of the first layer are removed to simulate a step edge on a surface. The lateral interaction potential is also known as Schwoebel-Ehrlich barrier and causes increased friction at surface steps. (b) Illustration of the potential barrier of a three-dimensional hexagonal crystal structure (hcp) with a lattice constant of 0.3 nm. (c) The potential barrier of a single-point surface defect and (c) the analogue illustration of the three-dimensional crystal structure.

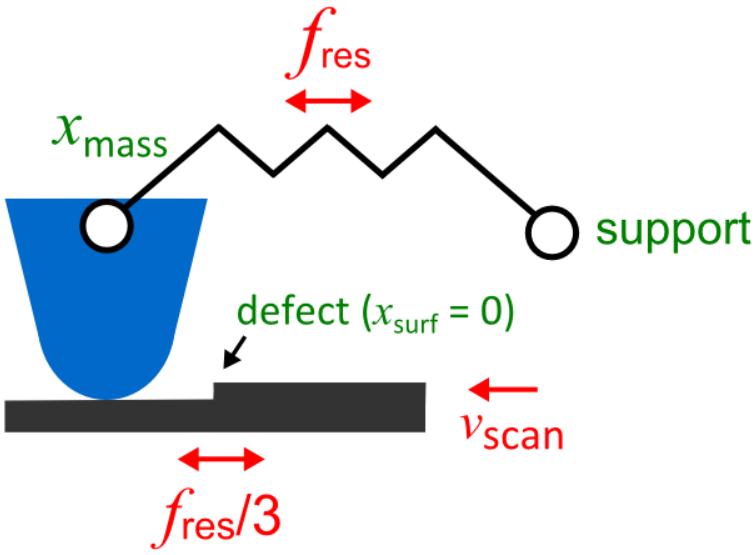

Figure 6.8: Basic model for simulations of non-linear interactions in dynamic friction frce microscopy at surface defects. The surface moves with a relative and constant velocity $v_{\text{scan}} = 1 \cdot 10^{-6}$ m/s, similar to experimental scanning speeds, and is additionally modulated at $f_{\text{res}}/3$. Non-linear interactions excite the mass which oscillates around its equilibrium position $x = 0$.

6.2 Simulations of Dynamic FFM Signal at Defects

For simulations of the dynamic FFM signal, the cantilever is represented by a spring-mass system (Fig. 6.8) [74]. The mass is connected with a spring and the surface vibrates at $f_{\text{res}}/3$. Spring constant $k_{\text{lever}} = 175$ N/m and mass $m = 1.23 \cdot 10^{-9}$ kg determine the resonance frequency $f_{\text{res}} = 60$ kHz of the system.
A constant longitudinal friction force F_{friction} affects the mass and induces non-linear resonant response [34, 74]. Furthermore, a viscous damping constant γ is taken into account [31]. With respect to the relative velocity $v_{\text{r}} = v_{\text{mass}} - v_{\text{surf}}$ between mass and surface, dissipative forces on a flat surface area without defects are given by

$$F_{\text{diss}} = -F_{\text{friction}} \cdot \text{sgn}\,(v_{\text{r}}) - \gamma \cdot v_{\text{r}}. \tag{6.3}$$

Please note that in contrast to conventional atomic stick-slip simulations, a stick-slip type motion of the tip is not assumed here, since the relative velocities are many orders of magnitude higher than in static FFM measurements. This assumption was verified by a direct comparison of experimental and similar simulations before (see Sec. 4.2). Also, the simulation does not differentiate between static and sliding friction contributions but resort to one friction value.
In the next step the surface defects are modeled, i.e. steps edges and grain boundaries F_{def}. As outlined before, the atomic coordination at the step edge is altered and causes variations in the atomic interaction potential with surface atoms which is also referred to

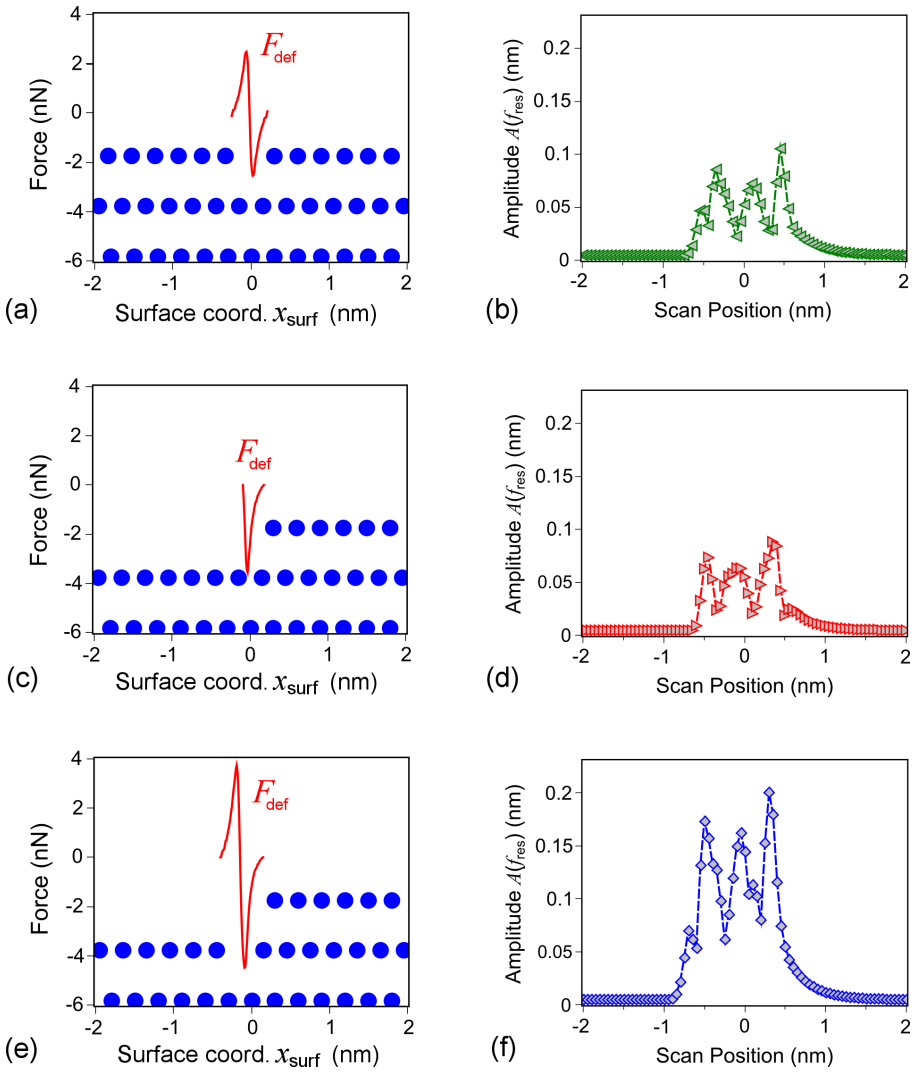

Figure 6.9: Forces at a grain boundary (a), step edge (c) and combined grain boundary/step edge defect (e). Simulated resonance signal (b, d, f) during scanning over the defects with a modulation amplitude of $A_{\mathrm{mod}} = 0.5$ nm. Dissipation on the surface is considered by $\gamma = 9 \cdot 10^{-6}$ Ns/m and $F_{\mathrm{friction}} = 0.04$ nN. Viscous damping is assumed to be increased at the defects $\gamma = 1.35 \cdot 10^{-5}$ Ns/m.

as Schwoebel-Ehrlich barrier [108, 109]. In atomic models of friction force microscopy it is usually assumed that one atom at the apex of the AFM tip interacts with the surface atoms [16]. In the spirit of that model, the lattice structure and algorithm presented before [16] are reproduced to calculate the effective energy barrier for surface defects.
In Fig. 6.9 (a),(c) and (e) the additional lateral force contributions F_{def} due to a missing atom defect, a monoatomic surface step and a combined atomic defect and step, respectively, are depicted. The missing atom defect is a simple 1D representation of a grain boundary and can be viewed as the maximum possible distortion of the atomic lattice due to dissimilar oriented grains at their mutual interface (i.e. emulating the atomic lattice at the position of the $\perp$-symbols in Fig. 6.5 (a)). For model simulations, the atomic defect

potential is matched with the average friction approach in Eq. 6.3. In a first approximation, for a qualitative interpretation, the lateral defect force F_{def} (red curves in Fig. 6.9 (a),(c) and (e)) is taken which is then assumed to be encountered by the laterally moving tip at the position of the defect. The spring force and the frictional forces are summed for simulations

$$m \cdot \ddot{x}_{\mathrm{mass}} = -x_{\mathrm{mass}} \cdot k_{\mathrm{lever}} + F_{\mathrm{def}} + F_{\mathrm{diss}}. \tag{6.4}$$

In order to mimic the dynamic FFM method, the surface is simulated to vibrate laterally at $f_{\mathrm{mod}} = f_{\mathrm{res}}/3$ and induces tip oscillations, i.e. position x_{mass} of the mass m around its equilibrium position at $x = 0$, which are calculated by a numerical algorithm. In this method the tip motion v_{scan} is coupled to the surface oscillation by the frictional forces in Eq. 6.3 and F_{def}. Interaction forces between mass and surface are calculated with respect to the interaction coordinate

$$x_{\mathrm{i}} = x_{\mathrm{mass}} - x_{\mathrm{surf}}. \tag{6.5}$$

In Fig. 6.9 (b, d, f) the resonance component $A(f_{\mathrm{res}})$ of the tip oscillation, taken from a fast Fourier transformation, is shown for the three defect types. Each data point represents an averaged amplitude with regard to one modulation period at $f_{\mathrm{res}}/3$. Small dissipative friction forces F_{diss} between tip and surface cause a low signal. If the mass encounters a surface defect, non-linear interactions at the defect barrier increase the resonance oscillations of the mass. Furthermore, an increased viscous damping parameter with respect to the flat surface is used at the position of the defect, to account for the enhanced damping properties of defective graphite layers.
The simulated data qualitatively confirms that the here considered surface defects result in an enhanced amplitude at the cantilever resonance as observed in the experiments in Fig. 6.3 (b). The simulated resonance amplitude values for the atomic defect and the monoatomic step are of similar magnitude, while the experiments show a factor of about three larger amplitudes for the step as opposed to the grain boundary. However, the here simulated missing atom defect can be considered as the maximum defect geometry along a grain boundary and on average a smaller signal should be seen, consistent with the experiments.
However, close observation of the simulated amplitude data reveals a substructure in the signal, e.g. three distinct peaks along a step edge which is not seen in the line profiles of the experimental data in Fig. 6.3 (c). In order to resolve this substructure in the experiments, a measurement of the topography and dynamic FFM signal (Fig. 6.10) with enhanced lateral resolution and optimized modulation amplitude, as well as frequency is done on an area with a step edge (left hand side) and combined grain boundary/step edge (right hand side). In the latter a grain boundary crosses a monoatomic step edge on the right part of the image.
The images already indicate that a sub-structure exists in the amplitude signal along the surface steps. One representative line profile of the cantilever resonance amplitude on the step-edge on the left hand side is shown in Fig. 6.10 (c) and two line profiles along the grain boundary/step edge on the right hand side in Fig. 6.10 (d) and (e).

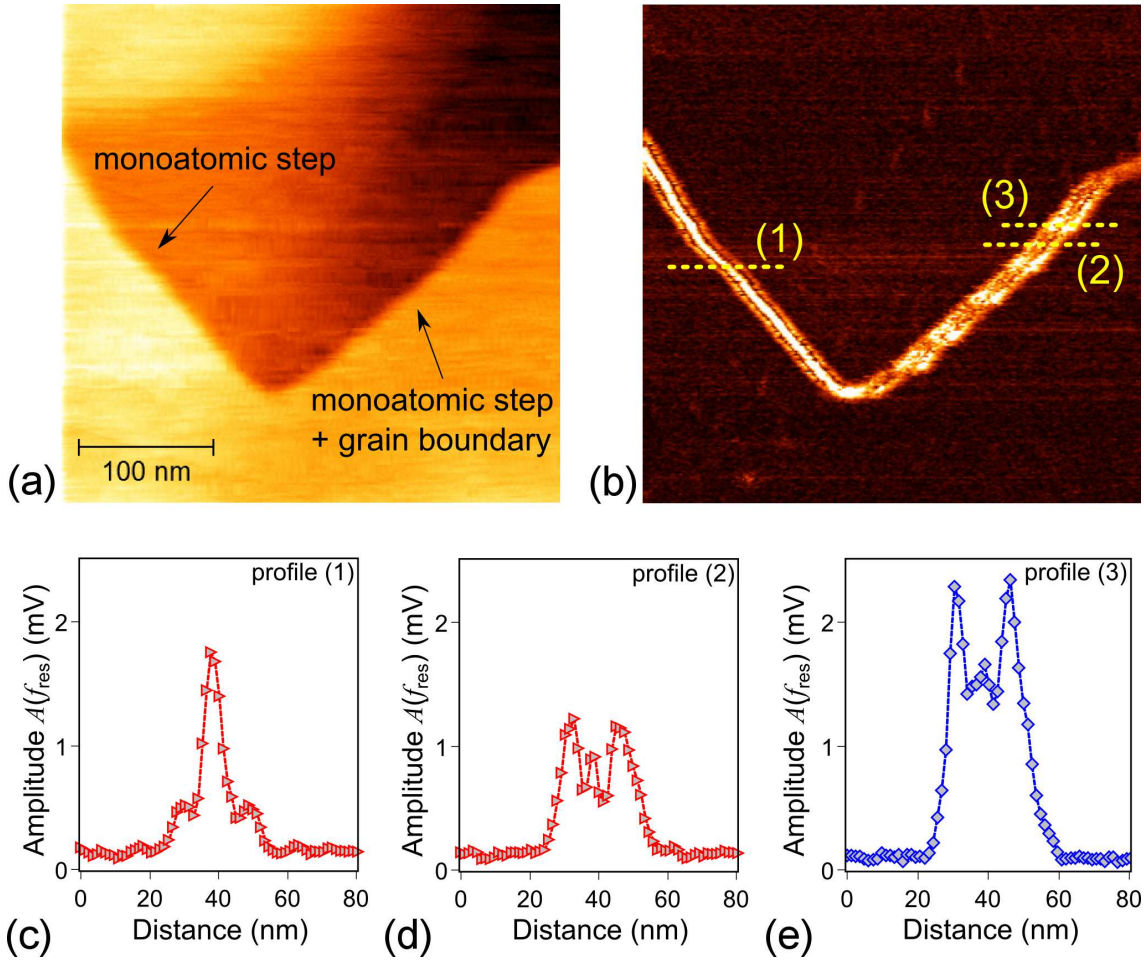

Figure 6.10: (a) The topography depicts a monoatomic surface step which is crossed by a grain boundary on the right part of the image. (b) The dynamic FFM channel shows an increased signal at the step edges ($f_{\mathrm{mod}} = 20.2$ kHz). (c - e) Line profiles of the dynamic friction signal at the indicated positions 1 and 2 (monoatomic step edge) and 3 (grain boundary plus step edge) show a distinct fine structure along the defects.

The step edge on the left hand side (Fig. 6.10 (c)) shows a three peak substructure in the amplitude signal, similar to the simulation in Fig. 6.9 (d). In the experiment the middle peak, however, is much more pronounced than the side peaks, which is different from the simulations. For the combined grain boundary/step edge in Fig. 6.10 (d, e) a triple peak structures is found, in good agreement with the simulations. Depending on the exact position of the tip along the defect, the height of the peaks alternates a fingerprint of the above discussed Moiré pattern of the grain boundary.
Please note that the horizontal axis in the experimental line profiles and the simulations encompass very different ranges. For example the distance between the two outer peaks for the monoatomic step edge in the experiment (Fig. 6.10 (d)) is about 15 nm, while the corresponding distance in the simulated amplitude graph (Fig. 6.9 (d)) is 1 nm. This is due to the different lateral oscillation amplitudes used in the experiment and the simulation of 7 nm and 0.5 nm, respectively. The ratio between peak distances and oscillation

amplitudes are about 15 in both cases, showing that the sub-structure range is directly related to the sample modulation amplitude.
While there is no attempt to explain the physical reason for the precise fine structure at this point, the model qualitatively explains the experiments and the observed enhanced dynamic FFM signal at defects and steps. A direct quantitative comparison is difficult due to certain unknown parameters, like contact stiffness, tip shape and viscous damping factor. Moreover, the force interaction between tip and surface may also result in a shift of the effective cantilever resonance which is completely neglected so far. Since a fixed frequency $f_{\mathrm{mod}} = f_{\mathrm{res}}/3$ is excited and the cantilever amplitude is also read out at a fixed frequency f_{res}, a resonance shift may change the cantilever amplitude signal substantially, and consequently influence the precise fine structure of the signal.
Therefore, in the next step, measurements of the cantilever amplitude signal are performed along a step edge as a function of the excitation frequency. Since a complete frequency sweep at each tip-sample position would be too time consuming and drift effects would dominate, a rapid band excitation method is implemented in the following.

6.3 Dynamic Friction Signal using the Band Excitation Method

In order to implement a fast frequency dependent analysis of the cantilever amplitude behavior, an off-resonant chirp signal is applied to the modulation piezo during scanning. A frequency range from 20.0 - 20.6 kHz around the $f_{\mathrm{res}}/3$ of the bending mode was used. In

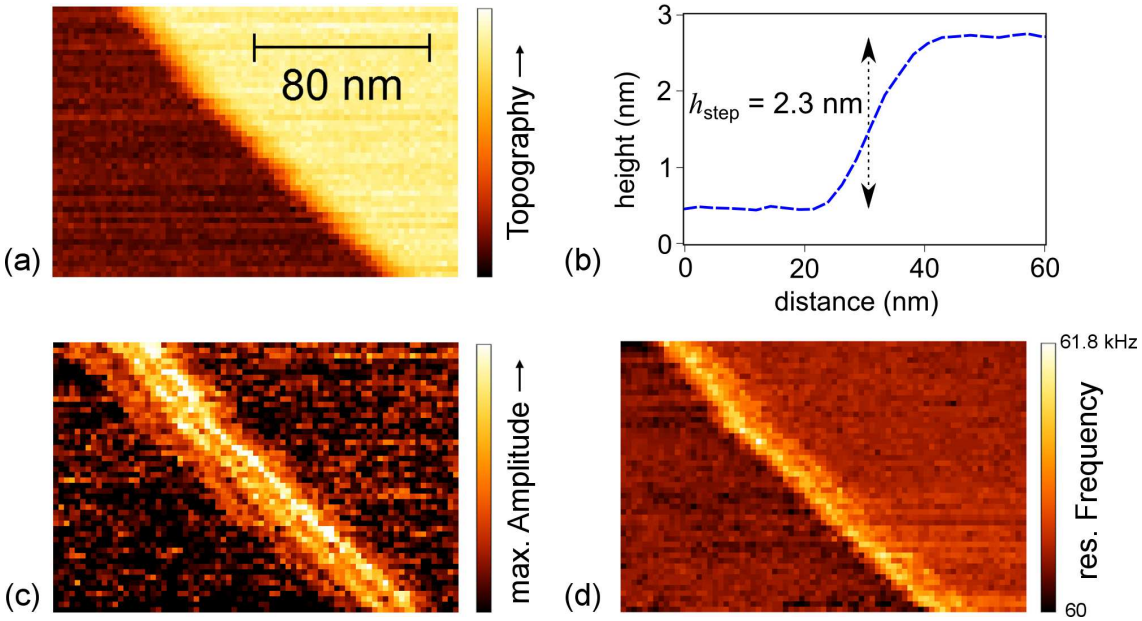

Figure 6.11: Off-resonant chirp excitation at a graphite surface step. The profile of the topography indicates a step height of 2.3 nm (a, b). Each pixel in the amplitude and frequency image represents a single resonance measurement (c, d). The maximum amplitude (c) exhibits a higher signal at the surface step. Additionally, the interaction causes a slight shift towards higher frequencies (d).

the following measurements, the excitation amplitude was kept constant at 1.5 nm, except at the band edges to avoid artificial peaks (see also Fig. 3.16) [45]. The digital signal processing and fast Fourier transformation of the resonant cantilever response obtains a complete resonance curve at each image pixel. The characteristic parameters of the resonance curves, i.e. quality factor, resonance frequency and amplitude, can be extracted and used for mapping the local dynamic friction induced tip-sample interaction.
The topography of a multiple surface step with a height of 2.3 nm is depicted in Fig. 6.11 (a) and (b). Again, an increased amplitude signal with a threefold sub-structure is seen along the step edge in Fig. 6.11 (c). However, a considerable shift of the cantilever resonance towards higher frequencies along the step edge is observed in Fig. 6.11 (d). This means that the amplitude signal in the previous dynamic FFM measurements using a fixed excitation and read-out frequency is indeed a convolution of amplitude changes, as well as frequency shift effects.
For better analysis, the averaged resonance curves of the cantilever on the bare graphite surface, as well as at the step edge are depicted in Fig. 6.12. The quality factor at the step edge is reduced by a factor of 4.5 and confirms a higher damping factor at the step. Furthermore, the resonance frequency is shifted by $\Delta f_{\text{shift}} = 0.29$ kHz towards higher frequencies.
Again simulations with the spring-mass system (Fig. 6.14) are performed in order to understand the local resonance curves on the surface and at the step edge. In contrast to the

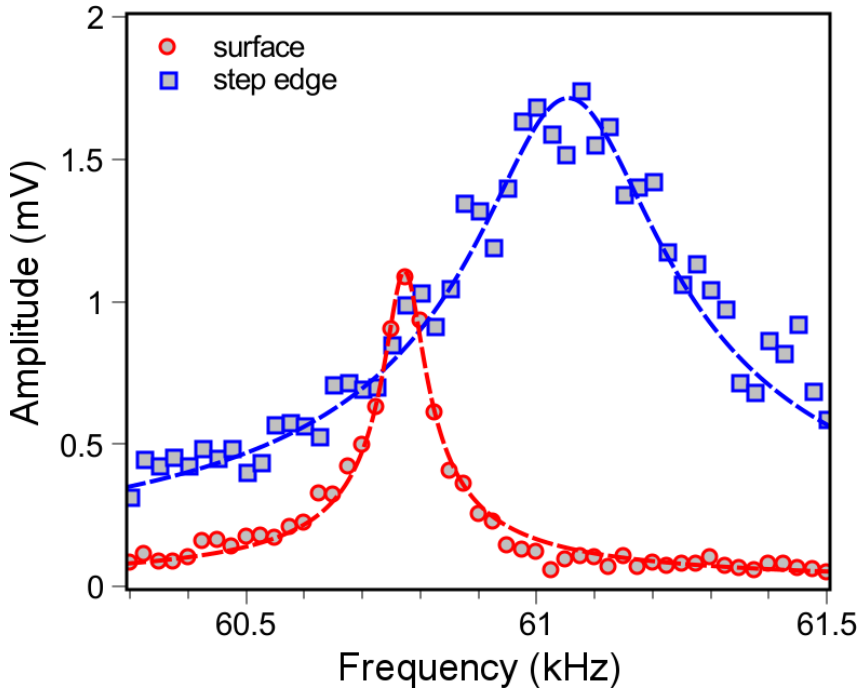

Figure 6.12: Experimental resonance curves on a graphite surface (red) and at a surface step (blue). The off-resonant excitation frequency is swept over a frequency band around $f_{\text{res}}/3$. The oscillation amplitude is increased at the surface step and the resonance frequency is shifted towards a higher frequency. Furthermore, higher dissipation at the step is accompanied by a decreased quality factor $Q = 195$ in comparison to the quality on graphite $Q = 879$.

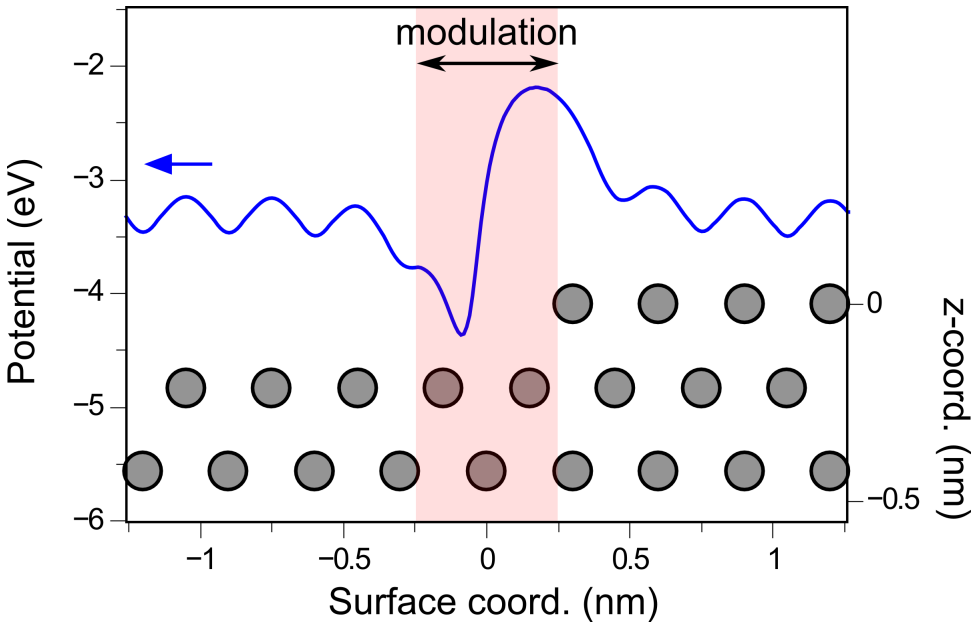

Figure 6.13: The frictional barrier of a monoatomic surface step affects the interaction between tip and surface at the defect. This variation in the surface potential causes an increased lateral force (compare Fig. 6.9 (d)) which influences the non-linear interaction during modulation and leads to an increased oscillation amplitude.

previous simulations, now for each data point in Fig. 6.14 (c), the surface is modulated by a fixed off-resonant frequency and amplitude. The third harmonic amplitude of the mass oscillation is extracted by performing a fast Fourier transformation. This obtains the complete cantilever resonance curves in the frequency domain.
Three simulated curves are depicted in Fig. 6.14 which illustrate the amplitude response on the surface and at the step edge around the cantilever resonance frequency f_{res}. The interaction on the surface is described by an adequate dissipative force resulting in a small resonance amplitude (red curve). At the step, the frictional barrier of a monoatomic surface step (lateral potential is shown in Fig. 6.13) is used. The corresponding curve (light blue square markers) shows an increased amplitude but decreased quality factor Q by a factor of 5.8, similar to the experimental data.
However, a striking discrepancy between experiment and simulation is observed for the frequency shift of the resonance curve. While the experiment shows a shift of the cantilever resonance to higher frequencies, the simulation predicts an opposite shift to lower frequencies. Please note that the relative amplitudes, the Q-factors and frequency shift magnitude depend on the chosen simulation parameters, however, the negative frequency shift direction is fixed, and cannot be changed to become positive within a meaningful range of parameters. Therefore, it is concluded that conceptually one important parameter is missing in the simulation.
In the next step, a modified interaction is used in the simulation by adding an elastic response of the step edge (see Fig. 6.14). The resonance frequency f_{res} of the bending mode is determined by the spring constant of the cantilever k_{lever} in Fig. 6.14 (a). A virtual

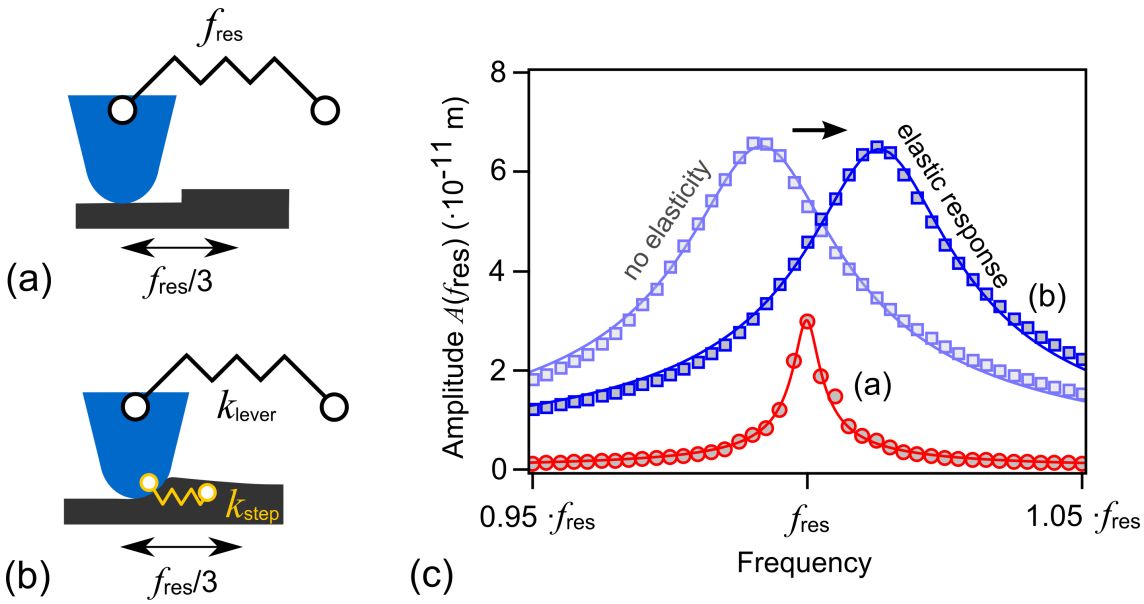

Figure 6.14: (a) The cantilever is represented by a spring-mass system for simulations. (b) Step edges cause higher interactions and in addition an elastic deformation provokes an increased resonance frequency f_{res}. (c) Simulated single-frequency amplitude response caused by a modulation amplitude $A_{mod} = 0.25$ nm at $f_{res}/3$. Friction on the surface is described by $\gamma = 1.35 \cdot 10^{-6}$ Ns/m and $F_{friction} = 0.05$ nN. At the step edge $F_{friction} = 0.05$ nN, increased damping $\gamma = 1.35 \cdot 10^{-5}$ Ns/m, the step edge defect barrier and a spring constant $k_{step} = 7.5$ N/m affect the mass.

spring constant k_{step} couples parallel to the cantilever in Fig. 6.14 (b) which represents an elasticity of the step and results in a higher effective spring constant k_{eff} of the system

$$k_{eff} = k_{lever} + k_{step}. \tag{6.6}$$

Now the elastic response of the step edge causes a resonance shift towards higher frequencies (see dark blue markers in Fig. 6.14 (c)) in qualitative agreement with the experimental observation.

6.4 Conclusion

In conclusion, surface defects on graphite (HOPG) using fractional resonance excitation in dynamic friction force microscopy were analyzed. The dynamic friction images do not only show surface steps but also reveal grain boundaries which are not visible in the topography. Corresponding simulations show that the dynamic friction signal from grain boundaries is of similar magnitude as from step edges, giving a qualitative insight into image contrast mechanisms. A fine-structure in the friction signal along defects and step edges can be identified which also shows up in the simulations. A quantitative comparison between simulation and experiments remains difficult due to several unknown parameters in the tip-sample contact.

The band-excitation method is adapted to the experimental setup for a more detailed investigation of friction interaction at a step edge. Experimental and simulated resonance curves indicate, that a decreased quality factor Q at the defect results due to increased energy dissipation when the tip crosses the step edge. Further, elastic properties of the topmost layer are found which can have a strong impact on the resonance curve signal and must be considered for the interpretation of the dynamic FFM images. The elasticity of mono- to multilayer graphene sheets has been shown to influence conventional FFM imaging already [110]. The method of fractional resonance excitation dynamic FFM seems to be very sensitive to those surface elasticities.

7 Summary

In conclusion, a fractional resonance excitation technique in dynamic friction force microscopy is introduced which can map local friction with high sensitivity.
A lateral sample modulation in the direction of a cantilever long-axis, with an excitation frequency below the natural eigenfrequency of the cantilever beam $f_{\mathrm{mod}} < f_{\mathrm{res}}$, excites dynamic oscillations of the bending mode. Frictional interactions at the tip-sample contact induce lever beam resonance oscillations at f_{res} which can be extracted by a lock-in detection scheme. In addition, normal deflections of the cantilever due to a comparatively slow scanning movement of the tip are controlled by a feedback loop and reflect the topography of the sample surface.
The cantilever beam vibrates in resonance if the modulation frequency matches an integer fraction of the bending mode resonance $f_{\mathrm{mod}} = f_{\mathrm{res}}/n$ with $n = 1, ..., 5$ (fractional excitation frequencies). The highest signal-to-noise ratio is reached at one third of the resonance $f_{\mathrm{mod}} = f_{\mathrm{res}}/3$.
A phenomenological model based on a spring-mass system is developed for a detailed analysis of the non-linear oscillation state. A constant friction value F_{friction} provokes stick-slip interactions between tip and surface. The friction force adheres the tip to the surface during the stick parts, where the cantilever oscillates at the modulation frequency. In contrast, if the lever spring force overcomes the acting friction force the tip starts to slide over the surface and the cantilever beam partially oscillates at resonance f_{res}.
The non-linear tip sliding mechanism sets in as soon as the excitation amplitude exceeds a certain threshold A_{trans}. For small modulation amplitudes a linear response results, where the cantilever tip sticks to the surface and directly follows the modulation movement. With an increasing modulation amplitude the transition from static-to-sliding is reached and the tip starts to slide across the surface.
At the transition point, the arising resonance frequency component $A(f_{\mathrm{res}})$ in the non-linear cantilever response can be extracted by a lock-in amplifier. A feedback setup is developed which can control the modulation amplitude at the stick-to-slip transition. Different lattice orientations of graphite grains influence the image contrast which can be explained by the graphite flake scenario. Frictional aging during sticking of the tip can be neglected due to very short hold times.
The topography of antimony nanoparticles influences the resonance frequency f_{res} of the dynamic cantilever oscillation. A single-frequency f_{res} friction image consequently depicts artificial signal variations caused by variations of local surface gradients. The images represent frequency shifts due to variations of the particle topography.
Furthermore, surface defects on graphite using fractional resonance excitation have been analyzed. The dynamic friction images do not only show surface steps but also reveal grain boundaries which are not visible in the topography. Corresponding simulations show that the dynamic friction signal from grain boundaries is of similar magnitude as from step edges, providing a qualitative insight into image contrast mechanisms. A fine-structure

in the friction signal along defects and step edges is identified which also appears in the simulations.
A band-excitation method is adapted to the setup for a more detailed investigation of friction interaction at a step edge. Experimental and simulated resonance curves indicate that a decreased quality factor Q at defects results due to increased energy dissipation when the tip crosses the step edge. Further, elastic properties of the topmost layer can have a strong impact on the resonance curve signal and must be considered for the interpretation of the dynamic FFM images.

Appendix

Basic Spring-Mass Model for Simulations

The cantilever is represented by a spring-mass system with a predefined resonance frequency f_{res} for simulations

$$f_{\mathrm{res}} = \frac{1}{2\pi} \cdot \sqrt{\frac{k_{\mathrm{spring}}}{m}}. \tag{7.1}$$

Scripts for computer simulations are realized in the programming language *phyton* where motion sequences are realized within short time steps Δt.
Starting at a given time t, mass position x_{mass} and velocity v_{mass} during modulation with a frequency $f_{\mathrm{res}}/3$ and modulation amplitude A_{mod} are well-defined

$$x_{\mathrm{surf}} = A_{\mathrm{mod}} \cdot \sin(2\pi f_{\mathrm{res}}/3 \cdot t), \tag{7.2}$$

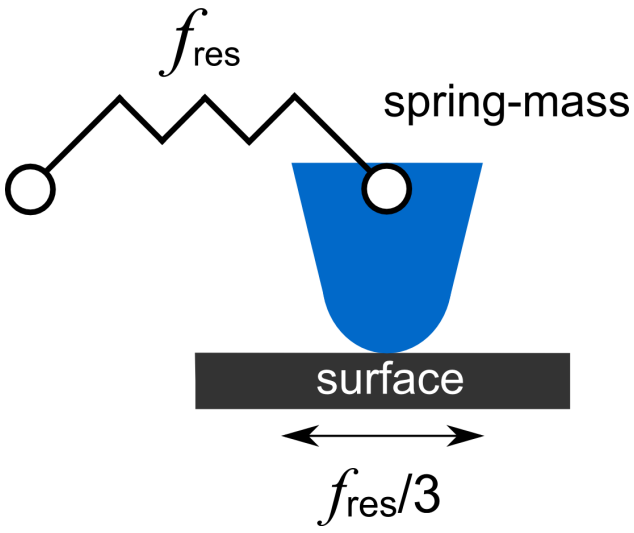

Figure 7.1: A spring-mass system is placed on top of a vibrating surface. The system is fixed to a support and spring constant, as well as mass determine the resonance frequency f_{res}. Spring force and friction interaction at the tip-surface contact accelerate the mass. The resulting oscillation response depends on frictional properties and the movement state of the surface.

$$v_{\text{surf}} = \mathrm{d}x_{\text{surf}}/\mathrm{d}t. \tag{7.3}$$

Furthermore, mass position x_{mass} and velocity v_{mass} are determined for a given time t. A restoring spring force acts on the mass depending on its deflection from the equilibrium position $x = 0$

$$F_{\text{spring}} = -k_{\text{spring}} \cdot x_{\text{mass}}. \tag{7.4}$$

Frictional interaction forces between mass and surface couple the mass oscillation to the surface oscillation. The relative velocity between mass and surface $v_{\text{r}} = v_{\text{mass}} - v_{\text{surf}}$ determines the direction of a constant friction force F_{friction}

$$F_{\text{const.}} = -F_{\text{friction}} \cdot \text{sgn}(v_{\text{r}}), \tag{7.5}$$

and describes viscous damping γ

$$F_{\text{viscous}} = -\gamma \cdot v_{\text{r}}. \tag{7.6}$$

A half-step method is used for an integration of Newton's equation of motion and calculates the mass oscillation. A detailed description of the Euler-Richardson method is given by *Gatland* [83].
This method calculates half-step points for $t + \Delta t/2$. The total force accelerates the mass and half-step velocity and position can be calculated

$$a_{\text{mass}} = (F_{\text{spring}} + F_{\text{const.}} + F_{\text{viscous}})/m, \tag{7.7}$$
$$v'_{\text{mass}} = v_{\text{mass}} + a_{\text{mass}} \cdot \Delta t/2, \tag{7.8}$$
$$x'_{\text{mass}} = x_{\text{mass}} + v_{\text{mass}} \cdot \Delta t/2. \tag{7.9}$$

For $t + \Delta t/2$, all relevant half-step parameters of mass and surface are recalculated

$$a'_{\text{mass}} = (F'_{\text{spring}} + F'_{\text{const.}} + F'_{\text{viscous}})/m. \tag{7.10}$$

The half-step acceleration and velocity are used to calculate the new parameters

$$v_{\text{mass, new}} = v_{\text{mass}} + a'_{\text{mass}} \cdot \Delta t, \tag{7.11}$$
$$x_{\text{mass, new}} = x_{\text{mass}} + v'_{\text{mass}} \cdot \Delta t. \tag{7.12}$$

These new values represent the position and velocity at $t + \Delta t$ and are used for the calculation of the next time step.

List of Figures

Bibliography

[1] V. Popov, *Contact mechanics and friction: physical principles and applications*, Springer-Verlag Berlin Heidelberg (2010).

[2] H. Hölscher, A. Schirmeisen, and U. D. Schwarz, *Principles of atomic friction: from sticking atoms to superlubric sliding*, Philosophical Transactions of the Royal Society A: Mathematical, Physical and Engineering Sciences **366**, 1383 (2008).

[3] J. F. Archard, *Contact and rubbing of flat surfaces*, Journal of Applied Physics **24**, 981 (1953).

[4] T. Mayer, J. Elam, S. George, P. Kotula, and R. Goeke, *Atomic-layer deposition of wear-resistant coatings for microelectromechanical devices*, Applied Physics Letters **82**, 2883 (2003).

[5] T. Baumberger and C. Caroli, *Solid friction from stick–slip down to pinning and aging*, Advances in Physics **55**, 279 (2006).

[6] V. Lampaert, F. Al-Bender, and J. Swevers, *Experimental characterization of dry friction at low velocities on a developed tribometer setup for macroscopic measurements*, Tribology Letters **16**, 95 (2004).

[7] J. Israelachvili, Y. Min, M. Akbulut, A. Alig, G. Carver, W. Greene, K. Kristiansen, E. Meyer, N. Pesika, K. Rosenberg *et al.*, *Recent advances in the surface forces apparatus (SFA) technique*, Reports on Progress in Physics **73**, 036601 (2010).

[8] C. M. Mate, G. M. McClelland, R. Erlandsson, and S. Chiang, *Atomic-scale friction of a tungsten tip on a graphite surface*, Physical Review Letters **59**, 1942 (1987).

[9] A. Socoliuc, R. Bennewitz, E. Gnecco, and E. Meyer, *Transition from stick-slip to continuous sliding in atomic friction: entering a new regime of ultralow friction*, Physical Review Letters **92**, 134301 (2004).

[10] E. Gnecco, R. Bennewitz, T. Gyalog, C. Loppacher, M. Bammerlin, E. Meyer, and H.-J. Güntherodt, *Velocity dependence of atomic friction*, Physical Review Letters **84**, 1172 (2000).

[11] Y. Dong, Q. Li, and A. Martini, *Molecular dynamics simulation of atomic friction: A review and guide*, Journal of Vacuum Science & Technology A **31**, 030801 (2013).

[12] T. Göddenhenrich, S. Müller, and C. Heiden, *A lateral modulation technique for simultaneous friction and topography measurements with the atomic force microscope*, Review of Scientific Instruments **65**, 2870 (1994).

[13] G. Binnig, C. F. Quate, and C. Gerber, *Atomic Force Microscope*, Physical Review Letters **56**, 930 (1986).

[14] O. Marti, J. Colchero, and J. Mlynek, *Combined scanning force and friction microscopy of mica*, Nanotechnology **1**, 141 (1990).

[15] G. Meyer and N. M. Amer, *Simultaneous measurement of lateral and normal forces with an optical-beam-deflection atomic force microscope*, Applied Physics Letters **57**, 2089 (1990).

[16] H. Hölscher, D. Ebeling, and U. D. Schwarz, *Friction at Atomic-Scale Surface Steps: Experiment and Theory*, Physical Review Letters **101**, 246105 (2008).

[17] L. Prandtl, *Ein Gedankenmodell zur kinetischen Theorie der festen Körper*, ZAMM-Journal of Applied Mathematics and Mechanics/Zeitschrift für Angewandte Mathematik und Mechanik **8**, 85 (1928).

[18] G. Tomlinson, *CVI. A molecular theory of friction*, The London, Edinburgh, and Dublin Philosophical Magazine and Journal of Science **7**, 905 (1929).

[19] E. Gnecco, R. Bennewitz, T. Gyalog, and E. Meyer, *Friction experiments on the nanometre scale*, Journal of Physics: Condensed Matter **13**, R619 (2001).

[20] T. Gyalog, E. Gnecco, and E. Meyer, *Stick-slip motion on the atomic scale*, in *Fundamentals of Friction and Wear*, 101–115, Springer (2007).

[21] S. Fujisawa, Y. Sugawara, S. Ito, S. Mishima, T. Okada, and S. Morita, *The two-dimensional stick-slip phenomenon with atomic resolution*, Nanotechnology **4**, 138 (1993).

[22] J. A. Ruan and B. Bhushan, *Atomic-scale and microscale friction studies of graphite and diamond using friction force microscopy*, Journal of Applied Physics **76**, 5022 (1994).

[23] N. Sasaki, K. Kobayashi, and M. Tsukada, *Atomic-scale friction image of graphite in atomic-force microscopy*, Physical Review B **54**, 2138 (1996).

[24] S. Fujisawa, K. Yokoyama, Y. Sugawara, and S. Morita, *Analysis of experimental load dependence of two-dimensional atomic-scale friction*, Physical Review B **58**, 4909 (1998).

[25] R. Bennewitz, T. Gyalog, M. Guggisberg, M. Bammerlin, E. Meyer, and H.-J. Güntherodt, *Atomic-scale stick-slip processes on Cu (111)*, Physical Review B **60**, R11301 (1999).

[26] A. Socoliuc, E. Gnecco, S. Maier, O. Pfeiffer, A. Baratoff, R. Bennewitz, and E. Meyer, *Atomic-scale control of friction by actuation of nanometer-sized contacts*, Science **313**, 207 (2006).

[27] R. W. Carpick, D. Ogletree, and M. Salmeron, *Lateral stiffness: a new nanomechanical measurement for the determination of shear strengths with friction force microscopy*, Applied Physics Letters **70**, 1548 (1997).

[28] M. A. Lantz, S. J. O'Shea, M. E. Welland, and K. L. Johnson, *Atomic-force-microscope study of contact area and friction on NbSe 2*, Physical Review B **55**, 10776 (1997).

[29] M. A. Lantz, S. J. O'Shea, A. C. F. Hoole, and M. E. Welland, *Lateral stiffness of the tip and tip-sample contact in frictional force microscopy*, Applied Physics Letters **70**, 970 (1997).

[30] J. Sokoloff, *Theory of dynamical friction between idealized sliding surfaces*, Surface Science **144**, 267 (1984).

[31] H. Hölscher, U. D. Schwarz, and R. Wiesendanger, *Modelling of the scan process in lateral force microscopy*, Surface Science **375**, 395 (1997).

[32] H. Hölscher, U. D. Schwarz, O. Zwörner, and R. Wiesendanger, *Consequences of the stick-slip movement for the scanning force microscopy imaging of graphite*, Physical Review B **57**, 2477 (1998).

[33] H. Hölscher, U. D. Schwarz, and R. Wiesendanger, *Simulation of a scanned tip on a NaF (001) surface in friction force microscopy*, Europhysics Letters **36**, 19 (1996).

[34] O. Zwörner, H. Hölscher, U. D. Schwarz, and R. Wiesendanger, *The velocity dependence of frictional forces in point-contact friction*, Applied Physics A **66**, S263 (1998).

[35] A. J. McMillan, *A non-linear friction model for self-excited vibrations*, Journal of Sound and Vibration **205**, 323 (1997).

[36] U. Rabe, K. Janser, and W. Arnold, *Vibrations of free and surface-coupled atomic force microscope cantilevers: theory and experiment*, Review of Scientific Instruments **67**, 3281 (1996).

[37] A. Raman, J. Melcher, and R. Tung, *Cantilever dynamics in atomic force microscopy*, Nano Today **3**, 20 (2008).

[38] J. Melcher, S. Hu, and A. Raman, *Equivalent point-mass models of continuous atomic force microscope probes*, Applied Physics Letters **91**, 053101 (2007).

[39] G. Stan, S. Krylyuk, A. V. Davydov, M. D. Vaudin, L. A. Bendersky, and R. F. Cook, *Contact-resonance atomic force microscopy for nanoscale elastic property measurements: Spectroscopy and imaging*, Ultramicroscopy **109**, 929 (2009).

[40] U. Rabe, S. Amelio, E. Kester, V. Scherer, S. Hirsekorn, and W. Arnold, *Quantitative determination of contact stiffness using atomic force acoustic microscopy*, Ultrasonics **38**, 430 (2000).

[41] D. Hurley and J. A. Turner, *Measurement of Poisson's ratio with contact-resonance atomic force microscopy*, Journal of Applied Physics **102**, 033509 (2007).

[42] K. Magnus, K. Popp, and W. Sextro, *Schwingungen: physikalische Grundlagen und mathematische Behandlung von Schwingungen*, volume 9, Springer Vieweg Verlag (2013).

[43] R. P. Feynman, R. B. Leighton, and M. Sands, *The Feynman: Mechanik, Strahlung, Wärme: mit 28 Tabellen/[dt. Übers.: Kap. 1-25 Heinz Köhler; Kap. 26-52 Eckhard Schröder]. Bd. 1*, volume 1, Oldenbourg Verlag (2007).

[44] S. Jesse, S. V. Kalinin, R. Proksch, A. Baddorf, and B. Rodriguez, *The band excitation method in scanning probe microscopy for rapid mapping of energy dissipation on the nanoscale*, Nanotechnology **18**, 435503 (2007).

[45] A. U. Kareem and S. D. Solares, *Characterization of surface stiffness and probe sample dissipation using the band excitation method of atomic force microscopy: a numerical analysis*, Nanotechnology **23**, 015706 (2012).

[46] U. D. Schwarz, O. Zwörner, P. Köster, and R. Wiesendanger, *Quantitative analysis of the frictional properties of solid materials at low loads. I. Carbon compounds*, Physical Review B **56**, 6987 (1997).

[47] D. Dietzel, M. Feldmann, U. D. Schwarz, and A. Schirmeisen, *Scaling Laws of Structural Lubricity*, Physical Review Letters **111**, 235502 (2013).

[48] B. Persson, *Theory and simulation of sliding friction*, Physical Review Letters **71**, 1212 (1993).

[49] M. Evstigneev, A. Schirmeisen, L. Jansen, H. Fuchs, and P. Reimann, *Contact ageing in atomic friction*, Journal of Physics: Condensed Matter **20**, 354001 (2008).

[50] Q. Li, T. E. Tullis, D. Goldsby, and R. W. Carpick, *Frictional ageing from interfacial bonding and the origins of rate and state friction*, Nature **480**, 233 (2011).

[51] Y. Liu and I. Szlufarska, *Chemical Origins of Frictional Aging*, Physical Review Letters **109**, 186102 (2012).

[52] R. W. Carpick and M. Salmeron, *Scratching the surface: fundamental investigations of tribology with atomic force microscopy*, Chemical Reviews **97**, 1163 (1997).

[53] E. Gnecco and E. Meyer, *Fundamentals of friction and wear*, Springer (2007).

[54] D. Dietzel, U. D. Schwarz, and A. Schirmeisen, *Nanotribological studies using nanoparticle manipulation: Principles and application to structural lubricity*, Friction **2**, 114 (2014).

[55] M. Dienwiebel, G. Verhoeven, N. Pradeep, J. Frenken, J. Heimberg, and H. Zandbergen, *Superlubricity of graphite*, Physical Review Letters **92**, 126101 (2004).

[56] K. Shinjo and M. Hirano, *Dynamics of friction: superlubric state*, Surface Science **283**, 473 (1993).

[57] M. Hirano, *Superlubricity: a state of vanishing friction*, Wear **254**, 932 (2003).

[58] H.-U. Krotil, E. Weilandt, T. Stifter, O. Marti, and S. Hild, *Dynamic friction force measurement with the scanning force microscope*, Surface and Interface Analysis **27**, 341 (1999).

[59] A. Spychalski-Merle, K. Krischker, T. Göddenhenrich, and C. Heiden, *Friction contrast in resonant cantilever vibration mode*, Applied Physics Letters **77**, 501 (2000).

[60] M. Reinstädtler, U. Rabe, V. Scherer, U. Hartmann, A. Goldade, B. Bhushan, and W. Arnold, *On the nanoscale measurement of friction using atomic-force microscope cantilever torsional resonances*, Applied Physics Letters **82**, 2604 (2003).

[61] K. Krischker, *Modulations-Reibungsmikroskopie in der Hebelarm-Biegeresonanz zur Charakterisierung von Oberflächeneigenschaften im UHV*, Ph.D. thesis, Justus-Liebig-Universität Giessen (2001).

[62] D. Iannuzzi, S. Deladi, V. J. Gadgil, R. G. P. Sanders, H. Schreuders, and M. C. Elwenspoek, *Monolithic fiber-top sensor for critical environments and standard applications*, Applied Physics Letters **88**, 053501 (2006).

[63] D. Chavan, G. Gruca, S. de Man, M. Slaman, J. H. Rector, K. Heeck, and D. Iannuzzi, *Ferrule-top atomic force microscope*, Review of Scientific Instruments **81**, 123702 (2010).

[64] D. Rugar, H. J. Mamin, and P. Guethner, *Improved fiber-optic interferometer for atomic force microscopy*, Applied Physics Letters **55**, 2588 (1989).

[65] A. Oral, R. A. Grimble, H. O. Özer, and J. B. Pethica, *High-sensitivity noncontact atomic force microscope/scanning tunneling microscope (nc AFM/STM) operating at subangstrom oscillation amplitudes for atomic resolution imaging and force spectroscopy*, Review of Scientific Instruments **74**, 3656 (2003).

[66] D. T. Smith, J. R. Pratt, and L. P. Howard, *A fiber-optic interferometer with sub-picometer resolution for dc and low-frequency displacement measurement*, Review of Scientific Instruments **80**, 035105 (2009).

[67] W.-T. Pong and C. Durkan, *A review and outlook for an anomaly of scanning tunnelling microscopy (STM): superlattices on graphite*, Journal of Physics D: Applied Physics **38**, R329 (2005).

[68] A. Pak, G. Gregori, J. Knight, K. Campbell, D. Price, B. Hammel, O. Landen, and S. Glenzer, *X-ray line measurements with high efficiency Bragg crystals*, Review of Scientific Instruments **75**, 3747 (2004).

[69] J. E. Sader, *Susceptibility of atomic force microscope cantilevers to lateral forces*, Review of Scientific Instruments **74**, 2438 (2003).

[70] W. Sharpe, B. Yuan, R. Vaidyanathan, and R. L. Edwards, *Measurements of Young's modulus, Poisson's ratio, and tensile strength of polysilicon*, in *Micro Electro Mechanical Systems, 1997. MEMS '97, Proceedings, IEEE., Tenth Annual International Workshop on*, 424–429 (1997).

[71] P. Zahl, M. Bierkandt, S. Schröder, and A. Klust, *The flexible and modern open source scanning probe microscopy software package GXSM*, Review of Scientific Instruments **74**, 1222 (2003).

[72] P. Zahl, T. Wagner, R. Möller, and A. Klust, *Open source scanning probe microscopy control software package GXSM*, Journal of Vacuum Science & Technology B **28**, C4E39 (2010).

[73] J. Colchero, M. Luna, and A. M. Baro, *Lock-in technique for measuring friction on a nanometer scale*, Applied Physics Letters **68**, 2896 (1996).

[74] F. Mertens, T. Göddenhenrich, and A. Schirmeisen, *Resonant cantilever response of static-to-sliding transitions in dynamic friction force microscopy*, Applied Physics Letters **104**, 113105 (2014).

[75] K. Yamanaka and E. Tomita, *Lateral Force Modulation Atomic Force Microscope for Selective Imaging of Friction Forces*, Japanese Journal of Applied Physics **34**, 2879 (1995).

[76] G. Haugstad, *Contrasting static-to-kinetic friction transitions on layers of an autophobically dewetted polymer film using Fourier-analyzed shear modulation force microscopy*, Tribology Letters **19**, 49 (2005).

[77] T. Kawagishi, A. Kato, Y. Hoshi, and H. Kawakatsu, *Mapping of lateral vibration of the tip in atomic force microscopy at the torsional resonance of the cantilever*, Ultramicroscopy **91**, 37 (2002).

[78] W. Georgi and E. Metin, *Einführung in LabVIEW*, Carl Hanser Verlag GmbH Co KG (2012).

[79] F. J. Harris, *On the use of windows for harmonic analysis with the discrete Fourier transform*, Proceedings of the IEEE **66**, 51 (1978).

[80] C. H. Scholz, *Earthquakes and friction laws*, Nature **391**, 37 (1998).

[81] M. A. Heckl and I. Abrahams, *Curve squeal of train wheels, part 1: mathematical model for its generation*, Journal of Sound and Vibration **229**, 669 (2000).

[82] T. Palberg and K. Streicher, *Resonant stick–slip motion in a colloidal crystal*, Nature **367**, 51 (1994).

[83] I. R. Gatland, *Numerical Integration of Newtons equation including velocity-dependent forces*, American Journal of Physics **62**, 259 (1994).

[84] D. Dietzel, T. Mönninghoff, C. Herding, M. Feldmann, H. Fuchs, B. Stegemann, C. Ritter, U. D. Schwarz, and A. Schirmeisen, *Frictional duality of metallic nanoparticles: Influence of particle morphology, orientation, and air exposure*, Physical Review B **82**, 035401 (2010).

[85] M. Feldmann, D. Dietzel, H. Fuchs, and A. Schirmeisen, *Influence of Contact Aging on Nanoparticle Friction Kinetics*, Physical Review Letters **112**, 155503 (2014).

[86] A. Schirmeisen and U. D. Schwarz, *Measuring the friction of nanoparticles: a new route towards a better understanding of nanoscale friction*, ChemPhysChem **10**, 2373 (2009).

[87] B. Bhushan, *Nanotribology and nanomechanics*, Wear **259**, 1507 (2005).

[88] B. Bhushan and T. Kasai, *A surface topography-independent friction measurement technique using torsional resonance mode in an AFM*, Nanotechnology **15**, 923 (2004).

[89] B. Stegemann, *Wechselwirkungen monodisperser Antimon-Cluster mit Oberflächen: Diffusion, Wachstum und Strukturbildung im Nanometerbereich*, Shaker (2003).

[90] B. Stegemann, C. Ritter, B. Kaiser, and K. Rademann, *Crystallization of antimony nanoparticles: Pattern formation and fractal growth*, The Journal of Physical Chemistry B **108**, 14292 (2004).

[91] M. Cuberes, B. Stegemann, B. Kaiser, and K. Rademann, *Ultrasonic force microscopy on strained antimony nanoparticles*, Ultramicroscopy **107**, 1053 (2007).

[92] S. Sundararajan and B. Bhushan, *Topography-induced contributions to friction forces measured using an atomic force/friction force microscope*, Journal of Applied Physics **88**, 4825 (2000).

[93] H. Hölscher, U. D. Schwarz, and R. Wiesendanger, *Calculation of the frequency shift in dynamic force microscopy*, Applied Surface Science **140**, 344 (1999).

[94] P. Simonis, C. Goffaux, P. A. Thiry, L. P. Biro, P. Lambin, and V. Meunier, *STM study of a grain boundary in graphite*, Surface Science **511**, 319 (2002).

[95] W.-T. Pong, J. Bendall, and C. Durkan, *Observation and investigation of graphite superlattice boundaries by scanning tunneling microscopy*, Surface Science **601**, 498 (2007).

[96] J. Červenka and C. Flipse, *Structural and electronic properties of grain boundaries in graphite: Planes of periodically distributed point defects*, Physical Review B **79**, 195429 (2009).

[97] P. Y. Huang, C. S. Ruiz-Vargas, A. M. van der Zande, W. S. Whitney, M. P. Levendorf, J. W. Kevek, S. Garg, J. S. Alden, C. J. Hustedt, Y. Zhu, J. Park, P. L. McEuen, and D. A. Muller, *Grains and grain boundaries in single-layer graphene atomic patchwork quilts*, Nature **469**, 389 (2011).

[98] A. J. Marsden, M. Phillips, and N. R. Wilson, *Friction force microscopy: a simple technique for identifying graphene on rough substrates and mapping the orientation of graphene grains on copper*, Nanotechnology **24**, 255704 (2013).

[99] C. S. Ruiz-Vargas, H. L. Zhuang, P. Y. Huang, A. M. van der Zande, S. Garg, P. L. McEuen, D. A. Muller, R. G. Hennig, and J. Park, *Softened Elastic Response and Unzipping in Chemical Vapor Deposition Graphene Membranes*, Nano Letters **11**, 2259 (2011).

[100] K. Kim, Z. Lee, W. Regan, C. Kisielowski, M. F. Crommie, and A. Zettl, *Grain Boundary Mapping in Polycrystalline Graphene*, ACS Nano **5**, 2142 (2011).

[101] E. Cockayne, G. M. Rutter, N. P. Guisinger, J. N. Crain, P. N. First, and J. A. Stroscio, *Grain boundary loops in graphene*, Physical Review B **83**, 195425 (2011).

[102] S. Malola, H. Häkkinen, and P. Koskinen, *Structural, chemical, and dynamical trends in graphene grain boundaries*, Physical Review B **81**, 165447 (2010).

[103] A. Mesaros, S. Papanikolaou, C. F. J. Flipse, D. Sadri, and J. Zaanen, *Electronic states of graphene grain boundaries*, Physical Review B **82**, 205119 (2010).

[104] Y. Wang, Y. Ye, and K. Wu, *Simultaneous observation of the triangular and honeycomb structures on highly oriented pyrolytic graphite at room temperature: An STM study*, Surface Science **600**, 729 (2006).

[105] T. Müller, M. Lohrmann, T. Kässer, O. Marti, J. Mlynek, and G. Krausch, *Frictional force between a sharp asperity and a surface step*, Physical Review Letters **79**, 5066 (1997).

[106] E. Weilandt, A. Menck, and O. Marti, *Friction studies at steps with friction force microscopy*, Surface and Interface Analysis **23**, 428 (1995).

[107] P. Egberts, Z. Ye, X. Z. Liu, Y. Dong, A. Martini, and R. W. Carpick, *Environmental dependence of atomic-scale friction at graphite surface steps*, Physical Review B **88**, 035409 (2013).

[108] R. L. Schwoebel, *Step Motion on Crystal Surfaces*, Journal of Applied Physics **37**, 3682 (1966).

[109] G. Ehrlich and F. Hudda, *Atomic View of Surface Self-Diffusion: Tungsten on Tungsten*, Journal of Chemical Physics **44**, 1039 (1966).

[110] C. Lee, Q. Li, W. Kalb, X.-Z. Liu, H. Berger, R. W. Carpick, and J. Hone, *Frictional Characteristics of Atomically Thin Sheets*, Science **328**, 76 (2010).

Publications and Conference Contributions

Publications

F. Mertens, T. Göddenhenrich, and A. Schirmeisen, *Resonant cantilever response of static-to-sliding transitions in dynamic friction force microscopy*, Applied Physics Letters **104** 113105 (2014)

F. Mertens, T. Göddenhenrich, V. Lushta, and A. Schirmeisen, *Dynamic friction force microscopy using fractional resonance excitation: Image contrast of graphite surface defects*, (2015)

Conference Contributions

Materialforschungstag Mittelhessen 2011: F. Mertens, K. Krischker, T. Göddenhenrich, A. Schirmeisen, *Dynamic Friction Force Microscopy: Image Contrast at Higher Modes on HOPG*, Gießen 2011 (poster)

3rd International Workshop on Advanced Atomic Force Microscopy Techniques 2012: F. Mertens, K. Krischker, T. Göddenhenrich, A. Schirmeisen, *Dynamic Friction Force Microscopy: Image Contrast at Higher Modes on HOPG*, Karlsruhe 2012 (poster)

DPG Frühjahrstagung der Sektion Kondensierte Materie (SKM) 2012: F. Mertens, T. Göddenhenrich, A. Schirmeisen, *Dynamic Friction Force Microscopy: Image Contrast at Higher Modes on HOPG*, Berlin 2012 (poster)

Materialforschungstag Mittelhessen 2012: F. Mertens, T. Göddenhenrich, A. Schirmeisen, *Dynamic Friction Force Microscopy: Imaging via control of nonlinear cantilever oscillation*, Marburg 2012 (poster)

4th International Workshop on Advanced Atomic Force Microscopy Techniques 2013: F. Mertens, T. Göddenhenrich, A. Schirmeisen, *Dynamic Friction Force Microscopy: Imaging via control of nonlinear cantilever oscillation*, Karlsruhe 2013 (talk)

DPG Frühjahrstagung der Sektion Kondensierte Materie (SKM) 2013: F. Mertens, T. Göddenhenrich, A. Schirmeisen, *Friction induced self-excited cantilever resonance oscillation*, Regensburg 2013 (talk)

DPG Frühjahrstagung der Sektion Kondensierte Materie (SKM) 2013: F. Mertens, T. Göddenhenrich, A. Schirmeisen *Dynamic Friction Force Microscopy: Imaging via control of nonlinear cantilever oscillation*, Regensburg 2013 (poster)

544. WE-Heraeus-Seminar: Interactions with the Nanoworld: Local Probes with High Time, Energy and Force Resolution: F. Mertens, T. Göddenhenrich, A. Schirmeisen, *Dynamic Friction Force Microscopy on Antimony Nanoparticles*, Bad Honnef 2013 (poster)

DPG Frühjahrstagung der Sektion Kondensierte Materie (SKM) 2014: F. Mertens, T. Göddenhenrich, A. Schirmeisen, *Friction contrast in Dynamic Friction Force Microscopy*, Dresden 2014 (talk)

DPG Frühjahrstagung der Sektion Kondensierte Materie (SKM) 2014: T. Göddenhenrich, F. Mertens, A. Schirmeisen, *Dynamic Friction Force Microscopy on antimony nanoparticles*, Dresden 2014 (poster)

4th Euro AFM Forum: F. Mertens, T. Göddenhenrich, A. Schirmeisen, *Dynamic Friction Force Microscopy: Revealing grain boundaries on graphite surfaces*, Göttingen 2014 (poster)

5th Multifrequency AFM Conference: F. Mertens, T. Göddenhenrich, A. Schirmeisen, *Dynamic Friction Force Microscopy: Imaging via control of non-linear cantilever oscillation*, Madrid 2014 (poster)

DPG Frühjahrstagung der Sektion Kondensierte Materie (SKM) 2015: F. Mertens, T. Göddenhenrich, A. Schirmeisen, *Dynamic Friction Force Microscopy at Surface Defects on HOPG*, Berlin 2015 (talk)

Acknowledgment

An dieser Stelle möchte ich mich bei all denjenigen bedanken, die mich bei der Anfertigung dieser Arbeit unterstützt haben. Ich bedanke mich bei

Prof. Dr. André Schirmeisen, der diese Arbeit angeregt und betreut hat und mit dessen Unterstützung diese zu einem erfolgreichen Abschluss geführt wurde,

Thomas Göddenhenrich für das stets freundliche Arbeitsklima, die kompetente Unterstützung und die Weiterreichung seines Fachwissens,

Michael Feldmann für seine Unterstützung bei der Steuersoftware GXSM und eine stets unterhaltsame Zeit im Büro,

Yusuf Kücükkaplan, der mit seinem feinmechanischen Know-How die Realisierung der experimentellen Aufbauten erst möglich gemacht hat,

den beiden Postdocs Dirk Dietzel und Daniel Ebeling, die mir zu jeder Zeit mit Rat und Tat zur Seite standen,

Alexandra Gabriel, für die immer freundliche und schnelle Unterstützung bei formalen Angelegenheiten,

und der gesamten Arbeitsgruppe Schirmeisen, allen voran meinen Bürokollegen, mit denen ich in den letzten vier Jahren eine lehrreiche und lustige Zeit durchlebt habe.

Mein ganz besonderer Dank gilt natürlich meiner Verlobten Sarah, meinen Eltern sowie meiner gesamten Familie, die mich während meiner Doktorandenzeit in jeder Hinsicht unterstützt haben.

Ich erkläre:
Ich habe die vorgelegte Dissertation selbständig und ohne unerlaubte fremde Hilfe und nur mit den Hilfen angefertigt, die ich in der Dissertation angegeben habe. Alle Textstellen, die wörtlich oder sinngemäß aus veröffentlichten Schriften entnommen sind, und alle Angaben, die auf mündlichen Auskünften beruhen, sind als solche kenntlich gemacht. Bei den von mir durchgeführten und in der Dissertation erwähnten Untersuchungen habe ich die Grundsätze guter wissenschaftlicher Praxis, wie sie in der "Satzung der Justus-Liebig-Universität Gießen zur Sicherung guter wissenschaftlicher Praxis" niedergelegt sind, eingehalten.

Felix Mertens

Gießen, April 2015